UNIVERSIDADE D
COIMBRA

ANZUM AL ABIR

MECHANICAL AND TRIBOLOGICAL BEHAVIOUR ANALYSIS OF POLY (LACTIC ACID) REINFORCED WITH SN-ZN-BI, SHORT CARBON FIBRES, AND GRAPHENE PRODUCED BY CASTING, 3D PRINTING, AND LASER TEXTURING

VOLUME 1

Dissertation under the Joint European Master's Degree in Surface Tribology and Interfaces guided by Prof. Dr. Bruno Trindade presented to the Department of Mechanical Engineering of the Faculty of Science and Technology of the University of Coimbra.

July 2022

1 2 9 0

FACULDADE DE CIÊNCIAS E TECNOLOGIA
UNIVERSIDADE D COIMBRA

Mechanical and tribological behaviour analysis of Poly (Lactic Acid) reinforced with Sn-Zn-Bi, short carbon fibres, and graphene produced by casting, 3D printing, and laser texturing.

Submitted in Partial Fulfilment of the Requirements for the Degree of European Joint European Master in Tribology of Surfaces and Interfaces.

Análise do comportamento mecânico e tribológico do poli (ácido lático) reforçado com Sn-Zn-Bi, fibras curtas de carbono e grafeno produzido por fundição, impressão 3D e texturização a laser.

Author

Anzum Al Abir

Advisor[s]

Prof. Dr. Bruno Trindade

Jury

President	**Prof. Dr. Albano Cavaleiro** **Professor at University of Coimbra**
Vowel	**Prof[a]. Dr[a]. Paula Piedade** **Professor at University of Coimbra**
Advisor	**Prof. Dr. Bruno Trindade** **Professor at University of Coimbra**

· U C ·

UNIVERSIDADE DE COIMBRA

tribos
Joint European Master in Tribology of Surfaces and Interfaces
Ljubljana • Leeds • Coimbra • Luleå

Coimbra, July 2022

ACKNOWLEDGMENTS

I wish to express my gratitude to my master thesis advisor Prof. Bruno Trindade from the University of Coimbra, for his professional guidance, support, and insightful suggestions during the writing of this work.

I would like to extend my gratitude to the staff at IPN, particularly to Carlos Patacas, António Fonseca, Fábio Cerejo, Todor Vuckov, and Nelson Duarte, Sergio Lourenco, and Telma Ferreira, for their time and effort in performing the characterisation of the project samples. I would like to thank the staff at the Mechanical Department of the University of Coimbra, particularly, Catarina Pinho, Pedro Soares, Diego, Luis Cacho, and Goncalo Olivera who also helped in the production and characterisation of the samples. Special thanks to the staff at the University of Aveiro (Dr Florinda Costa) for providing the laser machine and expertise for the conduction of the laser texturing experiments. Finally, I want to express my gratitude to the TRIBOS consortium and the European Commission for supporting my master's program. The completion of this thesis would not have been possible without their financial help.

RESUMO

Os compósitos de matriz polimérica são uma excelente opção para muitas indústrias tecnologicamente exigentes, tais como aeroespacial, automóvel, naval e civil. Tal deve-se às suas excepcionais propriedades multifuncionais. Devido à sua crescente demanda, são necessários estudos detalhados sobre o seu comportamento físico, químico, tribológico e mecânico sob várias situações de exposição. Os polímeros à base de petróleo têm inúmeros efeitos ambientais negativos, como poluição (terra, água, etc.) e aquecimento global. Como alternativa, os polímeros biodegradáveis têm grande potencial elavado para substituir os plásticos tradicionais à base de petróleo. Entre eles, o poli (ácido lático) (PLA) é um plástico biodegradável promissor, amplamente disponível, que tem a capacidade de se decompor após o uso, sem poluir o meio ambiente, sendo por isso usado em diferentes aplicações de engenharia. No entanto, apresenta algumas limitações, como a baixa resistência ao desgaste e as baixas propriedades mecânicas que, por vezes, provocam algum grau de limitação funcional das peças.

O objetivo deste projeto é melhorar as propriedades mecânicas e tribológicas do PLA através do seu reforço com materiais autolubrificantes com baixo atrito e taxa de desgaste, capazes de minimizar a formação e libertação de detritos de desgaste. Para tal, nanoplaquetas de grafeno (GNP), fibras curtas de carbono (SCF) e uma liga de brasagem à base de Sn foram adicionados à matriz de PLA para melhorar as suas propriedades. Existem inúmeras técnicas de produção de compósitos de matriz polimérica, cada uma com vantagens e desvantagens únicas. Neste estudo, três processos de produção diferentes foram usados para produzir as amostras compósitas: (i) síntese mecânica seguida de fundição, (ii) a síntese mecânica/plastografia seguida de extrusão e impressão 3D e (iii) a texturização a laser do PLA fundido, compactação a frio dos reforços e sinterização a laser. Os resultados mostraram que as amostras compósitas reforçadas com GNP e SCF (50-50% em peso relativo) apresentaram os melhores desempenhos mecânico e tribológico, seguidas pelas reforçadas apenas com GNP. Nas amostras produzidas pelo processo de fundição e impressão 3D, concluiu-se que a adição de GNP melhorou significativamente as propriedades mecânicas e tribológicas dos compósitos PLA-GNP. Embora as amostras reforçadas com a liga Sn-Zn-Bi tenham melhorado a dureza dos compósitos obtidos por fundição, o coeficiente de atrito e a resistência ao desgaste foram piores nessas amostras, em comparação com os outros compósitos e com o PLA puro. Outra conclusão importante retirasda deste trabalho foi a de que 1% em peso de GNP e SCF é

suficiente para aumentar significativamente a dureza dos compósitos. No entanto, o aumento do teor destes reforços não teve grande influência nesta propriedade. A dureza do compósito com 5% em peso de GNP e SCF, apenas sofreu um pqueneo aumento de dureza quando comparada com a amostra com 1% em peso destes reforços. Em relação ao comportamento tribológico, observou-se que os valores de COF aumentaram com o aumento do teor de GNP + SCF. No que diz respeito ao processo de texturação e sinterização a laser e com base nos resultados preliminares, pode afirmar-se que os compósitos com GNP tiveram o melhor desempenho tribológico e que o compósito com SCF apresentou os valores mais elevados das propriedades mecânicas. No entanto, as condições de sinterização não foram as mais indicadas, pelo que há necessidade de estudar com mais detalhe diferentes parâmetros do processo.

Para trabalhos futuros propõe-se estudar com mais detalhe o efeito dos reforços no polímero PLA.

ABSTRACT

Polymer composites are an excellent option for many technologically demanding industries, including aerospace, automotive, marine, and civil. This is due to their exceptional multi-functional qualities. A detailed examination of these composites' physical, chemical, tribological, and mechanical behaviour under various exposure situations is required due to the rising demand for them. Petroleum-based polymers have numerous negative environmental effects such as pollution (land, water, etc.), and global warming. Biodegradable polymers are one of the most potential materials for replacing traditional petroleum-based plastics. Among all the polymers, poly (lactic acid) (PLA) is a promising biodegradable plastic that is not only widely available but also safe to decompose after use without polluting the environment. PLA is also used in different engineering applications. But it has a few disadvantages such as the low wear resistance and low mechanical properties which sometimes causes some degree of functional limitation of the parts.

The goal of this project is to improve the mechanical and tribological properties of PLA. This will be accomplished by creating a self-lubricating reinforced PLA composite with low friction and wear rate, capable of minimizing wear debris formation and release. For this purpose, graphene nanoplatelets (GNP), short carbon fibres (SCF), and soft Sn-based brazing alloy were added to the PLA matrix to improve its properties. There are numerous polymer matrix composite production techniques, each with unique advantages and disadvantages. In this study, three different production processes were used to produce the composite samples. The first one is mechanical alloying followed by casting, the second one is mechanical alloying/plastography followed by extrusion and 3D printing, and the third one is laser texturing of casted PLA, cold compaction of the reinforcements, and laser sintering. In all the cases, the composite samples reinforced with GNP and SCF (50-50 relative wt.%) showed the best results in terms of mechanical and tribological performance. The second-best composite sample were the ones with GNP solely. In the samples produced by the casting and 3D printing process, the GNP reinforced composite exhibited that the GNP alone can significantly improve the mechanical and tribological properties. Though the samples reinforced with Sn-Zn-Bi alloy improved the hardness of the casted composites, the friction coefficient and wear resistance were the worst in those samples compared to the other composites and the pure PLA as well. Another important finding was that the 1 wt.% of GNP and SCF is enough to increase the hardness significantly. But adding more concentration of GNP and SCF to the composite did

not help much in hardness. At 5 wt.% of GNP and SCF, the hardness of the composites increased a little bit compared to the ones with 1 wt.% of reinforcements. Concerning the tribological behaviour, it was observed that COF values increased with the increase of the GNP and SCF wt.%. The lack of adequate sintering process conditions led to some difficulties with the samples produced by laser surface texturing, cold compaction, and laser sintering. However, based on some preliminary results, it can be said that the composites with GNP performed better tribologically and the composite with SCF showed improvement in mechanical properties.

There is a scope of future work regarding this project to have a better understanding of the composite and the effect of reinforcements on its properties.

CONTENTS

1. INTRODUCTION 14

2. AIM OF THE STUDY 16

3. STATE OF ART 17

3.1 poly (lactic acid) (PLA) 17

3.2 Polymer Matrix Composite 18

3.3 Basic method of production 19

3.4 PLA-based Composite material 19

3.5 PLA-based composite Tribological behaviour 20

3.6 Mechanical alloying 27

3.6.1 Polymer-based composites produced by MA 27

3.7 3D printing of PLA-composite 29

3.8 Laser texturing of PLA 30

4. RESEARCH GAP AND OBJECTIVE 33

5. EXPERIMENTAL DETAILS 34

5. 1. Manufacturing processes 34

5.1.1. Mechanical alloying procedure 34

5.1.2. Casting 34

5.1.3 3D printing Procedure 37

5.1.4 Laser Texturing & Sintering Procedure 41

5.2 Characterisation techniques 42

5.2.1 Morphological and chemical characterisation 42

5.2.2 Tomography 43

5.2.3 3D profilometry 44

5.2.4. Structural characterisation 44

5.3.5. Thermal analysis characterisation 45

5.3.6. Mechanical and tribological characterisation 46

5.3. Raw materials 49

6. RESULTS and DISCUSSION 54
6.1. Mechanical alloying and casting process……..56
6.1.1. Mechanical alloying……57
6.1.2. Casting…… 60
6.2. Mechanical alloying / plastography, filament extrusion, and 3D Printing……68
6.2.1. Mechanical alloying……..69
6.2.2. Filament Extrusion……69
6.2.3. 3D printing……70
6.3. Plastography, filament extrusion, and 3D Printing (preliminary results)…… ……..77
6.3.1 Plastography……...78
6.3.2. 3D printing……78
6.4. Laser texturing, reinforcement of the texture by cold compaction, and laser sintering (preliminary results) ……...83
6.4.1 Laser texturing……...83
6.4.2. Cold Compaction……..84
7. CONCLUSION……....87
8. FUTURE WORK……88
9. REFERENCES…….……..… ……....89

LIST OF FIGURES

Figure 1: Major polymer matrix composite fabrication processes [55] 21
Figure 2: COF dependence on carbon monofiller content in PLA-based nanocomposites (scratch test data) [59]. 22
Figure 3: COF dependence on carbon monofiller content in PLA-based nanocomposites (wear test data) [59]. 23
Figure 4: COF dependence on 3 and 6 wt.% monofiller and bifiller content in PLA-based nanocomposites [59]. 23
Figure 5: COF dependence on 9 and 12 wt.% monofiller and bifiller content in PLA-based nanocomposites [59]. 24
Figure 6: Average tensile stress-strain curve for PLA and PLA-based composites [60]. 24
Figure 7 25
Figure 8: Average stress-strain curve for PLA and PLA-based composites from flexural test [60]. 26
Figure 9: Results of flexural properties of PLA and PLA-based 3D printed composite samples [60]. 26
Figure 10: Tensile strength (a), and elongation-at-break (b) for PLA and PLA-GR nanocomposites [61]. 27
Figure 11: TEM images of the bi-filler composites containing (a) polylactic acid (PLA)/1.5wt.% GNP/4.5wt.% MWCNT and (b) PLA/3 wt.% GNP/3 wt.% MWCNT, respectively [62]. 27
Figure 12: Electrical conductivity vs. GNP and MWCNT filler content for mono-filler (PLA/GNP and 28
Figure 13: Mechanical and tribological properties of the reinforced UHMWPE samples [65]. 29
Figure 14: Storage modulus plot versus temperature for neat PLA and its nanocomposites films with BCNC [67]. 30
Figure 15: Oxygen permeability at 80% RH for neat PLA and Its nanocomposites with BCNC prepared by ball milling [67]. 31
Figure 16: Tensile stress-strain curves (a) and Flexural stress-strain curves (b) for the 3D printed PLA and PLA-Graphene composite samples [68]. 32

Figure 17: Microscopic images of the obtained surfaces (magnification 100) recorded for reference material (Ref) and laser-treated with accumulated fluences of 24 J/cm2 (F1), 48 J/cm2 (F2) and 71 J/cm2 (F3) [70]. 33
Figure 18: Typical loads vs. indentation depth curves for reference material (Ref) and laser-treated with accumulated fluences of 24 J/cm2 (F1), 48 J/cm2 (F2) and 71 J/cm2 (F3) [70]. 34
Figure 19: Planetary ball milling mechanism [75]. 36
Figure 20: Ball-powder-ball collision of metal powders during MA [76]. 37
Figure 21: Planetary ball mill (Frisch Pulverisette 6) 38
Figure 22: Schematic diagram of the casting process. 39
Figure 23: Schematic diagram of the extrusion process. 40
Figure 24: Extruder used in this work. 40
Figure 25: Production by 3D printing method [78]. 41
Figure 26: 3D printer (Prusa i3 MK3) used in this work. 41
Figure 27: Plastograph used in this work. 42
Figure 28: Granulator used in this work. 43
Figure 29: SEM (Hitachi-SU3800) used in this work. 45
Figure 30: SKYSCAN X-ray microtomography equipment used in this work. 45
Figure 31: 3D profilometer (Alicona-InfiniteFocus) used in this work. 46
Figure 32: Philips XPert XRD equipment used in this work. 47
Figure 33: DSC equipment (NETZSCH-DSC 204 f1 phoenix) used in this work. 48
Figure 34: Shore (Durometer) Hardness Tester used in this work. 48
Figure 35: 3-Point bending test equipment (Shimadzu AG-10 universal testing machine). 49
Figure 36: Pin on disk tribometer (Rtec). 50
Figure 37: Raw PLA. 51
Figure 38: SEM images corresponding to the initial morphology of raw powders: (a) GNP, (b) SCF, (c) Bi, (d) Zn, (e) Sn 52
Figure 39: XRD pattern of raw PLA. 53
Figure 40: XRD pattern of raw Sn-Zn-Bi mixture. 53
Figure 41: XRD pattern of PLA, GNP, and SCF. 54
Figure 42: DSC of PLA particle. 54
Figure 43: DSC of PLA used for 3D printing. 55
Figure 44: Diagram of all the raw materials and techniques used in this work. 56
Figure 45: Flow diagram of mechanical alloying and casting. 57

Figure 46: (a) SEM images and (b) EDS elemental maps of Sn-Zn-Bi mixture after 5 hours of MA. 58
Figure 47: (a) SEM images and (b) EDS elemental maps of Sn-Zn-Bi mixture after 10 hours of MA. 58
Figure 48: (a) SEM images and (b) EDS elemental maps of Sn-Zn-Bi mixture after 25 hours of MA. 59
Figure 49: EDS elemental analysis of Sn-Zn-Bi alloy after 25 hours of MA. 59
Figure 50: XRD patterns of the Sn-Zn-Bi mixture milled for 5, 10, and 25h. 60
Figure 51: PLA granules coated with GNP and metallic alloy, as a typical example of the other coated systems. 61
Figure 52: (a) SEM images and (b) EDS elemental maps PLA granules coated with GNP and SCF, as a typical example of all the other systems. 61
Figure 53: Different casted samples produced in this work. 61
Figure 54: XRD patterns of the raw and casted PLA. 62
Figure 55: DSC of casted PLA. 63
Figure 56: XRD patterns of the PLA, PS, and PG casted samples. 63
Figure 57: XRD of PLA and PLA reinforced with the metallic alloy casted samples. 64
Figure 58: Shore D hardness of the casted samples. 65
Figure 59: Time vs COF curves of the casted samples. 66
Figure 60: Average COF values of the casted samples 66
Figure 61: Images of the wear profiles and 3D scans of the casted samples. 67
Figure 62: Specific Wear rate of the casted samples. 68
Figure 63: Complete diagram of 3D printed samples' manufacturing process. 69
Figure 64: Diameter of (a) PLA, (b) PG and (c) PSG filaments. 70
Figure 65: Microtomography images of (a) PLA, (b) PG, and (c) PSG filaments. 71
Figure 66: DSC curves of (a) PLA, (b) PG, and (c) PSG filaments. 71
Figure 67: 3D printed samples. 72
Figure 68: XRD patterns of the 3D printed samples. 72
Figure 69: Microtomography of PG-3D. 73
Figure 70: Microtomography of PSG-3D sample. 73
Figure 71: Shore D hardness of the 3D printed samples. 74
Figure 72: (a) Load vs displacement and (b) Flexural stress-strain curves of the 3D printed samples obtained from the 3-point bending tests. 74
Figure 73: Flexural modulus of the 3D printed samples. 75

Figure 74: Time vs COF curves of the 3D printed samples. 76
Figure 75: Average COF values of the 3D printed samples. 76
Figure 76: 3D profilometry images of the wear profiles and 3D scans of the 3D printed samples. 77
Figure 77: Specific Wear rate of the 3D printed samples. 78
Figure 78: Complete diagram of 3D printed samples' manufacturing process using plastography. 79
Figure 79: Torque vs time curve for different PLA, GNP, and SCF mixtures. 80
Figure 80: PSG-2 3D printed sample. 81
Figure 81: Shore D hardness of the 3D printed samples. 82
Figure 82: Time vs COF curves of the 3D printed samples. 82
Figure 83: Average COF values of the casted samples. 83
Figure 84: Laser Texturing and Sintering process for composite manufacturing. 84
Figure 85: 3D profilometry images and 3D scan of the textured PLA. 85
Figure 86: 3D profilometry images and 3D scan of the reinforced textured PLA. 86
Figure 87: Shore D hardness of the 3D textured samples 87
Figure 88: Time vs COF curves of the textured samples. 87
Figure 89: Average COF values of the textured samples. 88

List of Tables

Table 1: Wt.% of the multi-scaled UHMWPE polymer-based composite materials prepared with MA process [65]. 29
Table 2: Process parameters for 3D printing. 31
Table 3: Three different parameters were used for the experiment of laser texturing on PLLA [70]. 32
Table 4: References and composition of the samples produced in this work by casting. 38
Table 5: Furnace control parameters for casting. 38
Table 6: 3D printing parameters 41
Table 7: The composition and reference of the samples produced in this process. 42
Table 8: 3D printing parameters. 43
Table 9: Composites composition and their name for laser texturing and sintering method .. 43
Table 10: Laser texturing and laser sintering parameters. 44
Table 11: Laser sintering parameters for PST. 44
Table 12: Laser Sintering parameters for PGT and PGST. 44
Table 13: Samples composition produced in this process and their corresponding reference. 58
Table 14: Reference name and their composition of the 3D printed samples. 70
Table 15: Composition of PLA, GNP, and SCF for 3D printed composites using plastography and their reference name. 80
Table 16: Composition and reference name of Samples produced by laser texturing. 85

LIST OF ABBREVIATIONS

Abbreviation	Meaning
CF	Carbon fibre
CFR	Carbon fibre reinforcement
CoF	Coefficient of friction
CNT	Carbon nano tube
DSC	Differential scanning calorimetry
EDS	Electron dispersive spectroscopy
GNP	Graphene nanoplatelets
LST	Laser surface texturing
LVM	Low vacuum melting
MA	Mechanical alloying
MA'ed	Mechanically alloyed
MWCNT	Multiwall carbon nanotube
PCA	Process control agent
PE	Polyethylene
PEEK	Poly (ether ether ketone)
PLA	Poly (lactic acid)
PLDLA	poly (L-co-D, L lactic acid)
PMC	Polymer matrix composite
SA	Stearic acid
SCF	Short carbon fibres
SEM	Scanning Electron Microscopy
SS	Stainless steel
UHMWPE	Ultra-high molecular weight polyethylene
XRD	X-Ray diffraction

1. INTRODUCTION

A variety of materials have been employed in recent years to decrease the debris generated between the sliding surfaces. Metals, ceramics, and polymers are used in hard-on-soft and hard-on-hard bearings, respectively, where soft bearings represent polymers and hard bearings represent metals and ceramics [1]. To date, metallic titanium alloys, CoCr alloys [2], stainless steel [2], and ceramic materials such as alumina and zirconia [3] have been used for various biomedical applications. Because of their numerous features, including bioactivity, degradability, mechanical capabilities, and processing ability, natural and synthetic polymers have been widely used in tissue engineering and regenerative medicine.

In tissue engineering and regenerative medicine, degradable polymers such as PLA, polyglycolic acid (PGA), poly lactide-co-glycolic acid (PLGA), poly-caprolactone (PCL), poly tri-methylene carbonate (PTMC), and their copolymers or mixes are often utilized as scaffold materials [4].

Incorporating metal nanoparticles into a polymer matrix is a straightforward way to take advantage of nanoparticles. The approach in consideration is one of the most effective methods for preventing nano-sized metals from aggregating and preserving their characteristics. In this way, a polymer/metal nanocomposite with a polymer phase that acts as a stabilizer and a protective agent exhibits several important properties. In contrast to traditional composites, the presence of a large polymer-metal interface fundamentally influences polymer attributes such as crystal-ness, glass transition temperature (Tg), and free volume content, and thus contributes more electrical, mechanical, physical, thermal, and chemical properties. The presence of a polymer-metal interface makes the material more advantageous than traditional composite [5]. Polymer/metal nanocomposites can be made in a variety of ways, including mechanical milling and cold compaction, mix melting to blend polymer and metal nanoparticles, in situ polymerization of monomer within metal nanoparticles, in situ reductions of metal salts, and complexes in a polymer matrix and many more ways [6]. By carefully determining and combining polymer and metal pieces, the required nanocomposites may be streamlined. The kind of polymer matrix, content, nature, size, and scattering degree of metal nanoparticles fused in polymer, as well as interaction at the interphase/interface area between polymer and nanoparticles, are all factors that influence the characteristics of polymer nanocomposites [7]. It should be noted that nanoparticles must be adjusted considering the various properties of the polymer matrix to improve nanoparticle adhesion and dispersion [8-10].

Polymers such as proteins (soy, collagen, fibrin gels) or polysaccharides (starch, alginate, chitin/chitosan), polyhydroxyalkanoate (PHA), PLA, and PGA have huge potential in biomedical applications [11,12]. These are biocompatible and degradable to non-toxic parts with a regulated breakdown rate. Polymers that dissolve in water, such as polyethylene glycol (PEG), polyvinyl acetic acetate, poly acrylic acid (PAA), polyvinyl acetate (PVA), and guar gum, have also been used in this field [20]. For example, biosensors with mono- and bi-metallic core shells of sulfonated poly (ether ether ketone) (SPEEK)/Pd, Co, Pt, Ni, and Cu nanocomposites are efficient for detecting glucose [13].

Among all of these, PLA has potential in a range of fields, such as mechanical parts like gears, biomedical engineering and also in electronics engineering. PLA has proved its value as a 3D printable biopolymer, which has been supported by its participation in the global pandemic of Coronavirus Disease of 2019 (Covid-19) [14].

Because of the intrinsic advantages of nano-sized metals, such as large surface area and high moduli, metal nanoparticles often improve the mechanical properties and characteristics of polymers. Furthermore, the establishment of a solid interphase range between the polymer matrix and the nanoparticles facilitates the achievement of significant mechanical properties [15].

Metal nanoparticles, such as Ag, Au, Ti, Bi, Zn, Pt, Pd, and Cu, are commonly used because they have interesting biological, chemical, and physical features. Shape and size have a strong influence on the properties of metal nanoparticles, with small particle sizes, narrow size distributions, and well-stabilized metal nanoparticles demonstrating the optimum condition [16].

Papageorgiou *et al.* [17] performed a study to find the mechanical properties of syndiotactic polystyrene (PS) nanocomposites containing around 3 wt. % of different nanofillers such as multi-wall carbon nanotubes (MWCNT), Cu nanofibre, Ag nano & nanodiamond particles. It was revealed that metal nanoparticles could improve hardness, Young's modulus and impact strength with Ag nano in PS matrix. Mechanical properties were also improved by combining metal nanoparticles in PVA/Ag [18] and another study of chitosan/Ag [19] nanocomposites. As a result, we can conclude that metal nanoparticles can provide numerous advantages in the mechanical characteristics and properties of polymer matrices.

Carbon fibres are useful as reinforcing materials in a variety of matrix materials due to their high modulus, chemical reaction resistance, and the strength-to-weight ratio [20-31]. Carbon fibres are beneficial as reinforcing materials because of their distinctive attributes, which include high tensile modulus, low density, low thermal expansion coefficient, thermal stability,

excellent creep resistance, chemical stability, low electrical resistivity, and high thermal conductivity [32,33]. Carbon fibre reinforced polymer matrix composites have already transformed conventional materials in a variety of applications.

Polymeric matrix composites with graphene and its subordinates as fillers have illustrated the incredible potential for different critical applications, for example, gadgets, environmentally friendly energy vitality, aerospace, and automobile businesses. As previously stated, 2-D graphene has superior electrical, mechanical, and thermal properties, as well as other intriguing elements. It is reasonable to expect some significant changes in a variety of properties in composites containing graphene as a nanofiller. The recent achievement in blending a large amount of graphene has progressed the development of graphene-based composite and crossbreed materials [34].

Many studies have investigated the practicability of graphene as a nanofiller in various polymeric systems, such as epoxy, PS, PANI, PU, poly (vinylidene fluoride) (PVDF), Nafion, polycarbonate (PC), PET, and others [35]. Carbon fibre reinforced polymer matrix is also of great importance for improving the characteristics of the material. SCF and CCF reinforced PLA composites have also been studied to understand the effect on the mechanical behaviour of the composite [36]. The improvement of their characteristics is significant in terms of tribological behaviour, especially friction and wear [37].

2. AIM OF THE STUDY

The goal of this project is to improve the mechanical and tribological properties of PLA polymer. This will be accomplished by creating a self-lubricating reinforced PLA composite with low friction and wear rate, capable of minimizing debris formation and release. Under identical test conditions, the composite's friction and wear properties will be compared to those of pure PLA. There will be three routes for the manufacturing of the samples: 1) casting of mechanically alloyed reinforced PLA, 2) 3D printing from PLA and reinforced PLA filaments produced by mechanical alloying or plastography, and finally 3) laser texturing of PLA, reinforcement of the texture by cold compaction, and laser sintering. The reinforcement materials used in this work are metallic Sn-Zn-Bi alloy, graphene nanoparticles, and short carbon fibres.

3. STATE OF ART

3.1 Poly (lactic acid) (PLA)

PLA is a thermoplastic polyester. The chemical formula of PLA is $(C_3H_4O_2)_n$. PLA is a biodegradable polyester made from lactic acid (LA) or 2-hydroxy propionic acid, which is commonly generated through bacterial fermentation of carbohydrates from agricultural products like maize, potatoes, and cassava [36]. PLA manufacturing procedures include injection moulding, film extrusion, blow moulding, thermoforming, fibre spinning, and film-forming. Packaging, textile, biomedical, structural, and automotive are just a few of the industries where PLA-derived products have been used [38]. PLA polymers have a glass transition temperature of 60–65 °C, a melting temperature of 130–180 °C, and Young's modulus of 2.7–16 GPa, ranging from amorphous glassy polymer to semi-crystalline and highly crystalline polymer [39-41]. PLA can tolerate temperatures of up to 110 degrees Celsius [42].

PLA has grown in popularity because of its cost-effective production from biodegradable materials. PLA has the second greatest volume of usage of any bioplastic in the world. It covered 65% of the market share of bioplastics in 2020 [43]. In 3D printing, PLA is one of the most extensively used plastic filament materials.

The use of natural fibre to reinforce PLA composites is a crucial aspect of boosting biocomposites' mechanical uses. Furthermore, bio polyester PLA is the biodegradable polymer with the biggest variety of utilization for industrial demands among biodegradable polymers [38]. PLA has attracted a lot of interest as a polymeric scaffold for drug administration because of its biocompatibility and biodegradability. As PLDLA/TCP scaffolds for bone engineering, a composite blend of poly PLDLA and tricalcium phosphate (TCP) is utilized [44, 45].

3.2 Polymer Matrix Composites

Metal matrix composites (MMC), ceramic matrix composites (CMC), and polymer matrix composites (PMC) are three main types of composites used in a variety of engineering applications. The best properties of two or more heterogeneous materials are combined in composite materials [46,47]. Composites are made up of two basic components: reinforcement and matrix. The properties of composite materials are determined by the type of reinforcement and matrix materials used, as well as the manufacturing techniques [48].

A PMC is a material made up of short or continuous fibres that are held together by an organic polymer matrix. PMCs are used to transfer loads between matrix fibres. The lightweight, high

rigidity, and high strength along the direction of their reinforcements are just a few of the benefits of PMCs. Abrasion resistance and corrosion resistance are two further advantages. The matrix in PMCs is responsible for bonding the fibres together and transferring loads between them [49]. Thermosets or thermoplastics are commonly used as PMCs matrices. Thermosets are by far the most common variety today. Epoxies, phenolics, polyurethanes, and polyimides are among the resin systems used in thermosets. Epoxy solutions are currently the most popular in the advanced composites industry [50-52]. Fibre-reinforced PMCs have a volume of around 60% reinforcing fibre. Fibreglass, graphite, and aramid are some of the most prevalent fibres found and employed in PMCs [49]. Nanomaterials reinforced PMCs, unlike fibre-reinforced PMCs, can produce considerable improvements in mechanical characteristics at much lower loadings (less than 2% by volume) [53]. The mechanical properties of virgin graphene are like those of carbon nanotubes. Solution processing, melt processing, or in-situ polymerization are commonly used to process graphene PMCs in the same way that carbon nanotube PMCs are produced [54].

3.3 Polymer matrix composites processing routes

Figure 1 depicts the major processing routes for polymer matrix composites. Thermosets and thermoplastics are the two types of polymer matrices presented. A thermoset begins as a low-viscosity resin that reacts and cures during processing, resulting in an impenetrable solid. A thermoplastic is a high-viscosity resin that is heated above its melting point to be processed.

A thermoset resin cannot be reprocessed by reheating because it sets up and cures during processing. A thermoplastic, on the other hand, can be reheated above its melting temperature for further processing. For both groups of resins, some procedures are better suited to discontinuous fibres, and others are better suited to continuous fibres [55].

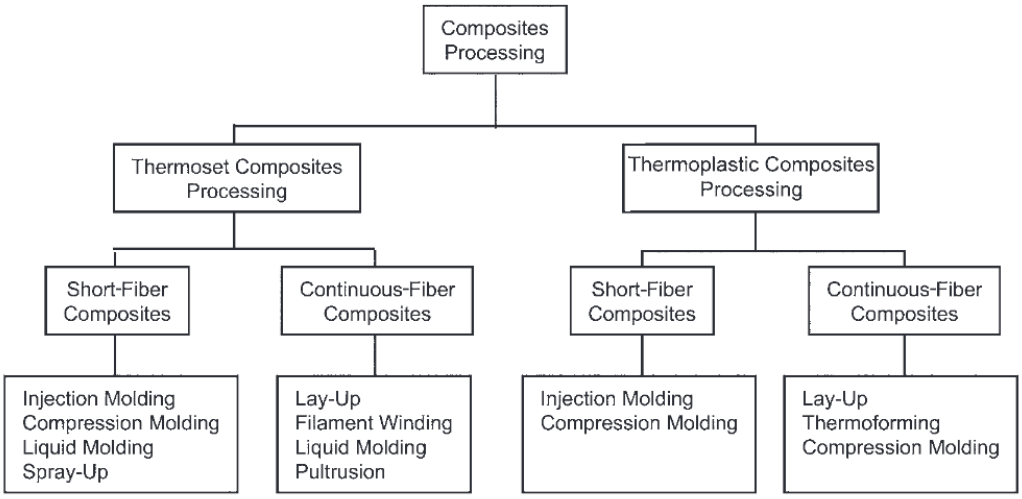

Figure 1: Major polymer matrix composite fabrication processes [55]

3.4 PLA-based composite material

Due to growing concerns about decreasing resources and increased pollution, interest to produce biopolymers has gained a lot of traction in recent years.

PLA is one of the most widely produced biopolymers in the world, making it an excellent candidate for product commercialisation with a global capacity of over 211,000 tons in 2020 [56].

Hinchcliffe *et al.* [57] combined theoretical and practical work on pre-stressed natural fibre reinforced PLA composites. The mechanical characteristics of PLA were improved in the study by adding additives. In comparison to solid non-reinforced PLA composites, the PLA reinforced composite had a 116 % increase in tensile strength and a 12% increase in flexural specific strength.

PLA matrix composites reinforced with magnesium (Mg) alloy have become more commonly available for usage in biomedical applications. The addition of Mg particles to PLA/Mg composites has been proven to increase the mechanical properties of the composites. At the same time, the PLA lowers Magnesium's rapid breakdown rate and H_2 emission [58].

3.5 PLA-based composite tribological behaviour

MWCNTs and GNPs were investigated as nanocomposites in PLA using the melt extrusion method [59]. To understand the tribological behaviour of the composite, the characterisation of the scratch and wear conditions, as well as the morphological aspects of the composite materials were investigated. As an initial phase in the procedure, the materials were created using the melt extrusion method. Filaments suitable for 3D printing were created from the

obtained pellets, which had a nanofiller loading of up to 12 wt.%. Scratch tests with a micro-cutting diamond blade were done using a constant normal force of 2 N. Scratch resistance of the 12 wt.% GNP/PLA nanocomposite was found to be twice as great as the plain PLA applied as a standard [59].

At the relevant applied normal force of 2 N, the addition of GNPs resulted in significantly better tangential force (Fx) and, as a result, higher COF and scratch-resistance of the PLA-based nanocomposites that we can observe in Fig. 2. This was due to the filler forming a network structure that prevents the diamond blade from passing through the sample. With CNT monofiller, the COF was significantly lower.

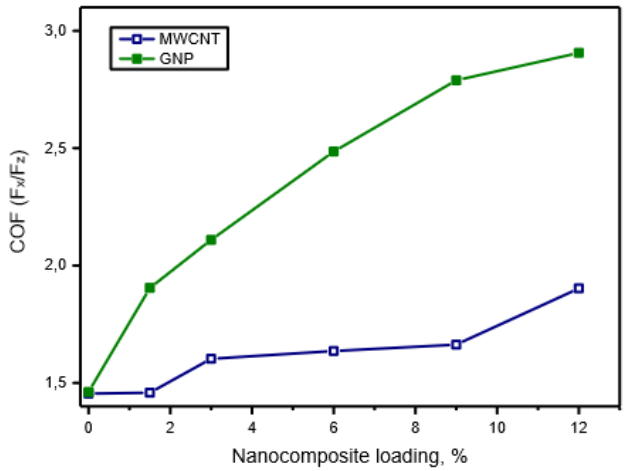

Figure 2: COF dependence on carbon monofiller content in PLA-based nanocomposites (scratch test data) [59].

Batakliev *et al.* [59] investigated the wear behaviour of carbon monofiller nanocomposite samples in comparison to pure polylactic acid, as shown in Fig 3. All the wear tests were carried out for a total of 300 seconds.

In Fig. 3, the coefficient of friction parameters indicated average values for the entire test period. Pure PLA had a higher COF, ranging from 0.15 to 0.16, whereas GNP and CNT-containing composite samples had lower COF values, ranging from 0.10 to 0.11.

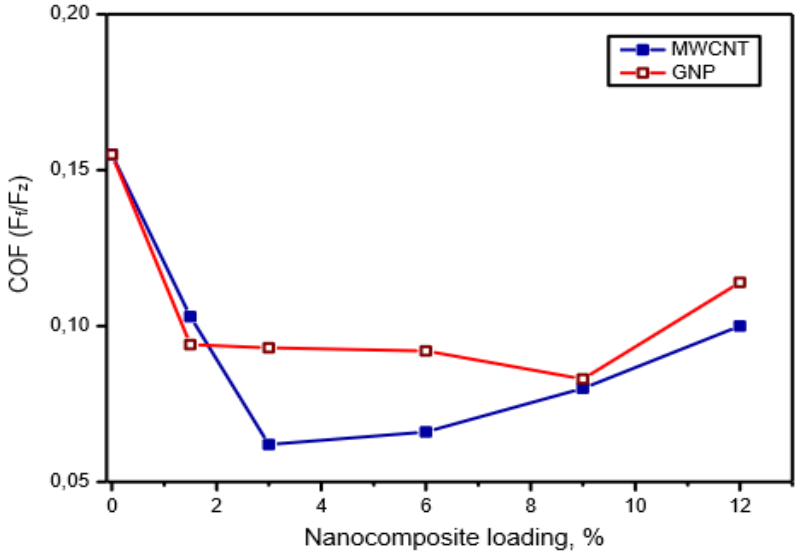

Figure 3: COF dependence on carbon monofiller content in PLA-based nanocomposites (wear test data) [59].

In the same work, the amount of reinforced materials was also increased up to 3 and 6 wt.% (Fig. 4). When compared to the clean PLA, there was a significant drop in COF reaching a value of 0.07 up to 3 wt.% MWCNT loading. With mono filler of 3 and 6 wt.% of GNP or CNT or a mixture of both, the COF value was significantly lower than pure PLA. 3 wt.% of MWCNT gave the smallest value of COF which can be described by the self-lubricating property of CNT. But the 1.5 wt.% of GNP and CNT increased the COF value in comparison with the monofiller system. A significant decrease in COF value was found for the GNP and CNT reinforced (6 wt.%) samples.

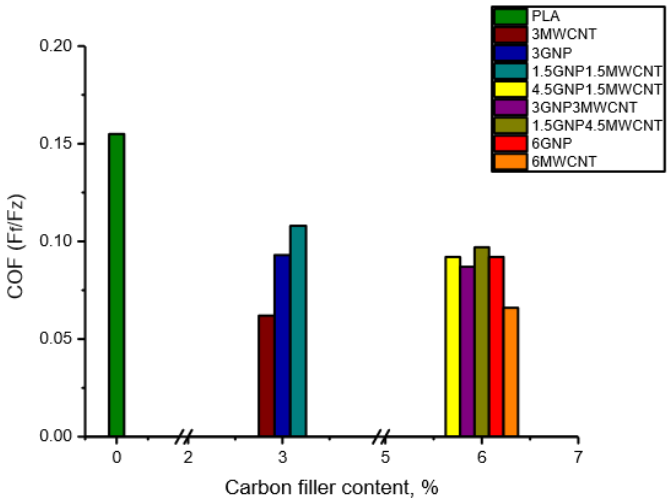

Figure 4: COF dependence on 3 and 6 wt.% monofiller and bifiller content in PLA-based nanocomposites [59].

The amount of reinforced materials was increased up to 9 and 12 wt.% (Fig. 5). The result was the same as expected. The COF value was lower than pure PLA for both cases though the 12 wt.% filler system has a slightly higher COF value than the 9 wt.% system.

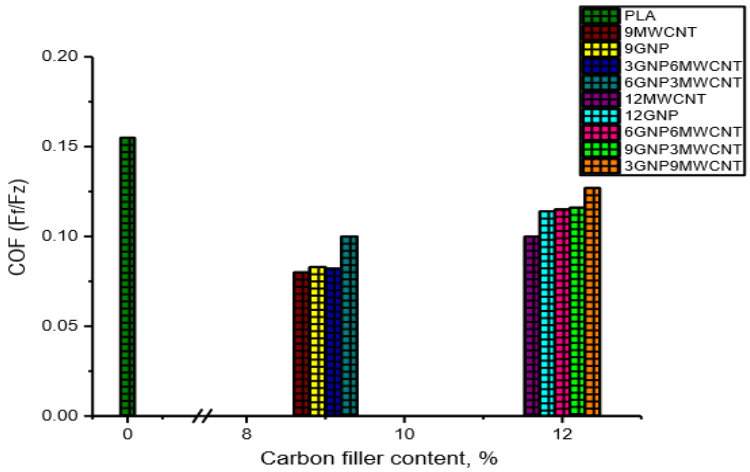

Figure 5: COF dependence on 9 and 12 wt.% monofiller and bifiller content in PLA-based nanocomposites [59].

Maqsood *et al*. [60] investigated the mechanical properties of pure PLA and PLA with CCF, SCF, and a mixture of CCF and SCF. In his study, he used fused deposition modelling (FDM) to produce all the samples. He produced and compared the properties of four sets of specimens. The following four sets of specimens were created using FDM technology: PLA, PLA with SCF (PLA-SCF), PLA printed with CCF (PLA-CCF), and PLA-SCF printed with CCF (PLA-SCF-CCF). After the FDM fabrication process, the effects on the tensile and flexural characteristics of specimens were studied experimentally. From Fig. 6, PLA composite with CCF and the mixture of CCF & SCF had a greater slope of the stain-stress curve. Their tensile stress was significantly higher for them than pure PLA and PLA-SCF composite.

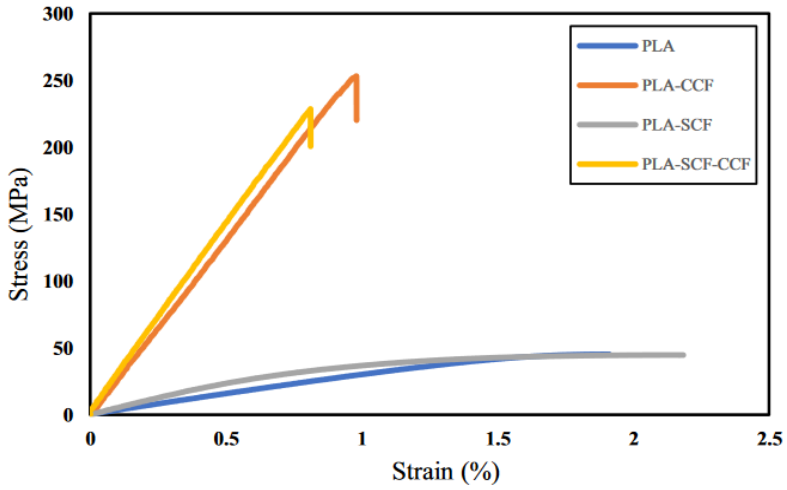

Figure 6: Average tensile stress-strain curve for PLA and PLA-based composites [60].

From the results obtained by Maqsood *et al*. [60], it was obvious that the tensile strength (Fig. 7 a) and Young's modulus (Fig. 7 b) increased 5 times with the PLA-CCF and PLA-SCF-CCF composite than with pure PLA and PLA-SCF composite. The Young's modulus of PLA-SCF

composite was also higher than pure PLA. Ductility (Fig. 7 c) was higher for pure PLA and PLA-SCF composite.

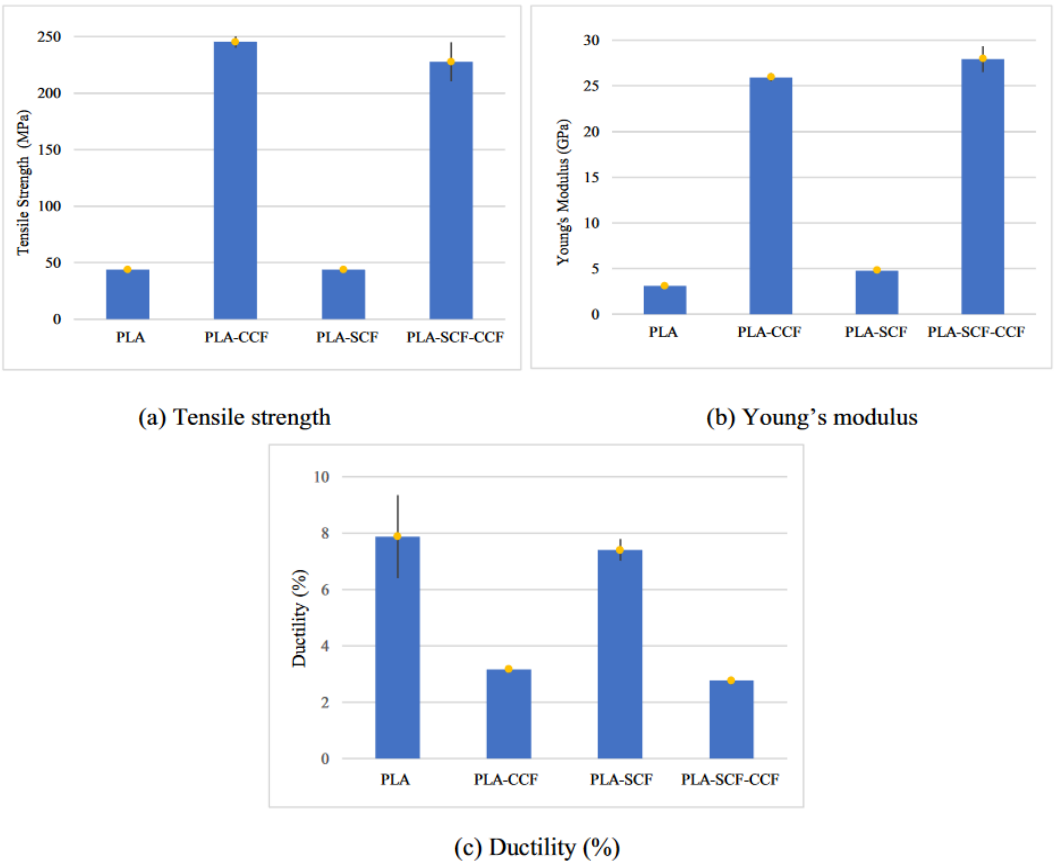

Figure 7: Results of tensile properties of 3D printed PLA and PLA-based composites [60].

A similar result was obtained from flexural tests. The stress-strain curve (Fig. 8) depicted higher stress for PLA-CCF and PLA-CCF-SCF composite than the other two systems. The flexural stress and flexural modulus increased with the PLA-CCF and PLA-SCF-CCF composite (Fig. 8). The flexural modulus of the PLA-SCF composite was also higher than the pure PLA.

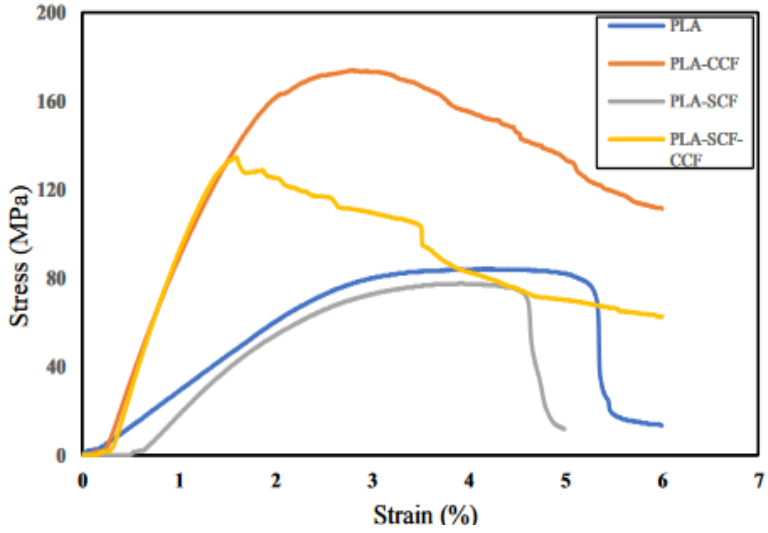

Figure 8: Average stress-strain curve for PLA and PLA-based composites from flexural test [60].

Figures 9 a, and b exhibit the flexural stress and flexural modulus of PLA-based 3D printed samples. The flexural stress and flexural modulus were much higher for PLA-CCF and PLA-SCF-CCF composites than for pure PLA and PLA-SCF composites. Flexural stress (Fig. 9 a) was even lower for PLA-SCF than pure PLA though the opposite result is obtained for flexural modulus (Fig. 9 b).

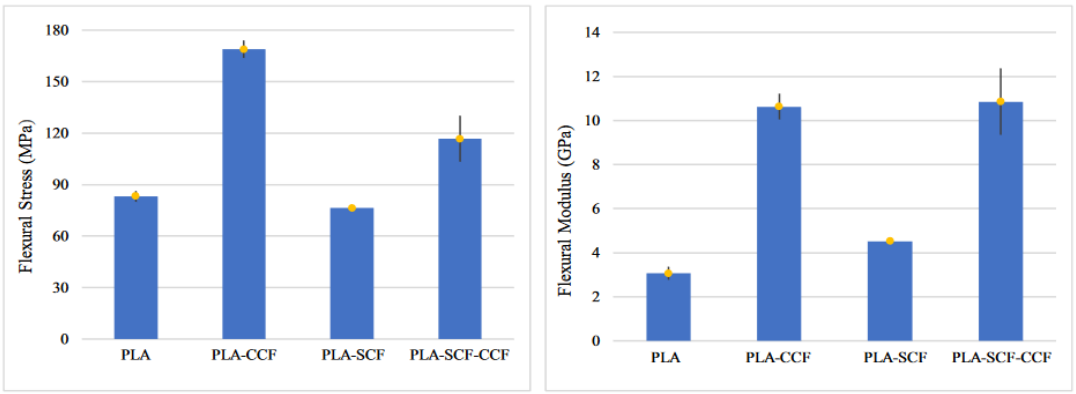

Figure 9: Results of flexural properties of PLA and PLA-based 3D printed composite samples [60].

Valapa *et al.* [61] studied the influence of graphene on the tensile properties of PLA and showed that the PLA-graphene composite has higher tensile strength than PLA and it is more effective when the graphene percentage is at the lowest quantity which is depicted in Figs. 10 a, and b.

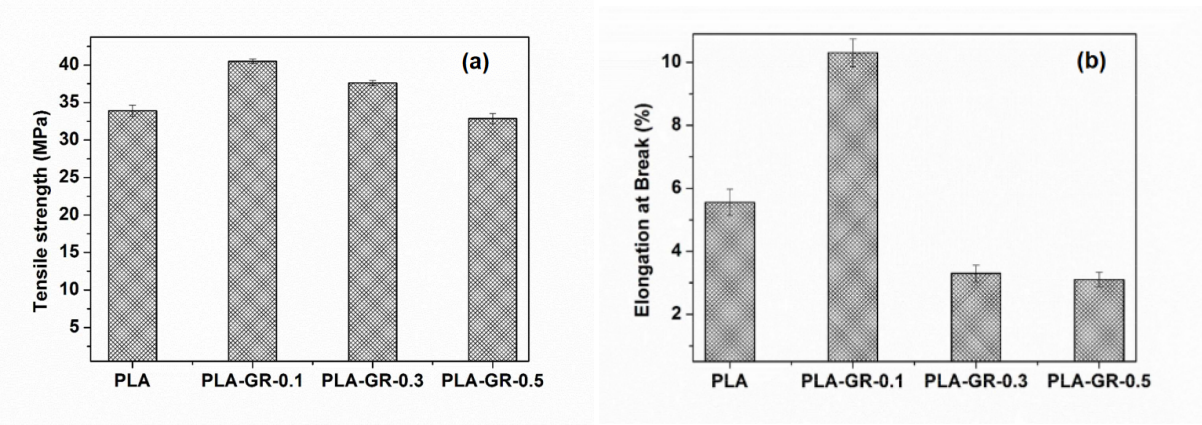

Figure 10: Tensile strength (a), and elongation-at-break (b) for PLA and PLA-GR nanocomposites [61].

Figures 11 a and b represent the TEM images of bi-filler composites with total filler contents of 6wt. % (a) PLA/1.5wt. % GNP/4.5wt. % MWCNT and (b) PLA/3wt. % GNP/3wt. % MWCNT. Figures 11 a and b depict good bi-filler dissemination at both combined concentrations. Both fillers appear to form an interconnected network of particles and small aggregates, with single nanotubes, small MWCNT aggregates, and GNPs forming an interpenetrated network of particles and small aggregates. The combination of the two nanofillers in the PLA matrix resulted in the possibility of a unique synergetic effect for improving electrical and mechanical properties [62].

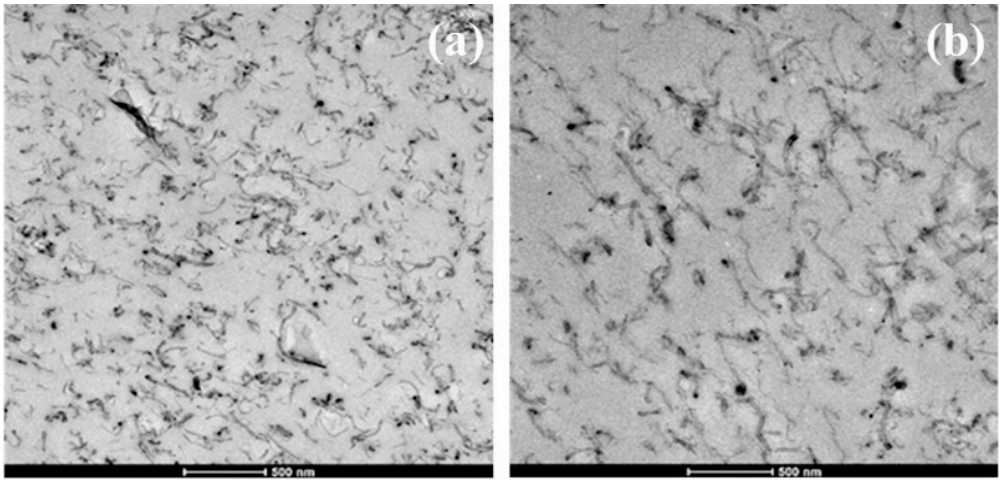

Figure 11: TEM images of the bi-filler composites containing (a) polylactic acid (PLA)/1.5wt.% GNP/4.5wt.% MWCNT and (b) PLA/3 wt.% GNP/3 wt.% MWCNT, respectively [62].

Typical thermoplastic polymers are electrical insulators. Polymers that contain electrically conductive reinforcement exhibits electric conductivity like semiconductors or metals. From Fig. 12, we can see that with increasing filler element, electric conductivity increases for both

the system (mono filler or bi filler composites) [62]. This behaviour can be utilised to develop biosensors.

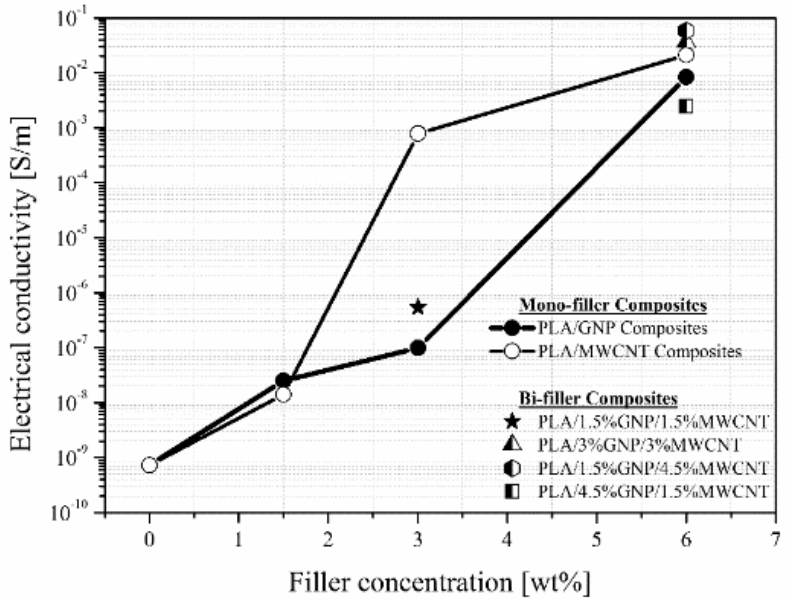

Figure 12: Electrical conductivity vs. GNP and MWCNT filler content for mono-filler (PLA/GNP and PLA/MWCNT) and bi-filler (PLA/GNP/MWCNT) composites [62].

3.6 Mechanical Alloying

MA is a one-of-a-kind technology for creating alloys and composites that are unlikely to achieve using traditional procedures like melting [63]. This process was first used to make oxide-dispersion enhanced nickel alloys in the 1960s. Its application, however, is no longer confined to the manufacture of metal alloys. Shaw *et al*. [64] were the first to examine the use of MA to make polymeric alloys without the use of chemical reagents in 1988. poly amide (PA) pellets were mechanically alloyed at -150°C in a high-energy shaker ball mill in this work. After 24 hours of MA, the PA particles had been refined from huge uneven particles to small layer structure particles.

3.6.1 Polymer-based composites produced by MA

Multi-scaled composite materials are important because they have better mechanical properties than materials made with traditional fillers or polymer mixes. Composite materials based on UHMWPE, quasicrystals, polyimide, and bronze were studied for usage in machine moving parts, gears, bearings, and sliding elements in a study done by Kaloshkin *et al.* [65].

The major goal was to look at the process of fabricating these composite materials and see if they are repeatable and reliable in an industrial setting. Kaloshkin *et al.* [65] produced multi-scaled UHMWPE polymer-based composite materials by mechanical alloying (Table 1). A planetary mill was used to prepare the samples. The authors showed that the quasicrystalline

phase was dissolved into an intermetallic solid solution when milled with bronze; however, milling with polymers preserved the quasicrystalline phase, whereas UHMWPE crystallized throughout the milling process. The tribological properties (Fig. 13) showed better results for composite materials with QC/bronze-based filler than for polyimide. However, they had a higher density than UHMWPE and a lower coefficient of friction than the other compositions. They also had superior abrasion resistance and a lower coefficient of friction than the other compositions. As a result, it appeared that a compromise between strong abrasion resistance and low density will be required for applications in moving parts, bearings, and gears. The polyimide-based specimen outperformed pure UHMWPE and QC/bronze-based filler in terms of strength and hardness. This research had also demonstrated that mechanical alloying may be used to manufacture composite materials with acceptable characteristics for use in weary conditions.

Table 1: Wt.% of the multi-scaled UHMWPE polymer-based composite materials prepared with MA process [65].

Sample I		Sample II		Sample III		Sample IV	
Component	wt%	Component	wt%	Component	wt%	Component	wt%
Quasicrystal	13	Quasicrystal	20	Quasicrystal	15	Quasicrystal	20
Polyimide	37	Polyimide	30	Bronze	35	Bronze	30
UHMWPE	50	UHMWPE	50	UHMWPE	50	UHMWPE	50

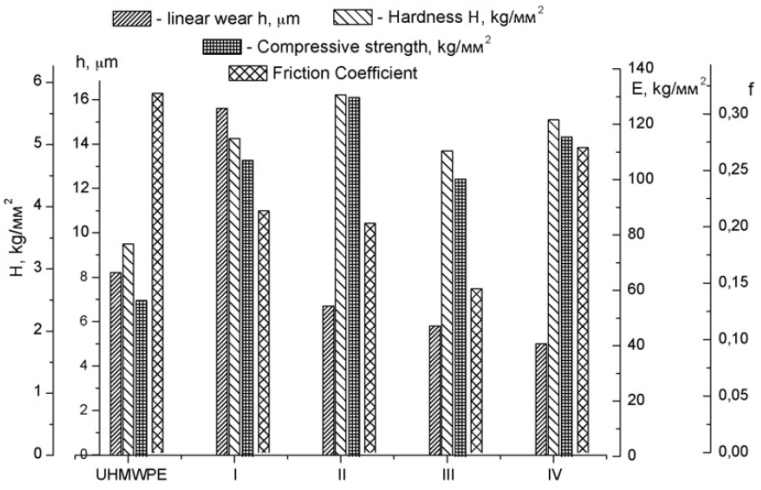

Figure 13: Mechanical and tribological properties of the reinforced UHMWPE samples [65].

In another work, for dental implant use, Souza *et al.* [66] examined the friction and wear behaviour of two PEEK matrix composites filled with natural amorphous silica fibres (PEEK-NASF) and particulate zirconium-lithium silicate glass fibre (PEEK-LZSA). MA of PEEK powder with varied contents (10, 20, and 30% mass. percent) of either of the fillers at 150 rpm for 24 hours using zirconia balls produced the PEEK-based composites. Hot pressing at 2 bars compressed the milled powders into cylinders, which were subsequently sintered slightly above

the melting point of PEEK and held at 4 bars for 4 seconds. The COF of the composites did not improve when compared to unfilled PEEK, hence the tribological outcomes from this investigation were not positive.

There are very few works done on producing PLA composite with the mechanical alloying process. One study showed that polylactidebacterial cellulose nanocrystals (BCNC) nanocomposites were developed by the ball milling method. It was found that the thermal stability of the PLA nanocomposites was not affected by the addition of BCNC [67].

Regardless of the nanofiller quantity, PLA films containing nanocellulose had better Young's modulus and tensile strength, as well as lower elongation at break, than plain PLA films. It's worth noting that the film with the minimum BCNC concentration (0.5%) had the largest reinforcing effect, which was most likely due to greater nanofiller redistribution within the polymeric matrix [67]. The storage modulus was used by Ambrosio-Martín *et al.* [67] to investigate the load-bearing capability of neat PLA and BCNC-containing nanocomposites produced using ball milling. Figure 14 depicts the results. When compared to neat PLA, the storage modulus of PLA nanocomposite films improved over the whole temperature range.

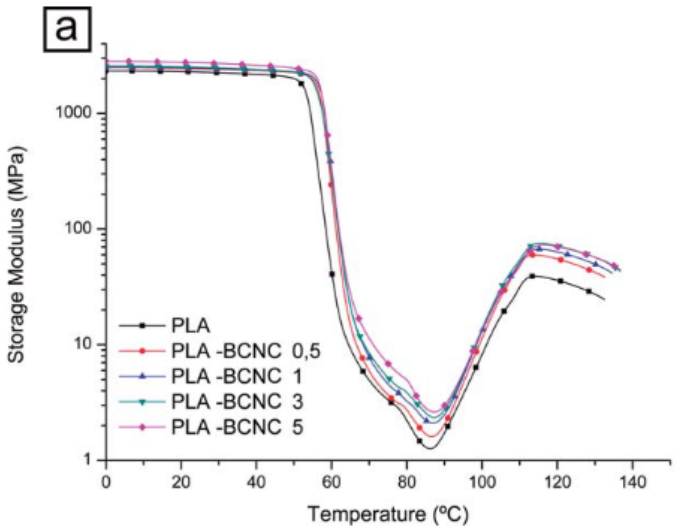

Figure 14: Storage modulus plot versus temperature for neat PLA and its nanocomposites films with BCNC [67].

In Fig. 15, the composites containing BCNC had a significant reduction in oxygen permeability, implying that the well-distributed fraction of crystal-line nanofillers effectively blocked oxygen flow. However, the greatest reduction was seen with the least nanocellulose content, emphasizing the importance of dispersion to optimize performance improvements for this type of composite.

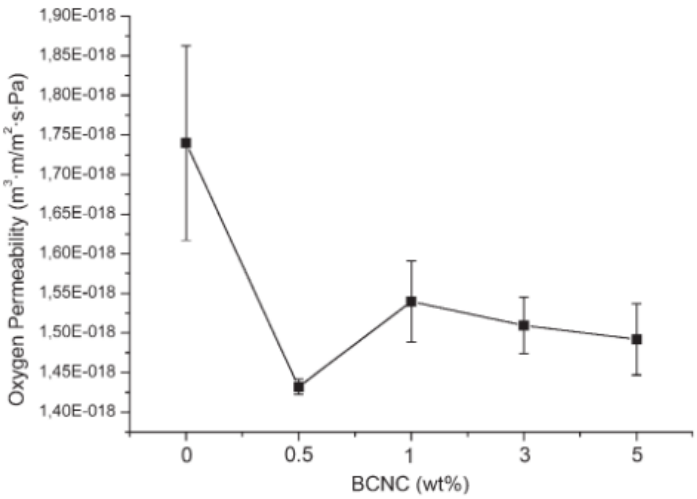

Figure 15: Oxygen permeability at 80% RH for neat PLA and Its nanocomposites with BCNC prepared by ball milling [67].

3.7 3D printing of PLA-composite

3D printing is a potential technique to create thermoplastic parts with complicated geometries, significant design flexibility, recyclability, and minimal material waste [68].

For polymer composite, FFF (fused filament fabrication) 3D printing is one of the most well-known used methods. There are studies on metal/polymer composite filament production and 3D printing to enhance the properties of the polymer [69]. Caminero *et al.* [68] studied PLA composite where graphene nanoplatelets were reinforced into PLA matrix to study the mechanical properties of the composite and the composite samples were produced by 3D printing. The parameters used in 3d printing during the study are given in table 2.

Table 2: Process parameters for 3D printing.

Parameters	Value
Layer thickness (mm)	0.12
Feed rate (mm/s)	50
Flow rate (mm^3/s)	4.8
Top and Bottom thickness (mm)	0.6
Nozzle temperature (°C)	210
Nozzle size (mm)	0.4

In terms of tensile and flexural stress, it was shown that samples made of PLA-Graphene composites performed the best overall. However, the PLA-Graphene composite samples' impact strength tended to decline with the inclusion of GNPs. Additionally, the PLA-Graphene composite specimens' general dimensional correctness was unaffected by the insertion of graphene nanoplatelets. Additionally, PLA Graphene Composite samples displayed the best overall surface texture performance (Fig. 16), especially when pieces were printed flat and on the edge. The encouraging findings of this work demonstrate the viability of 3D printed PLA-

graphene composites for possible usage in a variety of applications, including biomedical engineering. [79].

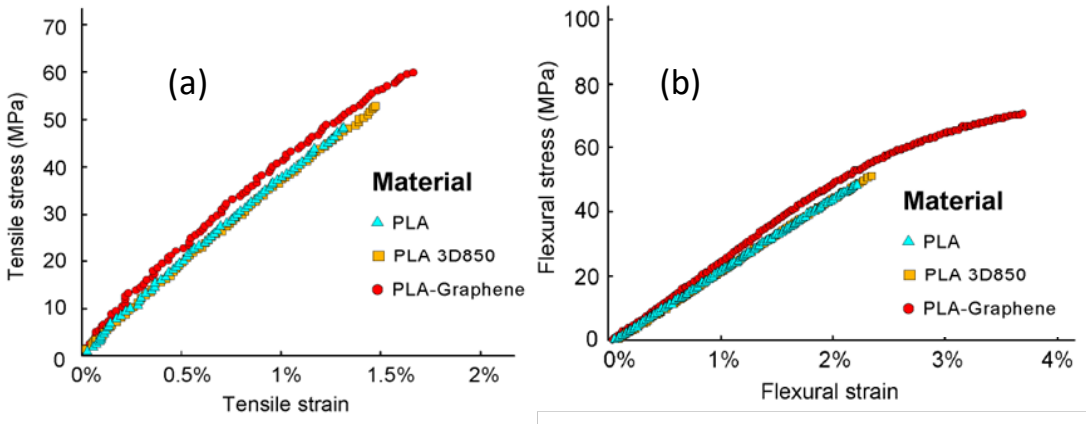

Figure 16: Tensile stress-strain curves (a) and Flexural stress-strain curves (b) for the 3D printed PLA and PLA-Graphene composite samples [68].

3.8 Laser texturing of PLA

Laser texturing is another method that was used by Tomanik *et al.* [70] to influence the micromechanical and biological properties of the poly L-lactic acid (PLLA) surface.

Three different laser parameters were used for the experiments as shown in table 3. The authors showed that laser-based technologies are widely used for patterning and/or texturing polymer surfaces. They showed how CO_2 laser irradiation affected the surface microhardness, roughness, wettability, and cytocompatibility of PLLA thin films. The experiments reveal that CO_2 laser texturing of PLLA allows for the adjustment of the structural and physical properties of the PLLA surface to the needs of the cells despite substantial changes in the mechanical characteristics of the laser-treated surface polymer.

Table 3: Three different parameters were used for the experiment of laser texturing on PLLA [70].

Specimen	Optical Power P (W)	Scanning Speed V (cm/s)	Hatching (Line-to-Line Space) h (μm)	Pulse Repetition Rate (PRR) (Hz)	Pulse Energy E_i (mJ)	Accumulated Fluence F_A (J/cm^2)
Reference	-	-	-	-	-	-
F_1	0.447				15.5	24
F_2	0.867	7.1	25.4	2.8	31.0	48
F_3	1.286				45.8	71

A microscopic examination (Fig.17) of the surfaces of the irradiated specimens revealed the presence of repeated structures.

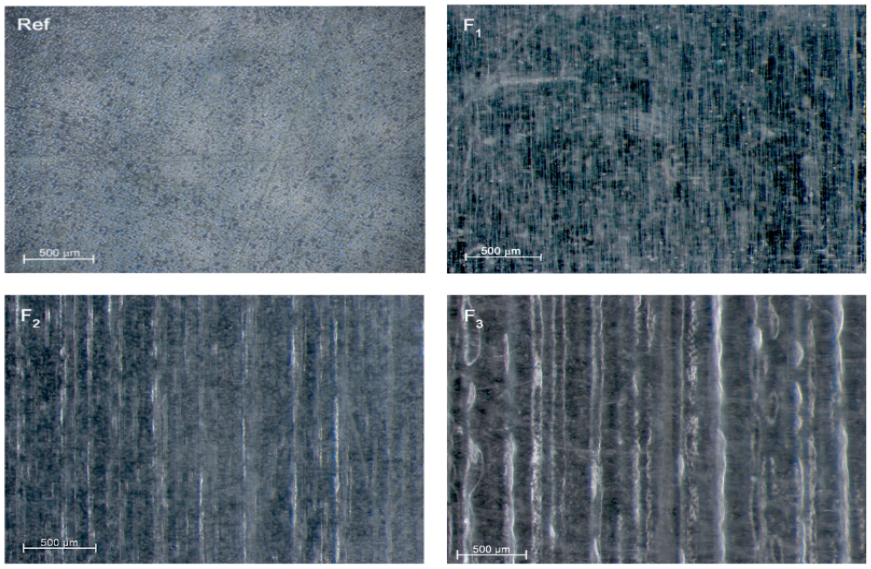

Figure 17: Microscopic images of the obtained surfaces (magnification 100) recorded for reference material (Ref) and laser-treated with accumulated fluences of 24 J/cm2 (F1), 48 J/cm2 (F2) and 71 J/cm2 (F3) [70].

The observed micro-patterns grew larger as the laser irradiation settings were raised. Increased utilization of accumulated flux formed micro-grooves, making the surface progressively rough, according to the surface roughness profiles determined.

The surface of PLLA is hydrophobic. An increase in the used accumulated fluence was characterized by a reduction in the contact angle during the surface laser structuring process, resulting in better wetting (wettability) of the material and higher surface roughness. The larger surface roughness and changing relationships between polar and nonpolar functional groups, as well as between acidic and basic sites available at the modified surface region, were partly responsible for the observed decrease in the contact angle of water wetting increasing surface hydrophilicity. They also had better adhesion when the surface roughness is increased. The use of laser treatment to significantly increased surface roughness allows for an increase in bone-forming cell proliferation and differentiation. The formation of nano or micropatterns on aliphatic polymer surfaces after laser irradiation was associated with an increase in roughness. The PLLA surfaces that had been irradiated had parallel and equidistant grooves and ridges. The pattern repeated itself, and as the fluence of the laser increased, the distance between every two adjacent ridges grew. Waugh *et al*. [70] discovered an improvement in the biocompatibility of CO_2 laser-treated surfaces. As the infrared spectroscopy revealed the presence of a vinyl group in PLLA irradiated with higher laser fluences, a biological test to determine the material's cytotoxic effects were required. The examined polymers had no cytotoxic activity, according to the biological evaluation.

In Fig. 18, the relation between the indentation force and the depth was observable. The significant finding was that the polymer's mechanical parameters were changed from stiff (F1, F2) to compliant (F3) while the surface topography and wettability were also altered. The PMC's reinforcement shielded the polymer matrix from abrasion by generating a transfer film on the counter surface.

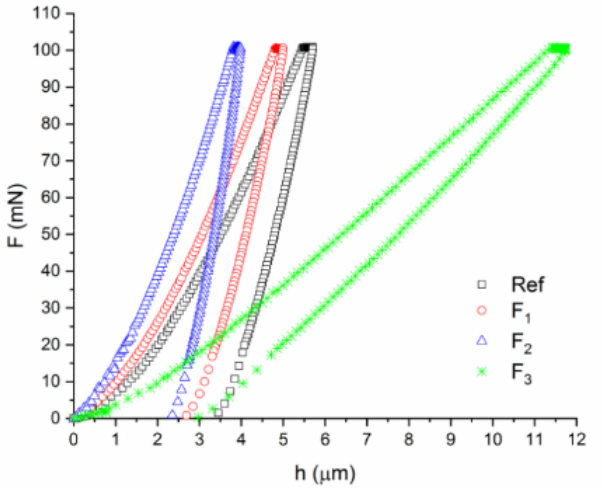

Figure 18: Typical loads vs. indentation depth curves for reference material (Ref) and laser-treated with accumulated fluences of 24 J/cm2 (F1), 48 J/cm2 (F2) and 71 J/cm2 (F3) [70].

4. RESEARCH GAP AND OBJECTIVE

In the field of PMCs, there is a lack of studies concerning their reinforcement by GNP, SCF, or metallic alloys. In a previous study (not published) performed by Crystal Emonde, (on the aim of the Tribos+ master thesis) a PEEK material was reinforced with Sn-Zn-Bi, SCF, and GNP. The mechanical and tribological behaviour of the samples were assessed. In this study, we are interested to change PEEK to PLA.

PEEK is a popular material for biomedical use, especially for implants. But pure PEEK, as well as PEEK-based composites, have the same issue of bio inertia and the general mechanical properties of PEEK-based composites are not quite impressive [71]. In the previous study, the mixture of the reinforcement and the polymers were not homogeneous. There was another issue of porosity in the PEEK-based composites.

On the other hand, PLA is considered because of its properties such as nontoxicity, biocompatibility, biodegradability, mechanical properties, and processability. PLA is thus an environmentally friendly, non-toxic polymer with properties that allow it to be used in the human body. Blending PLA with other polymers and materials is also quite easy and provides simple ways to improve associated properties or create novel PLA polymers/blends for target applications [72]. Moreover, PLA has a lower glass transition and melting temperature than PEEK which will help the heat treatment process to reduce the porosity of the composite.

The main objective of this project is to study the influence of different reinforcements (Zn-Sn-Bi alloy, GNP, and CSF) on the mechanical and tribological properties of PLA. Three approaches will be used: 1) mechanical alloying of the metallic elements, mechanical alloying of the PLA + reinforcement, and casting, and 2) mechanical alloying / plastography of reinforcement + PLA, filament extrusion, and 3D printing, and 3) Laser texturing, reinforcement of the texture by cold compaction, and laser sintering.

The structural, morphological, mechanical, and tribological behaviour of the different samples will be assessed by different techniques to determine the most suitable compositions for increasing the aforementioned properties.

5. EXPERIMENTAL DETAILS

In this section, the manufacturing processes and the experimental parameters used to produce the different samples are described. Besides, a brief description of the characterisation techniques used in this work is also included.

5. 1. Manufacturing processes

5.1.1. Mechanical alloying procedure

Mechanical alloying was chosen as a solid-state powder processing technique because it allows the mixing of metallic powders and coating the PLA with different reinforcements.

The MA procedure begins with the proportional mixing of powders (with a typical range of sizes ranging from 1 to 500 microns) [73] and their transportation to the vial with the grinding balls. Depending on the morphologies, such as metallic powders, intermetallic compounds, or dispersoid powders, and the character of the components within mixtures, such as ductile-ductile, ductile-brittle, or brittle metal powders, different alloys can be created [74].

A high-energy planetary ball mill (Frisch Pulverisette 6) was chosen to undertake the mechanical alloying of the components because of its adaptability in milling ductile and brittle components at high velocities. This mill consists of bowls, often known as vials, set on a revolving disk, and rotated along their axes by a specific drive system. The contents of the vials are affected by the centrifugal forces generated by the revolving disk around its axis and the autonomous turning of the vials (powders and balls). The centrifugal force is synchronized and opposed since the disk and vial rotate in opposite directions [73]. As shown in Fig. 19, grinding is caused by frictional forces between the grinding balls and the vial wall, followed by a high-energy collision of the balls and powder as they are lifted off the vial's surface and hit by the opposite wall at a high speed.

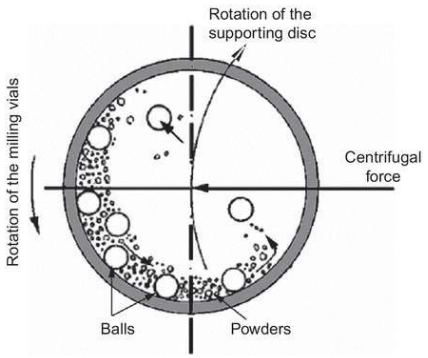

Figure 19: Planetary ball milling mechanism [75].

Ball-powder-ball collision, on the other hand, alters the morphology of metal powder in two ways, depending on the sort of constituent particles. When the clean surfaces of the ductile components in the powder overlap, cold welding occurs, resulting in the creation of layered composites. The brittle components, on the other hand, are typically confined in the composite and occluded within the ductile components [73, 76]. The layered composites deform into convoluted lamellae when the two processes of cold welding and fracture occur, and the microstructure of the powder becomes increasingly refined [76].

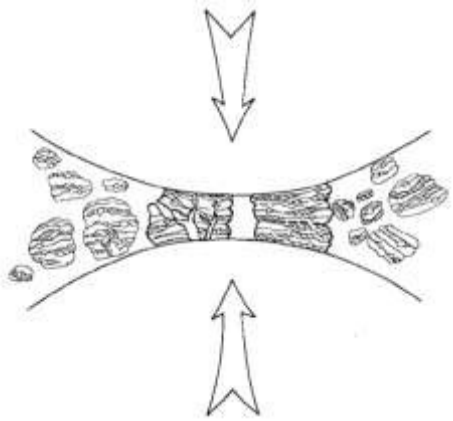

Figure 20: Ball-powder-ball collision of metal powders during MA [76].

Due to substantial plastic deformation, the hardness of the particles increases approximately linearly with time as MA proceeds. The agglomerated powders fracture into smaller particles as the milling time is increased. Lamellae are no longer resolvable by optical microscopy at this point, and milling is no longer possible [76].

Mechanical alloying of brazing alloy

The alloy was prepared in concentrations of 89wt.% Sn, 8wt.% Zn, 3wt.% Bi. Besides, 1wt.% of stearic acid was added as a PCA to prevent excessive cold welding of all mixtures. The powder to ball ratio used for milling was 20:1. 15 SS balls were used with a diameter of 18.5mm and 32 g of the weight of each ball. A planetary ball mill (Frisch Pulverisette 6) was used for milling, using a speed of 300 rpm and various grinding times. The vials were opened after 1, 3, 5, 10, 15, 20, and 25 h to collect a bit of powder for characterisation.

Mechanical alloying of PLA-based polymer matrix composite

PLA granules supplied by Goodfellow having an average diameter of 4.85mm and density of 1.25 g/cm3 were used during the research. In total, eight composite mixtures were produced

(Table 4). The relative amount of SCF and GNP in samples containing these two reinforcements was 50-50.

Table 4: References and composition of the samples produced in this work by casting.

Samples	Short Name	Samples	Short Name
PLA	PLA	PLA-Alloy	PA
PLA-SCF	PS	PLA-SCG-Alloy	PSA
PLA-GNP	PG	PLA-GNP-Alloy	PGA
PLA-SCF-GNP	PSG	PLA-SCF-GNP-Alloy	PSGA

The milling parameters were the same as before mentioned in the 5.1.1 (Mechanical alloying of brazing alloy) section, but the milling time was 10 minutes for all the samples.

Figure 21: Planetary ball mill (Frisch Pulverisette 6)

5.1.2. Casting

For the casting process, a mould of 4 mm diameter was used. 4.6g of the PLA granules or the PLA composites were poured into the mould and then it was placed inside the furnace. Casting process parameters are shown in Table 5.

Table 5: Furnace control parameters for casting.

Parameter name	Value
Initial temperature	25°C
Casting temperature	200°C
heating rate	5°C/min.
Final temperature	35°C

A schematic diagram of the casting process is shown in Fig. 22. The samples were produced by melting the PLA at 200ºC for 1h. A slow cooling process was used to maintain the crystallinity of PLA.

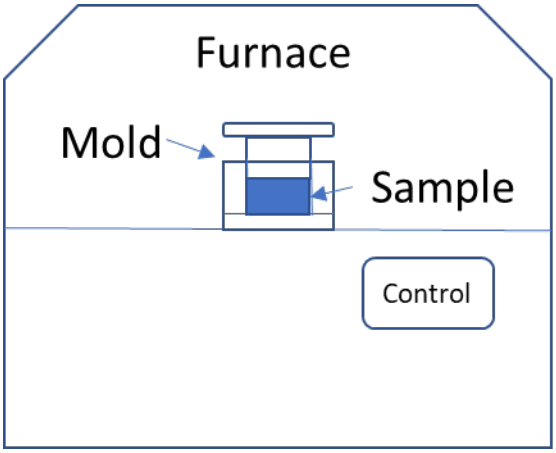

Figure 22: Schematic diagram of the casting process.

5.1.3. 3D printing Procedure

Extrusion

Plastic extrusion devices known as filament extruders create thermoplastic-based filaments used in 3D printers. Extrusion systems work by mixing raw plastic granules and additional additives, if any, in a mechanical mixer, then conveying the composite grains formed through a feed hopper to the heating nozzle side via a screw shaft [77].

In Fig. 23, a schematic diagram of the extrusion process is shown. In the extrusion process, the coated particles are fed through the hopper. Then the particles got melted at 190ºC and pressed with the screw. The melted PLA composite passed through the extrudate in the form of a filament of ~1.8 mm diameter which is suitable for 3D printing. The hot filaments were cooled down in a water tank and a pull roller was used to control the diameter of the filament.

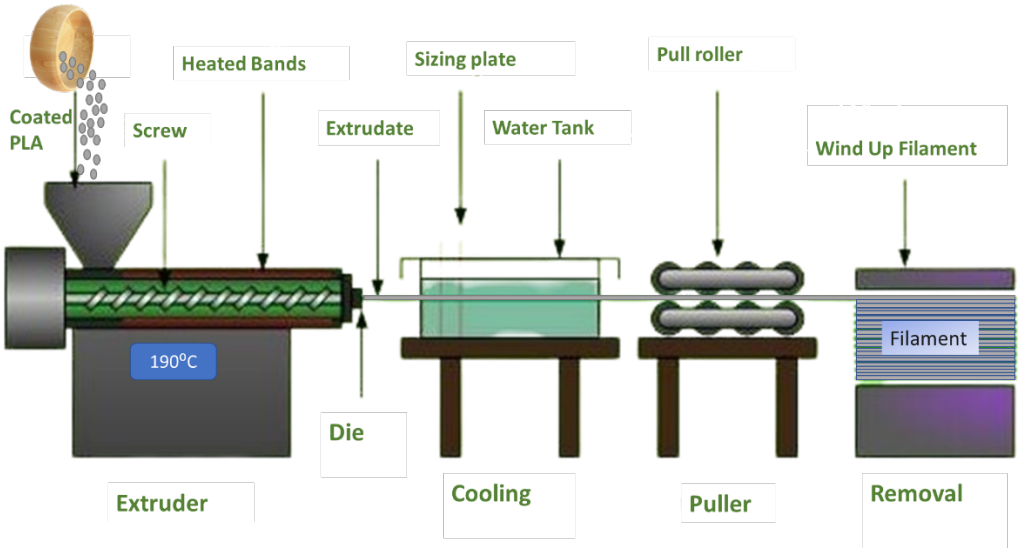

Figure 23: Schematic diagram of the extrusion process.

Figure 24: Extruder used in this work.

3D printing Process

The classic polymer extrusion process is analogous to part production in 3D printers. Modelling the part in a Computer-Aided Design (CAD) system is the initial stage of production. After that, the developed model is transformed into STL format, which allows data to be transferred between CAD platforms. Data linked to the model in STL format is communicated to the 3D printer after 2D slicing. The superposition of thermoplastic molten material termed filament, which is deposited from the nozzle of the 3D printer, produces the 3D geometry of the component designed in the computer environment [69]. In a nutshell, the technology entails pouring molten material in stages from a hot nozzle onto a heated flat table surface (Fig. 25).

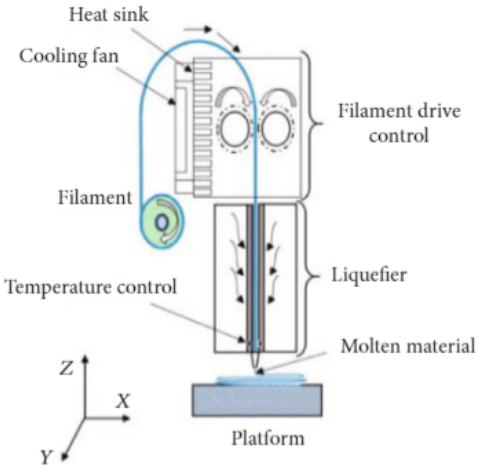

Figure 25: Production by 3D printing method [78].

Prusa i3 MK3 3D printer (Fig. 26) was used to print the sample for this project.

In table 6, all the information regarding 3D printed samples and 3D printing parameters is shown.

Table 6: 3D printing parameters

Printed samples dimensions (mm)	60x10x2
Extruder Temperature (ºC)	215
Bed	Painter's tape
Bed Temperature (ºC)	60
Cooling (Fan speed)	100%
Layer Thickness (mm)	0.1
Raster Angle (º)	-45/+45
Infill Density (%)	100%
Nozzle diameter (mm)	0.4

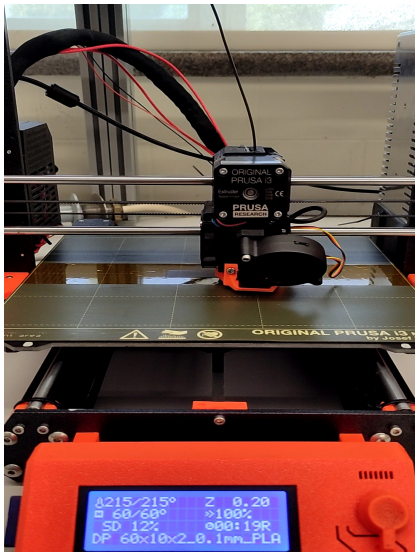

Figure 26: 3D printer (Prusa i3 MK3) used in this work.

Reinforcement %wt.-controlled 3D printing

Another process was undertaken to make the composite using Brabender Plastograph (Fig. 27). In this case, the PLA granules and the reinforcements were put together at 200 ºC inside the mixing chamber. A torque vs time graph was continuously observed during the melting and mixing process. The graph became stable and horizontal to the time axis against the torque axis after a few minutes indicating the mixture is homogenous. The process was carried out for 30 minutes for each mixture. The compositions are shown in table 7.

Table 7: The composition and reference of the samples produced in this process.

Sample name	PLA wt.%	SCF wt.%	GNP wt.%
PSG-0.5	99	0.5	0.5
PSG-1	98	1	1
PSG-2	96	2	2
PSG-5	90	5	5

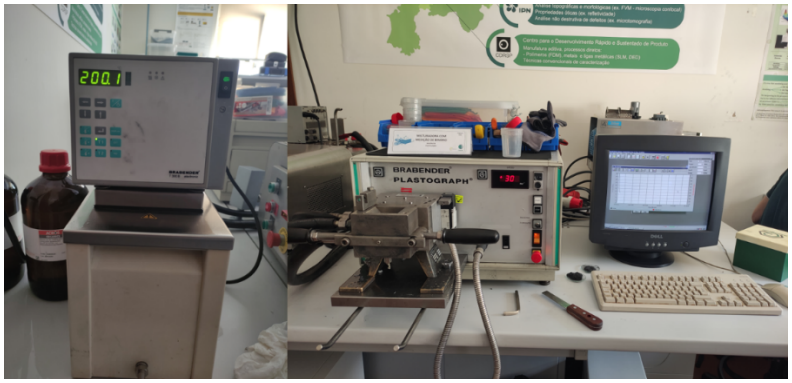

Figure 27: Plastograph used in this work.

After that, the mixtures were granulated in a granulator (Fig. 28) to make them suitable for the extrusion process to get the 3D printable filaments. After granulation, the 3D printed samples were produced in the same process described in the 5.1.3 (3D printing Process) section.

Figure 28: Granulator used in this work.

During this 3D printing process, there were a few changes in the parameters (table 8).

Table 8: 3D printing parameters.

Printed samples dimensions (mm)	60x10x2
Extruder Temperature (°C)	215
Bed	Painter's tape
Bed Temperature (°C)	60
Cooling (Fan speed)	100%
Layer Thickness (mm)	0.2
Raster Angle (º)	-45/+45
Infill Density (%)	100%
Nozzle diameter (mm)	0.8

5.1.4 Laser Texturing & Sintering Procedure

Laser Texturing

Casted PLA samples were textured with a CO_2 laser. Then the grooves created by the laser were filled with reinforcements and pressed in a hydraulic press with a 5ton load for 5 minutes. After that, the surface was sintered again with the same laser to make the final composite sample.

Table 9: Composites composition and their name for laser texturing and sintering method

Sample name	Composition
PST	PLA SCF
PGT	PLA GNP
PGST	PLA SCF GNP

For laser texturing on the casted PLA sample, the parameters used during the process are given in table 10.

Table 10: Laser texturing and laser sintering parameters.

Speed	60mm/s
Power	10%
Frequency	100kHz
Spot delay	0.1ms
Step angle	90º

Laser Sintering

During the sintering process, there were two different parameters used for different composites. For the PST sample, the less energized laser was used (Table 11) whereas for the PGT and PGST energy was higher (Table 12).

Table 11: Laser sintering parameters for PST.

Speed	3000mm/s
Power	10%
Frequency	100kHz
Spot delay	0.1ms
Step angle	90º

Table 12: Laser Sintering parameters for PGT and PGST.

Speed	120mm/s
Power	10%
Frequency	100kHz
Spot delay	0.1ms
Step angle	90º

5. 2. Characterisation techniques

5.2.1. Morphological and chemical characterisation

A concentrated electron beam is used to scan a sample's surface in a scanning electron microscope (SEM), which creates images of the sample. The sample's surface topography and chemical composition are revealed by the signals that are created because of the electrons' interactions with the sample's atoms [79]. To see the morphology of the samples, SEM (Hitachi-SU3800) technology was used before and after blending with the mechanical alloying process.

The analytical method, energy-dispersive X-ray spectroscopy (EDS) is used to characterize a sample's chemical makeup or determine its elemental composition. It depends on the interaction of an X-ray excitation source and a sample. Every element has a different atomic

structure, which allows for a different collection of peaks on its electromagnetic emission spectrum, according to the fundamental concept guiding its characterisation [80]. Moseley's law foretells the peak placements. EDS (Oxford Instruments X-MaxN) analysis was performed to identify the elemental distribution throughout the different samples using mapping for different milling times of the samples.

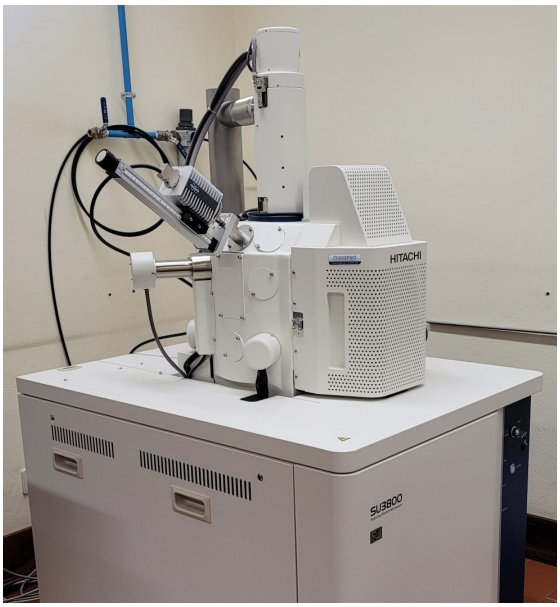

Figure 29: SEM (Hitachi-SU3800) used in this work.

5.2.2. Tomography

Like tomography and X-ray computed tomography, X-ray microtomography employs X-rays to produce cross-sections of real objects that may be utilized to construct virtual models (3D models) without harming the originals [81]. SKYSCAN X-ray microtomography was used for the tomographic analysis in this work.

Figure 30: SKYSCAN X-ray microtomography equipment used in this work.

5.2.3. 3D profilometry

Rapid, non-destructive, and non-contact surface method-optical profilometry is a form of microscope which uses a beam splitter to divide the light coming from a bulb into two separate streams. The light travels along two paths: one to the surface being tested, the other to a reference mirror. The two surfaces' combined reflections are transmitted onto an array detector. Interference can happen when the path difference between the recombined beams is on the order of a few light wavelengths or less. The surface features of the test surface are disclosed by this interference [82].

A 3D profilometer (Alicona-InfiniteFocus) was used to analyse the wear track and scar on the samples.

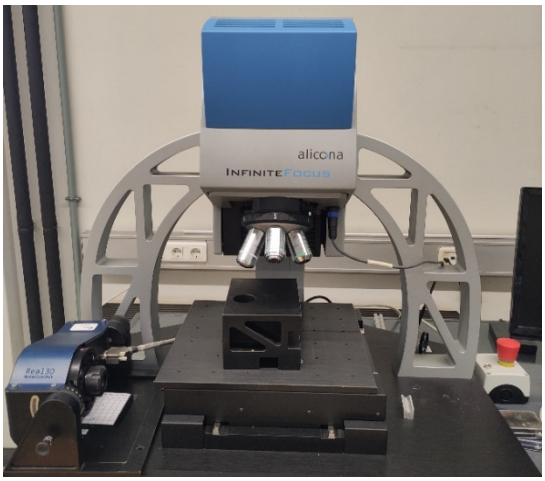

Figure 31: 3D profilometer (Alicona-InfiniteFocus) used in this work.

5.2.4. Structural characterisation

X-ray diffraction is a technique for examining the structure and physical characteristics of materials. The experimental science known as X-ray crystallography employs incident X-ray beams to diffract in various directions to determine the atomic and molecular structure of crystals. An image of the density of electrons within the crystal can be created in three dimensions by measuring the angles and intensities of these diffracted beams. The average locations of the atoms in the crystal can be calculated from this electron density [83]. The crystalline structure of the particles and composites was investigated by XRD (Philips XPert) with Co-Ka radiation (1.790300 Å).

Figure 32: Philips XPert XRD equipment used in this work.

5.3.5. Thermal analysis characterisation

Differential scanning calorimetry (DSC) is a thermal analytical technique that measures the difference in heat required to raise the temperature of a sample and a reference as a function of temperature. DSC is widely utilized to investigate polymeric materials and determine their thermal transformation. The glass transition temperature (Tg), crystallization temperature (Tc), and melting temperature (Tm) are all important thermal transitions [84]. Differential Scanning Calorimetry was used to assess the change in thermophysical behaviour and crystallinity of the PLA matrix. For all the samples, the temperature range was 25 ºC to 230 ºC. The heating rate was 10 ºC /min and the atmosphere was N_2, 40 ml/min.

The degree of crystallinity of the composite powders after compaction was evaluated using the equation [85]:

$$X_c\,(\%) = \frac{\Delta Hf}{\Delta Hfo} x100 \qquad (1)$$

Where ΔH_f represents the melting enthalpy of the samples and $\Delta H_f{}^o$ is the standard enthalpy of PLA normally taken as 93J/g [85].

NETZSCH-DSC 204 f1 phoenix equipment was used for the tests.

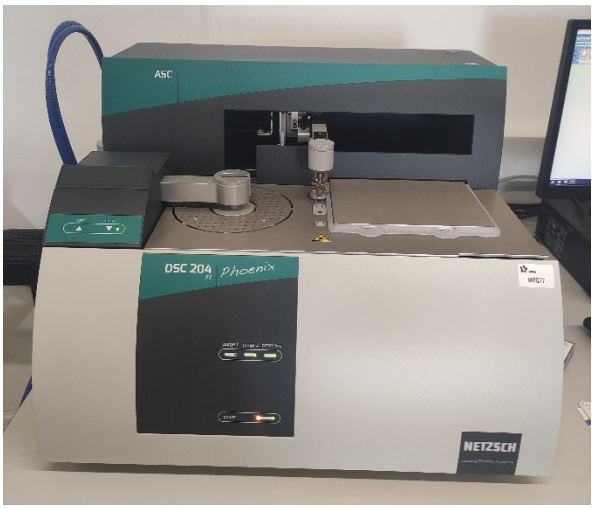

Figure 33: DSC equipment (NETZSCH-DSC 204 f1 phoenix) used in this work.

5.3.6. Mechanical and tribological characterisation

The Shore durometer is a tool used to gauge a material's hardness; commonly, it is used with rubbers, elastomers, and polymers. Greater resistance to indentation and consequently tougher materials are indicated by higher numbers on the scale. Lower numbers denote softer materials and less resistance. There are various durometer scales available for materials with various qualities. The ASTM D2240 type A and type D scales, which employ somewhat different measurement systems, are the two most popular scales. Softer ones are rated on the A scale, while harder ones are rated on the D scale [86].

The samples' Shore D hardness was determined using a CV Instruments Limited with the serial number 6870 under the ASTM D2240-00 testing standard. The Load was applied manually, and the results were taken in 3s. 5 tests were done on each sample.

Figure 34: Shore (Durometer) Hardness Tester used in this work.

3-Point Bending test

The three-point bending flexural test yields information on the material's bending modulus of elasticity, flexural stress, flexural strain, and flexural stress-strain response. This test is carried out using a three-point bend fixture on a universal testing machine. For 3D printed samples, a Shimadzu AG-10 universal testing machine equipped with h 5kN load cell at room temperature and with a grip speed of 2 mm/min was used for the 3-point bending tests of 5 samples from each type of composites. The specimens with dimensions of 60x10x2 mm were tested based on ASTM Standard D 790.

The stress-strain curve is obtained using from the load-displacement curve using equations 2 and 3 [87].

$$\sigma_f = \frac{3PL}{2bd^2} \tag{2}$$

$$\epsilon_f = \frac{6Dd}{L^2} \tag{3}$$

Here, σ_f and ϵ_f are Flexural stress and flexural strain respectively. P is applied load, and D is displacement. L, b, and d are the length, width, and thickness of the samples respectively.

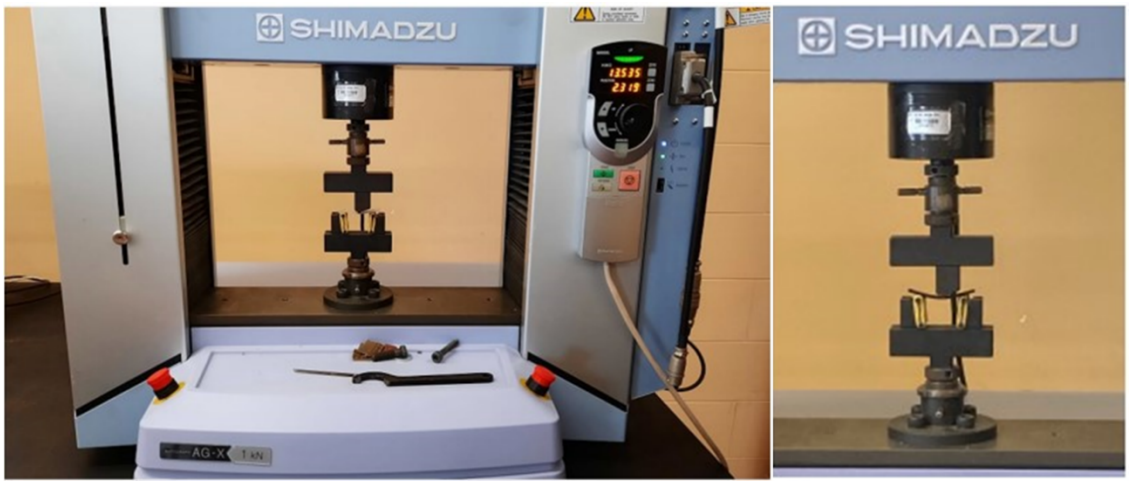

Figure 35: 3-Point bending test equipment (Shimadzu AG-10 universal testing machine).

Ball on disk tests (Reciprocating)

Before starting the wear characterisation, the casted samples were polished with 2400 mesh grit paper followed by 4000 mesh grit paper. Then the samples were tested in the Rtec instrument -MFT 5000. For 3D printed samples, there was no polishing involved. 3 tests were performed on each sample using this process.

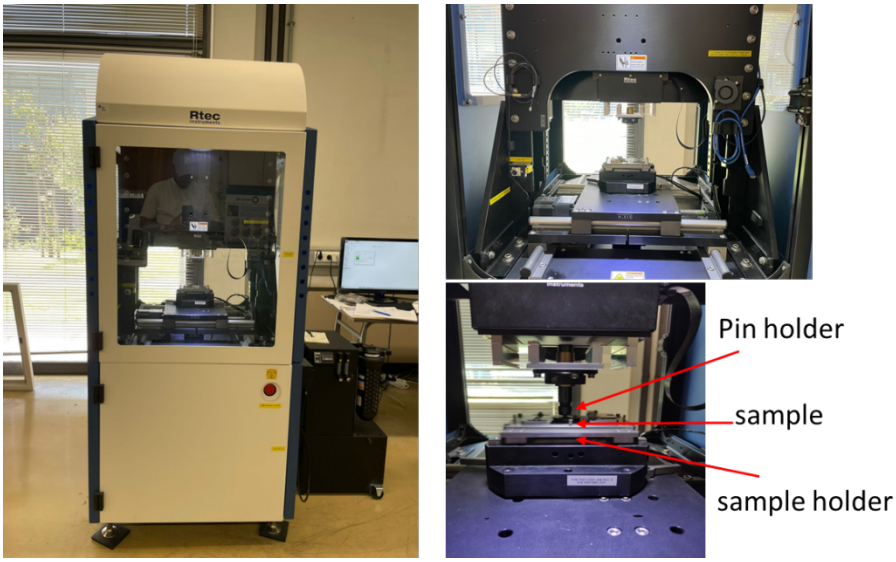

Figure 36: Pin on disk tribometer (Rtec).

A load of 5N was applied through a spherical pin based on a SS (100 Cr^6) ball with a diameter of 5 mm. Before starting, the ball was ultrasonically cleaned in ethanol and dried into the pin holder.

It was a reciprocating test. The stroke length was set at 6 mm, the frequency was 8.5 Hz, and the total time duration was 300 s. The experiment was carried out at room temperature (25°C temperature, 50 % humidity).

A 3D profilometer (Alicona) was used to analyse the wear track and scar on the samples. The specific wear rate, k, was calculated using the equation [88]:

$$k = \frac{V}{N}\left(\frac{nm^3}{nm}\right) \quad (4)$$

Where V denotes the wear volume on the sample, N is the load applied, and S is the journey distance.

5.3. Raw materials

The elemental Sn (purity 99.9%), Zn (purity 98.8%), and Bi (purity 99.5%) powders from Goodfellow were used for the brazing alloy design, with average particle sizes of 45, 7.5, and 45 µm, respectively. A mixture of short carbon fibres and Graphene nanoplatelets were used as reinforcements within the Sn-based brazing alloy. Sigrafil provided the SCF, which had a filament length of 80µ and diameter of 7µ while Nanografi provided the GNP (purity 99.9%), which had an average thickness of 5 nm and dimensions of 30 µm. The density of SCF and GNP were 1.8gm/cm^3 and 2 gm/cm^3 respectively.

In Fig. 37, the raw PLA particles are shown to have an average diameter of 4.85 mm.

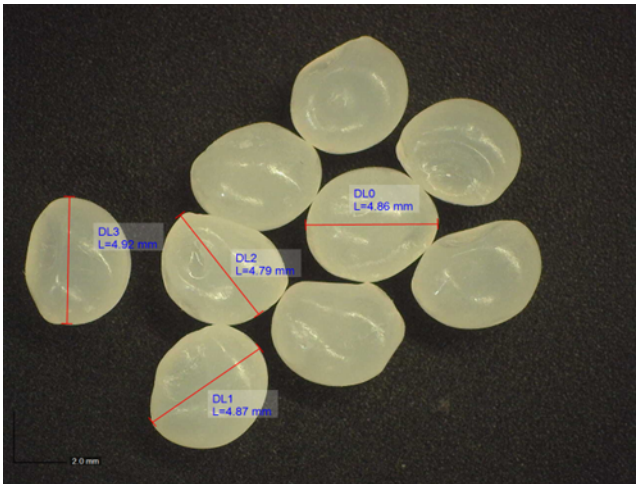

Figure 37: Raw PLA.

Morphology

Figure 38 shows the SEM images that correlate to the individual raw powders. GNP powders have a flake-like morphology with stacked layers of graphite sheets, whereas SCF appears as a random distribution of cylindrical rods. Sn powder has a droplet-shaped spheroidal morphology, with a size distribution of big and tiny particles that varies. Bi powder has a completely spherical shape and particles of equal size. Zn powders have a spherical shape with a varied size distribution that includes small, medium, and large particles.

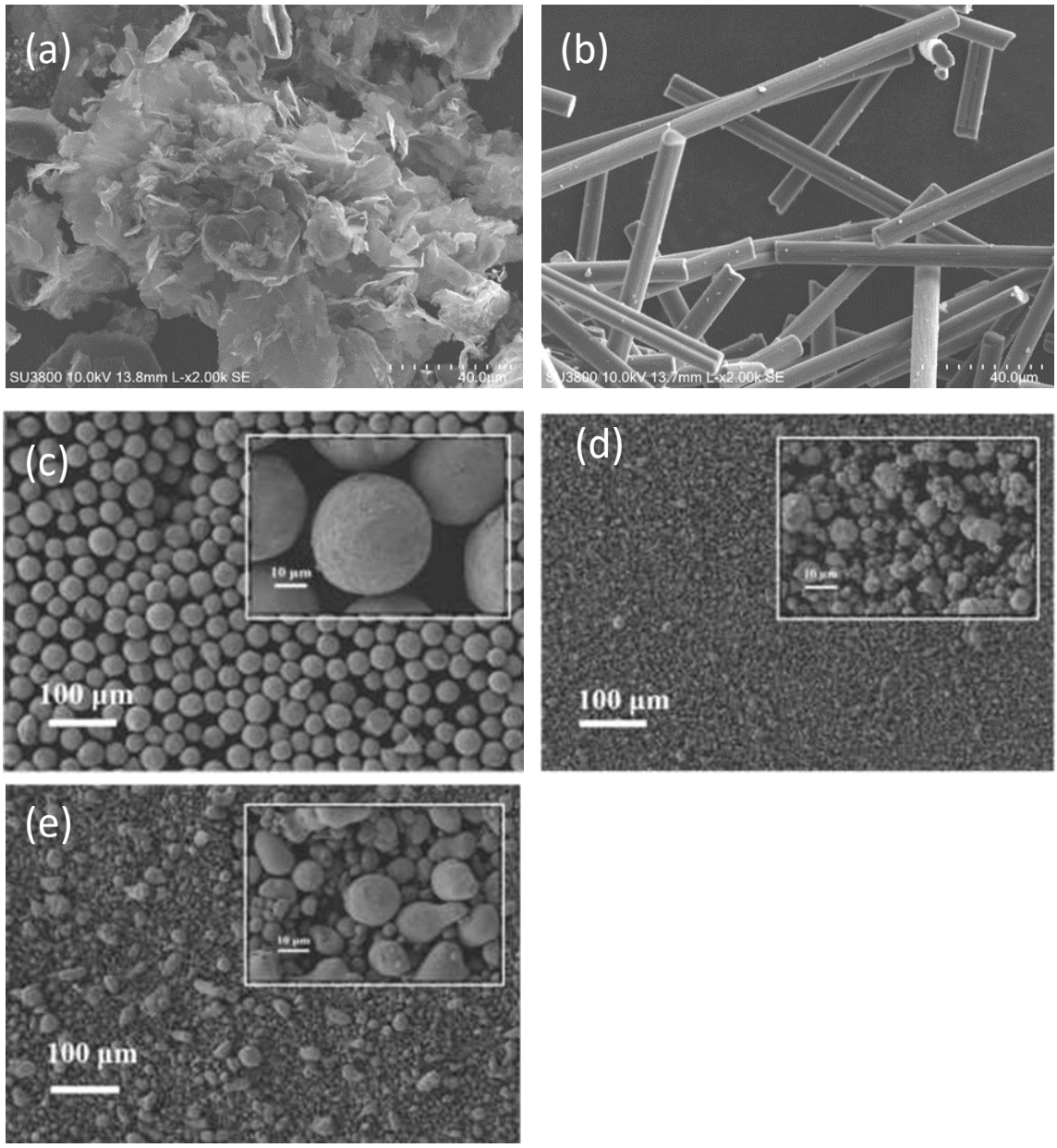

Figure 38: SEM images corresponding to the initial morphology of raw powders: (a) GNP, (b) SCF, (c) Bi, (d) Zn, (e) Sn

Structural evaluation

The crystallographic structure of the raw PLA powders characterized by XRD is illustrated in Fig. 39. Two dominant diffraction peaks at 2θ=19° and 22° represent the (200/100) and (203) planes, respectively, and the weak diffraction peak at 25.5° is indicative of the (015) plane. [89].

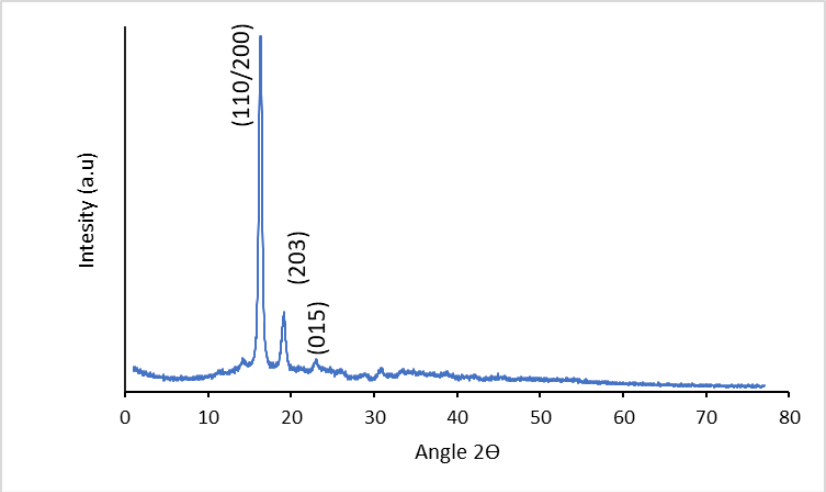

Figure 39: XRD pattern of raw PLA.

The crystallographic structure of the raw Sn-Zn-Bi mixture powders characterized by XRD is illustrated in Fig. 40. Sn peaks are visible at 35.7º,37.4º, 51.4º, and 52.6º angles. The small Bi peak is noticeable at a 42.4º angle whereas the two Zn peaks are at 45.7º and 50 angles. These peaks are expected to be seen in the XRD of Sn-Zn-Bi alloy produced by MA.

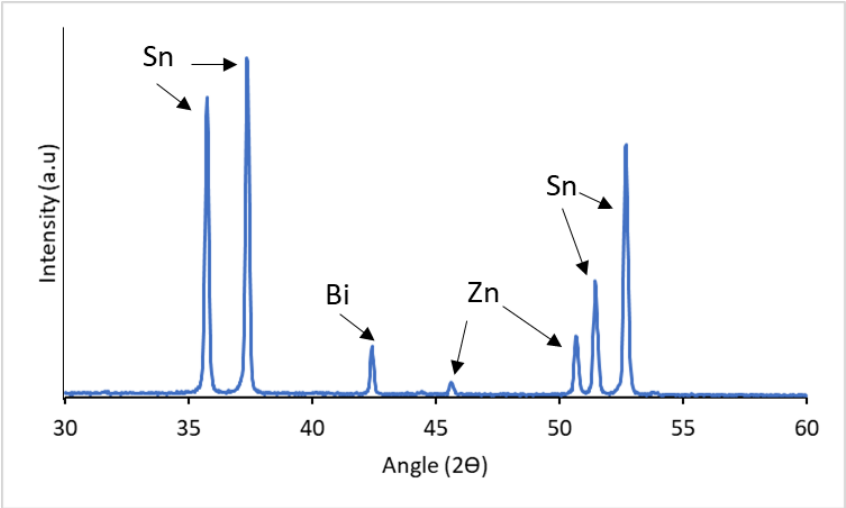

Figure 40: XRD pattern of raw Sn-Zn-Bi mixture.

The diffraction pattern of the GNP has one characteristic peak at ~31°, corresponding to the 002 planes. Diffraction peaks at 2Θ ~ 31.9° can be identified as the amorphous structure of SCF illustrated in Fig. 41.

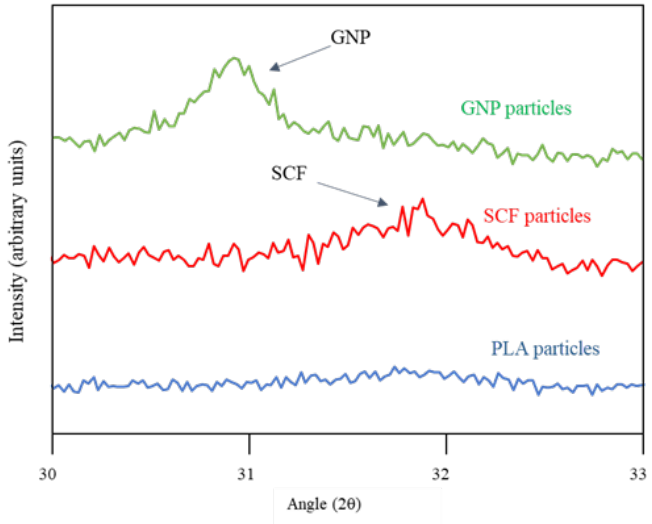

Figure 41: XRD pattern of PLA, GNP, and SCF.

DSC measurement

DSC of PLA is shown in Fig. 42. PLA exhibited a glass temperate (T_g) peak at around 6 °C, and a melting temperature (T_m) peak at around 173 °C. The crystallinity (X_c) is measured using equation 1 and the value is 45%.

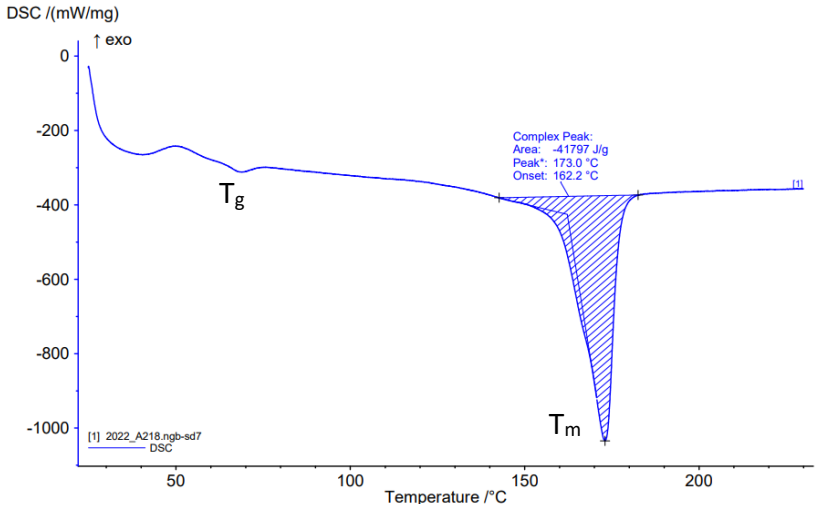

Figure 42: DSC of PLA particle.

The PLA used for 3D printing was a little different. The DSC analysis (Fig. 43) shows a small cold crystallization peak at 160°C which was not present in the raw PLA used for casted samples. T_g is 68.6 °C and T_m is 178.4 °C which is a little higher than the PLA used for casted samples (Fig. 42). The crystallinity (X_c) of this PLA is 38.825%.

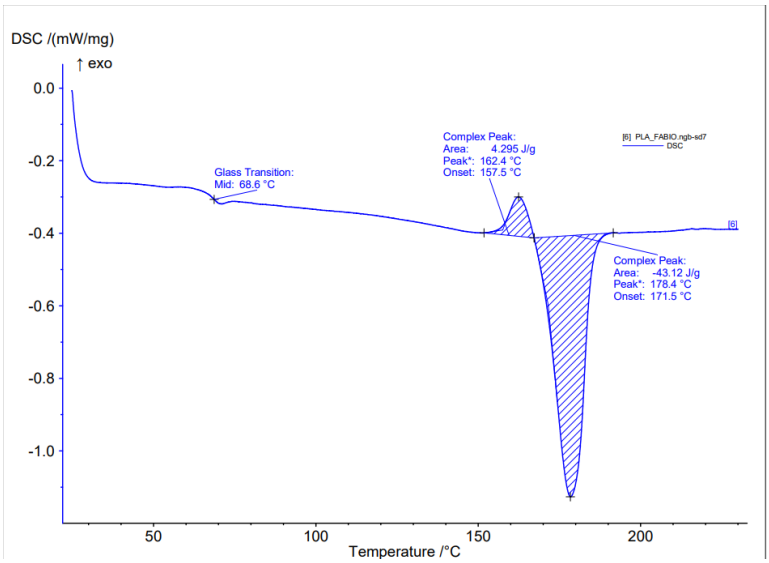

Figure 43: DSC of PLA used for 3D printing.

6. RESULTS AND DISCUSSION

As mentioned in section 4, 3 different sets of manufacturing processes were used in this project to produce different reinforced PLA composites (Fig. 44): (1) mechanical alloying and casting, (2) mechanical alloying / plastography, filament extrusion, and 3D printing, and (3) laser texturing reinforcement of the texture by cold compaction, and laser sintering. The results will be presented separately, for each manufacturing process.

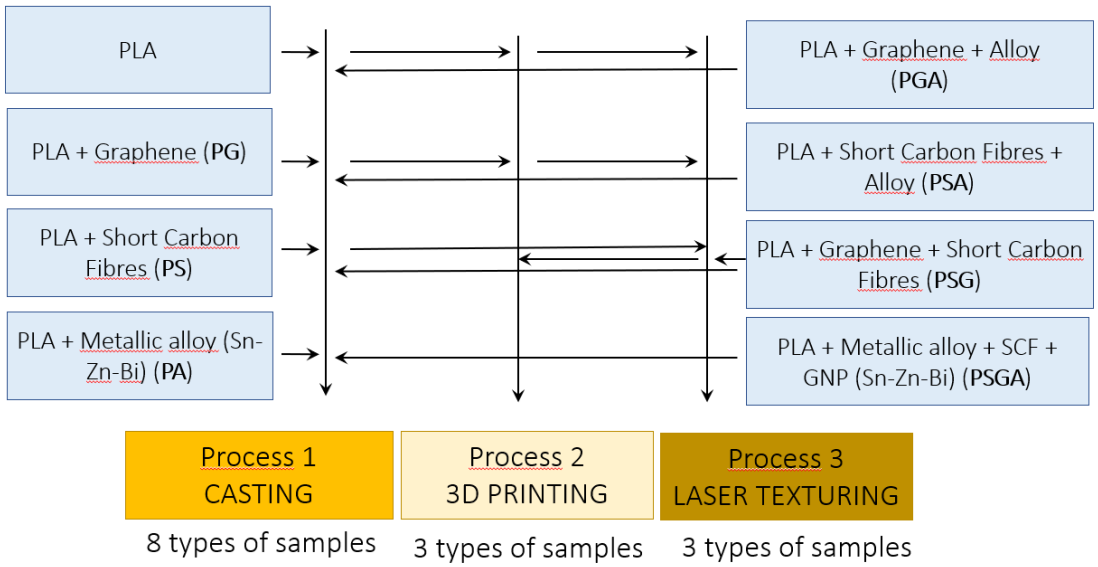

Figure 44: Diagram of all the raw materials and techniques used in this work.

Mechanical alloying and casting

A flow diagram of the complete Mechanical alloying and casting process for sample production is given in Fig. 45. It is a two-step process. The first step is mechanical alloying of alloy, and the second step is mechanical alloying of PLA with all reinforcements followed by casting.

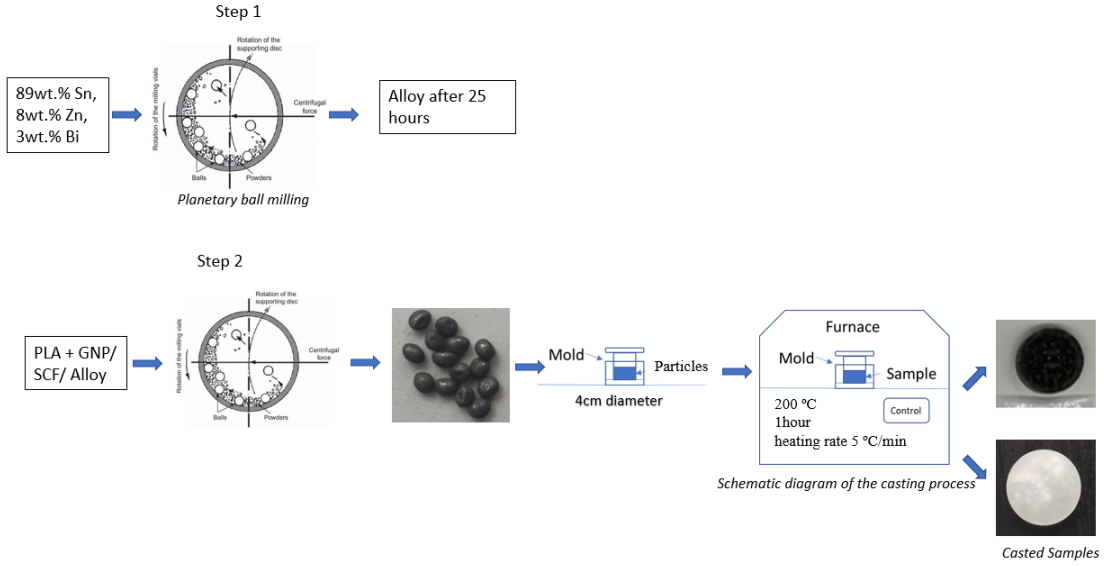

Figure 45: Flow diagram of mechanical alloying and casting.

6.1. Mechanical alloying and casting Process

Before casting, mechanical alloying was used for the synthesis of the composite materials (Table 13).

Table 13: Samples composition produced in this process and their corresponding reference.

Samples	Short Name	Samples	Short Name
PLA	PLA	PLA-Alloy	PA
PLA-SCF	PS	PLA-SCG-Alloy	PSA
PLA-GNP	PG	PLA-GNP-Alloy	PGA
PLA-SCF-GNP	PSG	PLA-SCF-GNP-Alloy	PSGA

6.1.1. Mechanical alloying

Mechanical alloying of the metallic powders

Morphological and structural characterisation

The SEM images and the corresponding EDS elemental mapping of the metallic alloy blends after 5, 10, and 25h of MA are presented in Figs. 46, 47, and 48, respectively.

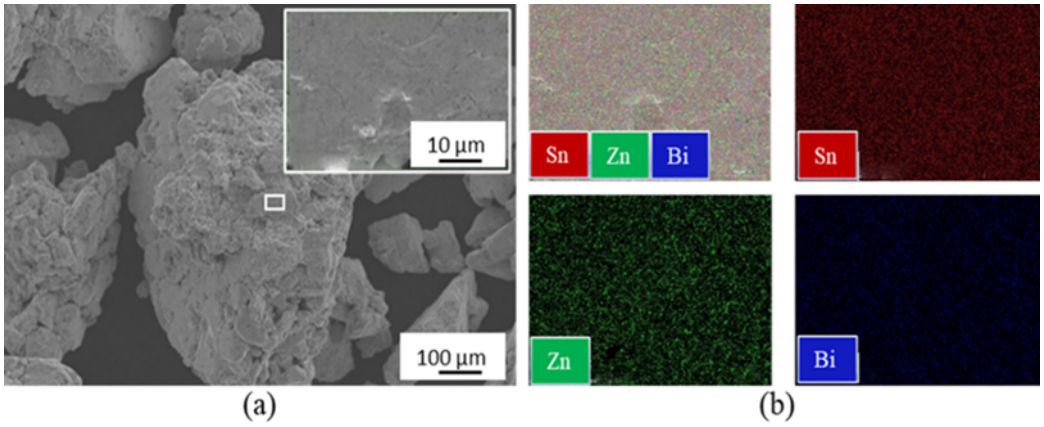

Figure 46: (a) SEM images and (b) EDS elemental maps of Sn-Zn-Bi mixture after 5 hours of MA.

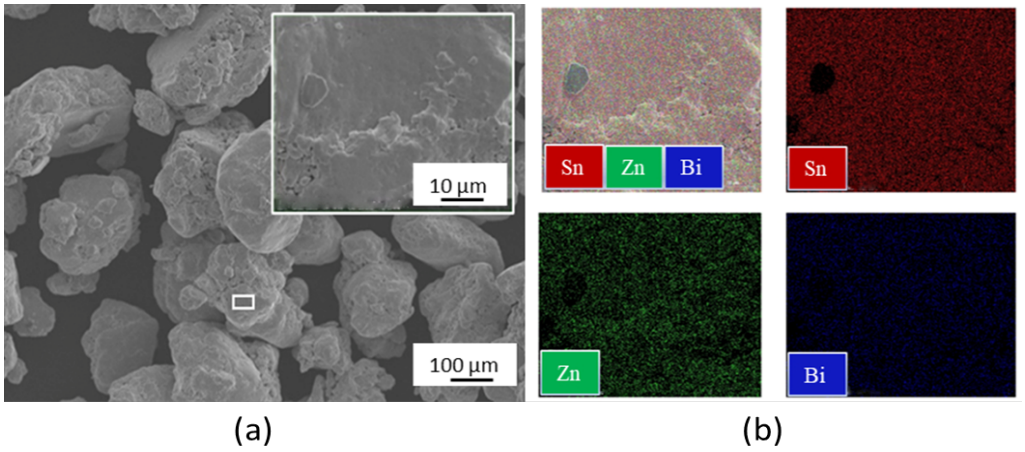

Figure 47: (a) SEM images and (b) EDS elemental maps of Sn-Zn-Bi mixture after 10 hours of MA.

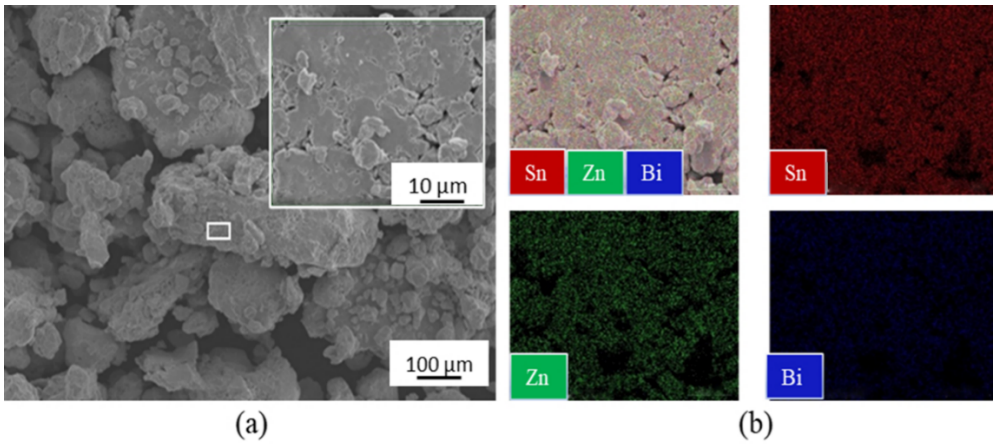

Figure 48: (a) SEM images and (b) EDS elemental maps of Sn-Zn-Bi mixture after 25 hours of MA.

During the first 5h of MA, there is a change in the shape of the particles, which become more flattened (Fig. 46). This phenomenon is well described in the literature on MA of ductile materials [90]. After 10 h of MA (Fig. 47), the average particle size of the sample is lower than the one for 5 h of MA. This means a fracture process occurred from 5h of MA likely due to the work-hardened, by plastic deformation, of the particles [91]. After 25h of MA (Fig. 48), particles with a size lower than 10 mm are detected. From the EDS elemental maps, it can be observed that the mixing of Sn, Zn, and Bi is quite homogeneous after 25h of milling (Fig. 48). Figure 49 shows the EDS elemental analysis after 25h of milling. Well-defined peaks of tin are present, together with the Zn and Bi ones with lower intensity (lower concentration in the mixture).

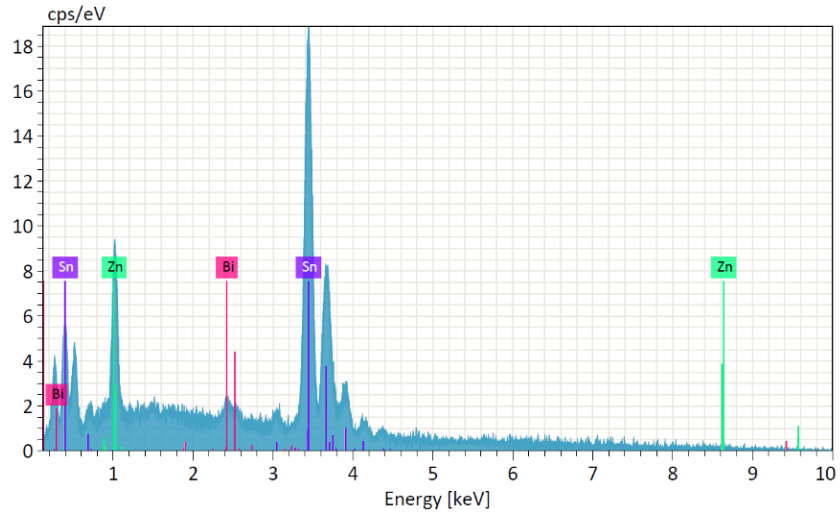

Figure 49: EDS elemental analysis of Sn-Zn-Bi alloy after 25 hours of MA.

Evolution of the crystal structure

The evolution of the XRD patterns of the Sn-Zn-Bi mixture as a function of MA time is presented in Fig. 49. After 5 h of MA, diffraction peaks of the constituent metals, i.e., Sn, Zn, and Bi are still detectable. When MA time is increased to 10 h, the diffraction peaks of Zn are no longer visible, which indicates that the dissolution of the atoms of Bi into the Sn lattice occurred. After 25 hours of MA, only Sn diffraction peaks are visible, which means that the Zn and Bi were incorporated in the Sn lattice. However, no noticeable shift of the Sn diffraction peaks is observed since the atomic radii of these elements are quite similar (1.45, 1.42, and 1.43 Å for Sn, Zn, and Bi, respectively). These results are in accordance with previous work on this system [92] that showed that it is possible to incorporate Zn and Bi into the tin lattice after a certain period of MA.

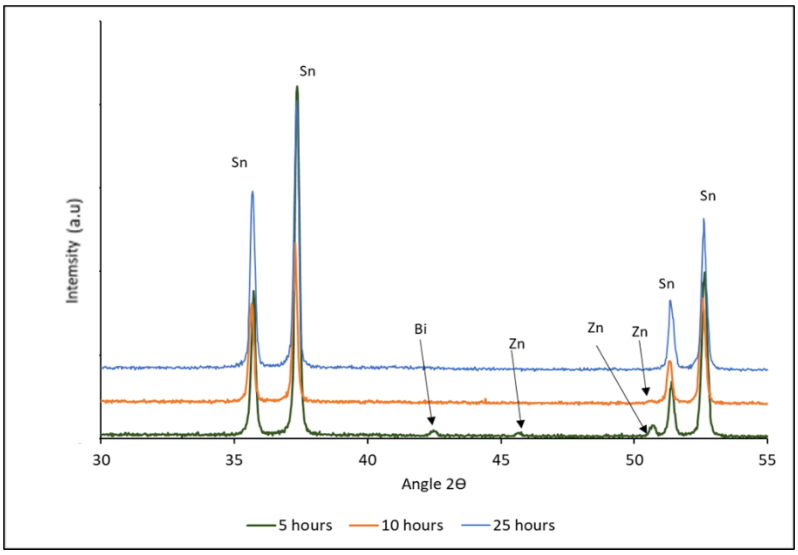

Figure 50: XRD patterns of the Sn-Zn-Bi mixture milled for 5, 10, and 25h.

Mechanical alloying of the metallic alloy- and carbon-reinforced PLA

Morphological and structural characterisation

Figure 51 shows an optical image of the PLA granules coated with GNP and metallic alloy, as a typical example of all the other coated systems. In all the cases, the PLA granules seem to be entirely coated, presenting a dark grey colour.

Figure 51: PLA granules coated with GNP and metallic alloy, as a typical example of the other coated systems.

SEM/EDS analysis (Fig. 52) was performed to confirm the optical observations.

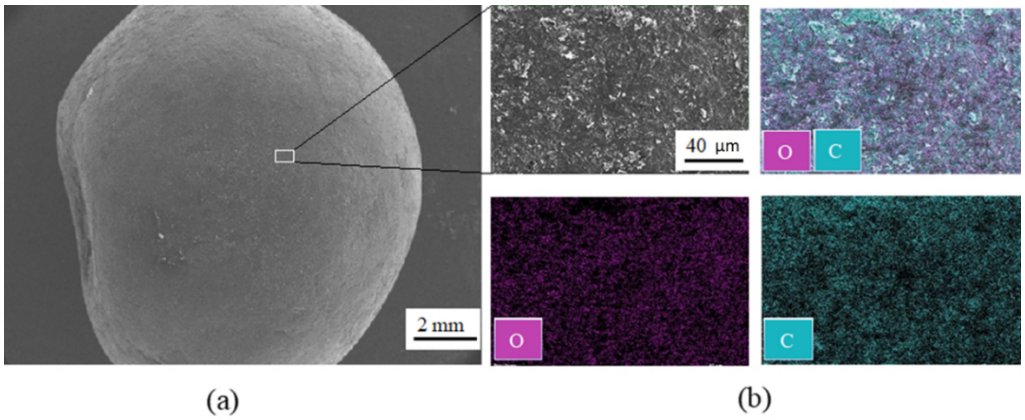

Figure 52: (a) SEM images and (b) EDS elemental maps PLA granules coated with GNP and SCF, as a typical example of all the other systems.

The SEM images (Fig. 52a) show that the PLA granules were completely covered by the different reinforcements. The EDS maps (Fig. 52b) confirm that the distribution of the different metallic elements on the PLA surface is quite homogenous.

6.1.2. Casting

Figure 53 shows pictures of PLA and reinforced PLA casted samples. All but PLA present the same grey tone as the MA'ed coated granules.

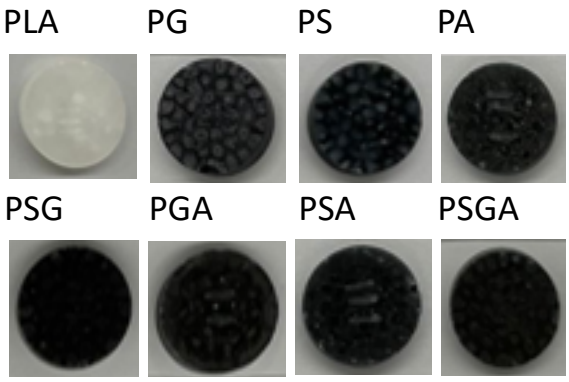

Figure 53: Different casted samples produced in this work.

Morphological and structural characterisation

The XRD patterns of the raw PLA (granules) and casted PLA samples are illustrated in Fig. 54. They exhibit the same diffraction peaks at the same angles, meaning that casting did not induce any new structural phase. However, the diffraction peaks are slightly broader, meaning a decrease in the PLA structural order. It is likely that a partial amorphization of PLA occurred during casting since the background of the corresponding XRD pattern can't be fitted by a horizontal line.

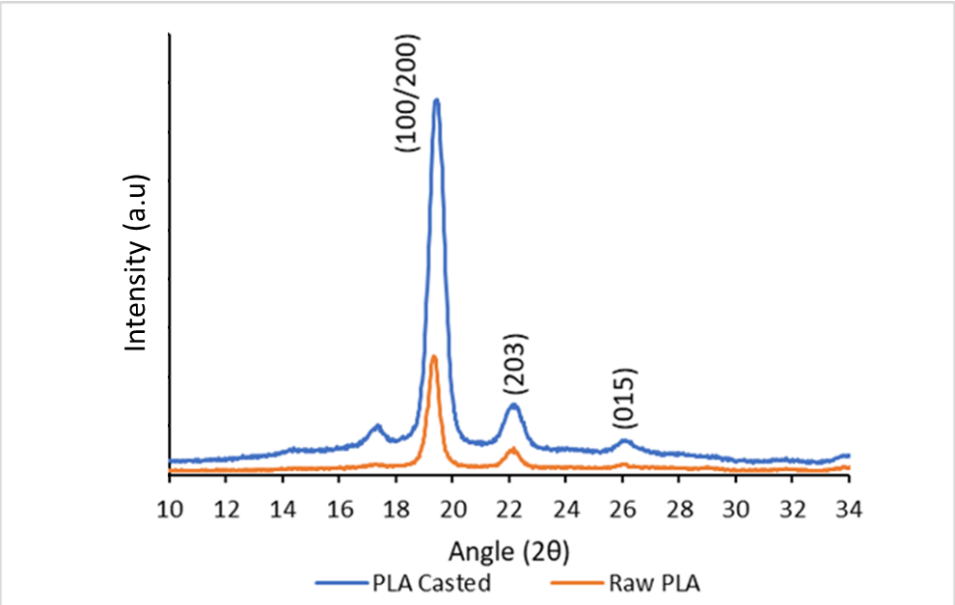

Figure 54: XRD patterns of the raw and casted PLA.

Thermal analysis

The DSC analysis of the casted sample (Fig. 55) corroborates the XRD analysis, confirming that casting induced some amorphization of the PLA. Contrary to raw PLA, a cold crystallization peak at ~110 ºC was detected for the casted sample. This cold-crystallization process is defined as a polymer crystallization that occurs above the glass transition temperature (Tg) upon heating in the presence of nuclei formed during the previous cooling step or during the sample's permanence at temperatures below Tg. So, during DSC, the PLA polymer got heated again and got sufficient energy for mobility above Tg temperature to arrange itself into the ordered structure (i.e., crystalline structure) by chain folding. Crystallinity (X_c) of the casted sample was calculated and the value of 40 % was obtained. This value is slightly lower than the one calculated after the DSC analysis of the raw material (45%) due to the loss of crystallinity during the casting process [93].

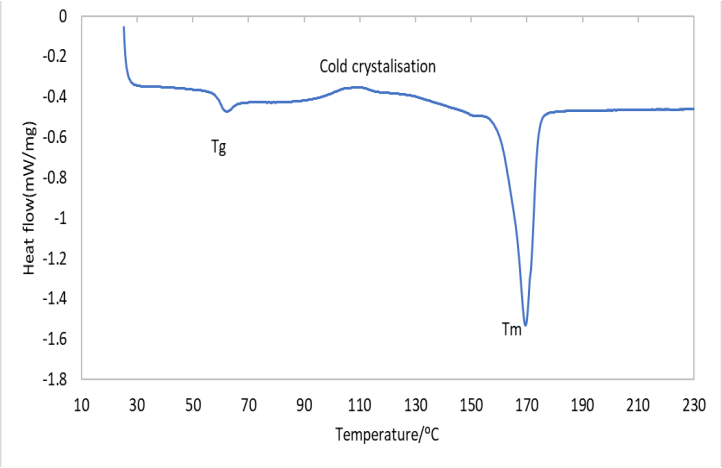

Figure 55: DSC of casted PLA.

Structural evaluation of the reinforced PLA composites

The XRD patterns of the casted PLA and reinforced PLA with GNP and SCF samples (PLA, PG, and PS) are shown in Fig. 56. The characteristic diffraction peak of GNP is clearly noticeable at a 2Θ angle of 33º. The diffraction peak of SCF is hardly distinguishable once it is positioned at the same diffraction angle as one of the PLA diffraction planes.

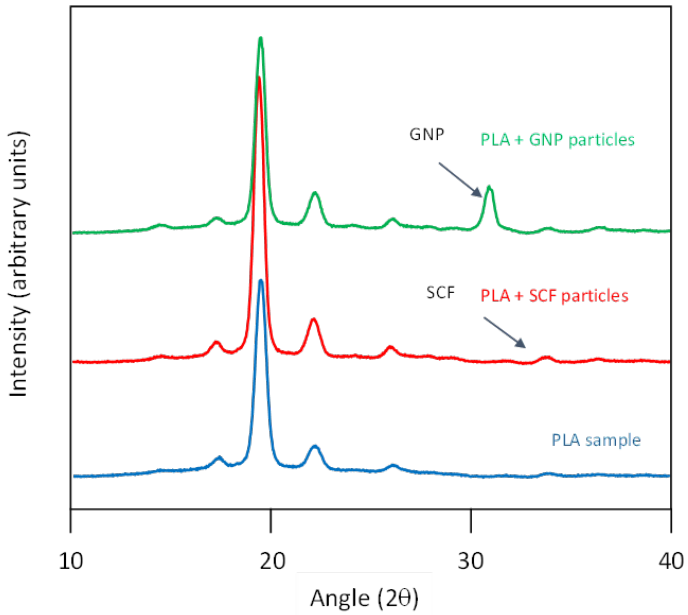

Figure 56: XRD patterns of the PLA, PS, and PG casted samples.

Figure 57 represents the XRD patterns of the PLA and PLA reinforced Sn-Zn-Bi samples. Considering the position of the Sn diffraction peaks (main element in the Sn-Zn-Bi alloy), the XRD analysis of the reinforced PLA sample was performed just for 2Θ between 35 and 40º. The results show the characteristic diffraction peaks of Sn, proving the existence of the alloy in the reinforced PLA casted sample.

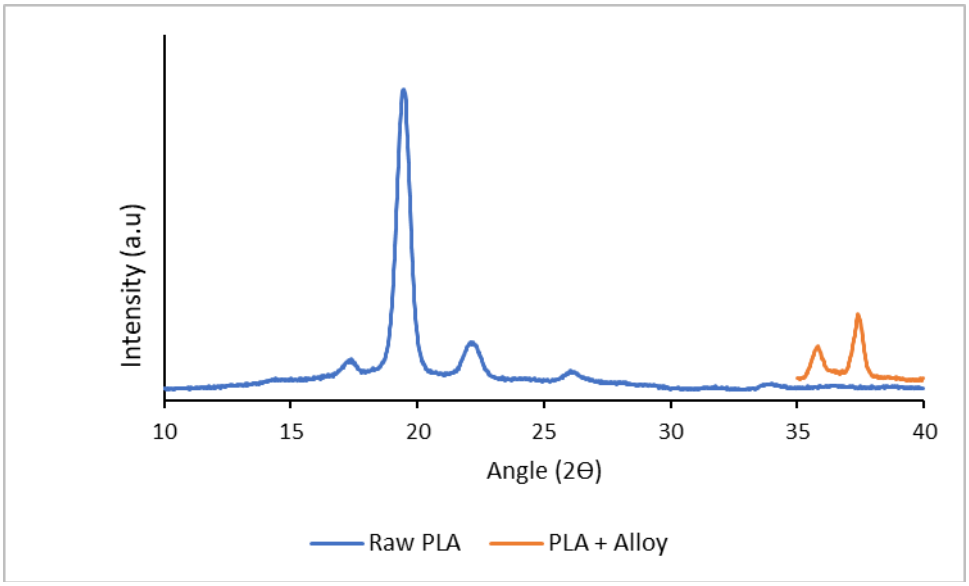

Figure 57: XRD of PLA and PLA reinforced with the metallic alloy casted samples.

Mechanical and tribological characterisation

Shore D Hardness tests

The Shore D hardness of the different casted samples is presented in Fig. 58. All the composites have higher hardness values than pure PLA (77 Shore D). PSG has the highest value among all the samples (84.5, corresponding to a 10% increase in hardness compared to PLA). PS and PG have a similar shore D value of 83. PSA, PSGA, and PGA also have almost similar shore D hardness (80, 81, and 81 respectively). The samples partially or totally reinforced with the metallic alloy have lower hardness values compared to SCF and GNP reinforced PLA samples. All the hardness values have a standard deviation of ~1 to 2 shore D. Addition of SCF and GNP increases the hardness of the composite as they are much harder than the polymer matrix. Similar results were obtained in other works where hardness was reported to be increased by the addition of GNP into polymer-based composites [94-97]. In some other studies, the increase of hardness of polymers by incorporating SCF was also observed by many authors [98,99].

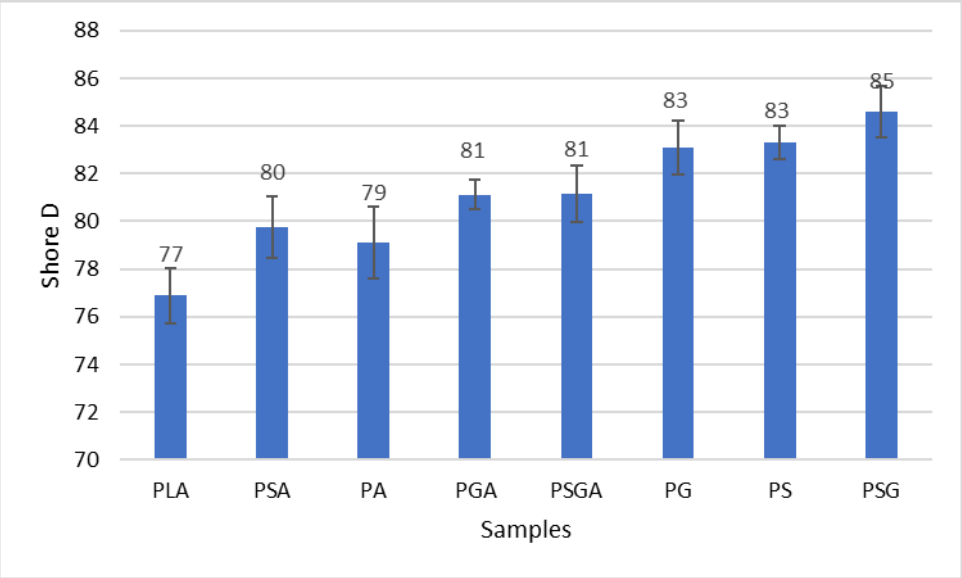

Figure 58: Shore D hardness of the casted samples.

Tribological analysis

Figure 59 illustrates the COF vs time (maximum of 300 s) curves for all the casted samples. All the reinforcements did not induce a significant reduction in the COF values. The average COF value of PLA is around 0.50. PG sample has the lowest value of COF (0.43) corresponding to a 14% reduction followed by PSG (0.44) which is a 12% reduction of COF compared to PLA (Fig. 60). The reason behind this may be the effect of graphene as a solid lubricant [100]. PGA, PSA, and PS have a similar average COF value (0.48). PA sample has the highest value of COF, which fluctuates during the tribological test from 0.53 to 0.6 with an average value of 0.55 which is a 10% increase in COF compared to PLA. The PA sample had cracks on the surface and chipping of material happened during the test due to the improper incorporation of alloy into the polymer which might be the reason for this increase in COF. PSGA shows the same average COF (0.50) as PLA. Batakliev [101] observed a similar COF reduction in PLA composites reinforced with GNP and carbon nanotube. The usual load applied during the wear test may cause the carbon flakes to separate from the nanocomposite matrix and provides a transfer film that acts as solid lubricants resulting in noticeably lower coefficients of friction than pure PLA [102].

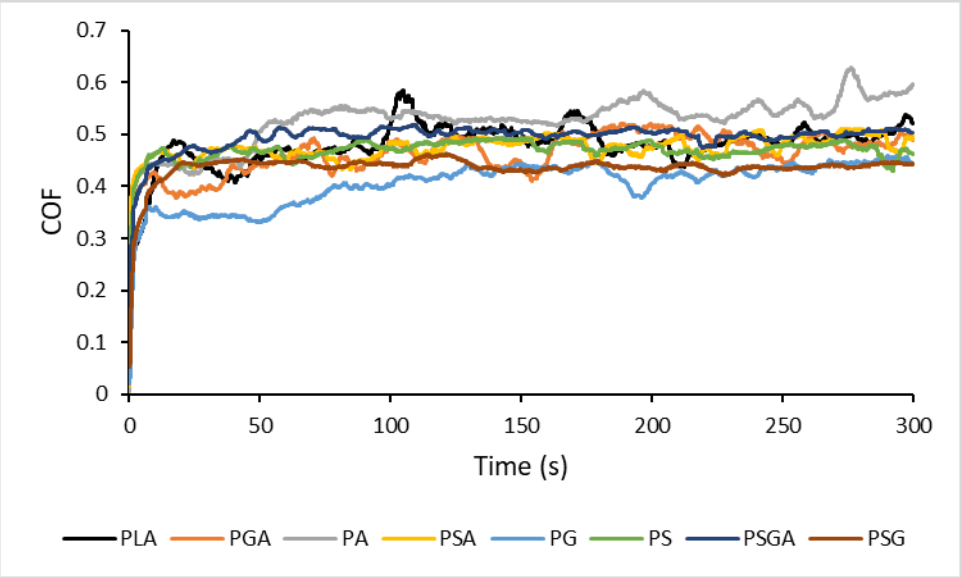

Figure 59: Time vs COF curves of the casted samples.

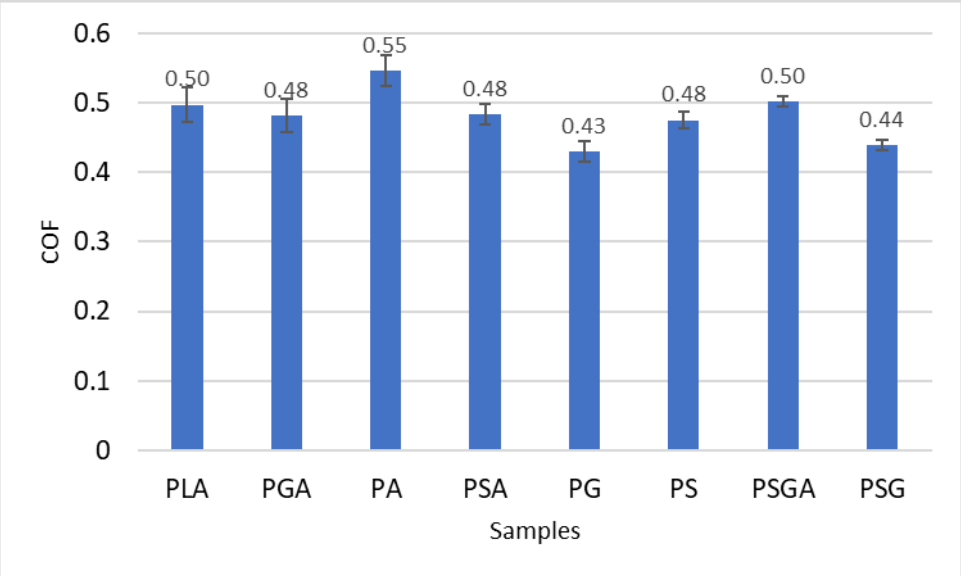

Figure 60: Average COF values of the casted samples

Figure 61 represents the 3D profilometry images of the wear scars and the corresponding wear profiles obtained from the casted samples after the tribological tests. The wear profile of the PSG sample has the lowest maximum wear depth (~6 µm), almost 7 times lower than the PLA sample (~40 µm). The PA sample has the highest maximum wear depth of ~110 µm. In this sample, some chipping happened during the tribological tests meaning that the metallic alloy was not properly incorporated into the PLA matrix and the adhesion was not good enough between PLA and the alloy to sustain the load applied during the test which created a deep wear profile on the sliding area noticeable in the 3D scan (in the colour contour of the 3D scan, green to blue represents the lower to a higher depth of the wear profile). PG has the second-

lowest maximum wear depth of ~11 µm. PSA and PGA have almost the same maximum wear depth (~50 µm). PS and PSGA have ~35 and ~22 µm of maximum wear depth respectively.

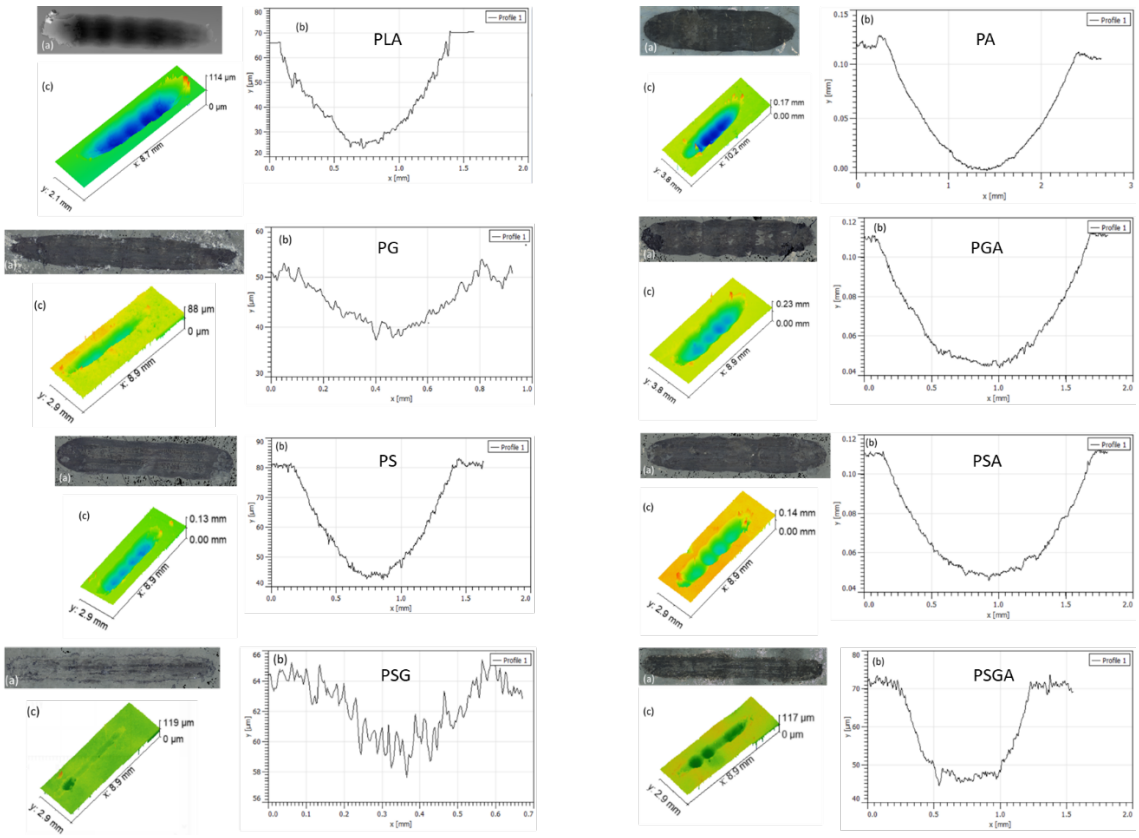

Figure 61: Images of the wear profiles and 3D scans of the casted samples.

The wear rate of the casted samples is illustrated in Fig. 62. Increased hardness values helped to increase wear resistance for the composite samples with GNP and SCF [103]. Pure PLA has an average specific wear rate of 1.8e-3 mm^3/Nm. PSG sample has the lowest amount wear rate (1.5e-04 mm^3/Nm) corresponding to a 12 times reduction compared to pure PLA. PG sample also shows a reduced wear rate (2.4e-04 mm^3/N). Like the COF, the highest wear rate was found for the PA sample (3.5e-03 mm^3/Nm) which is almost 2 times higher than PLA. During reciprocating pin on disk test, chipping of material occurred. The reason for this is the lower adhesion between the alloy and the polymer achieved by casting. PSGA also shows significant wear resistance (6.5e-4 mm3/Nm) but is higher than PSG and PG. PSA (1.9e-3 mm3/Nm) and PGA (2e-3 mm3/Nm) show higher wear rates than pure PLA. An increase in wear resistance by integration of GNP into the PLA matrix was reported by Ustillos *et al* [103]. Friedrich [104] showed in his study that SCF can affectively increase wear resistance in polymers. SCF and GNP both are much harder than the PLA and they can increase the hardness

in the composite which helps to have higher wear resistance. SCF increases the contact area of higher load-bearing capacity resulting in higher wear resistance for these composites.

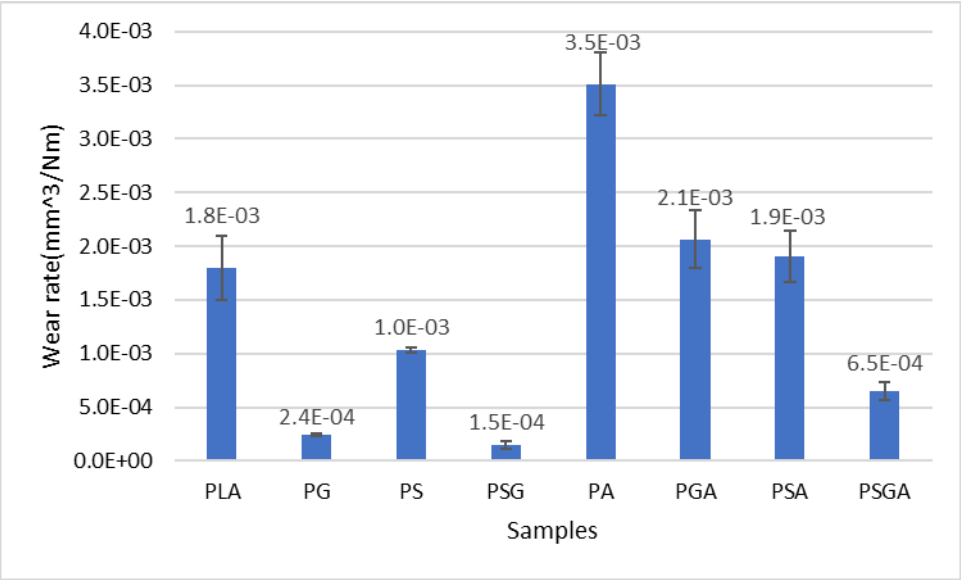

Figure 62: Specific Wear rate of the casted samples.

Mechanical alloying, filament extrusion, and 3D Printing

From the above-mentioned results, it was obvious that casted samples reinforced with the metallic alloy did not perform well mechanically and tribologically. So, it was decided just to 3D print PLA with SCF and GNP reinforcements. Mechanical alloying was used to produce different composite materials. Then, they were extruded to produce the filaments. Finally, 3D printing was used to fabricate three different samples of PLA, PLA+GNP, and PLA+GNP+SCF (Table 14) (Fig. 63).

Table 4: All 3D printed composites

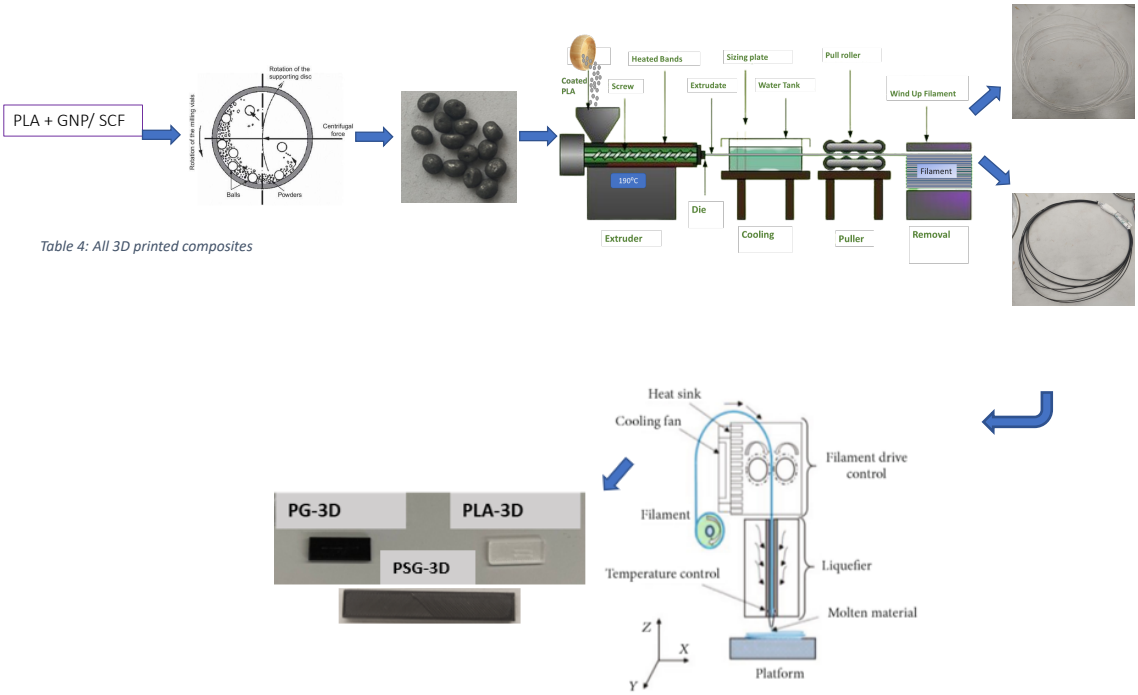

Figure 63: Complete diagram of 3D printed samples' manufacturing process.

6.2. Mechanical alloying / plastography, filament extrusion, and 3D Printing

The reference names and compositions of the 3D printed samples are shown in Table 14.

Table 14: Reference name and their composition of the 3D printed samples.

Samples	Short Name
PLA	PLA-3D
PLA-GNP	PG-3D
PLA-SCF-GNP	PSG-3D

6.2.1. Mechanical alloying

The mechanical alloying process was the same as described in section 5.1.1. Only the difference was the raw material was used as mentioned in table 14.

6.2.2. Filament Extrusion

The filaments were produced from mechanically alloyed mixtures synthesised with the same experimental parameters as the ones referred to in section 5.1.3.

Morphological and thermal characterisation of the filaments

The raw PLA particles with and without GNP and SCF coatings were extruded and subsequently inspected using an optical microscope (Fig. 64). From the figure it is observed that the diameter of the produced filament presents some diameter variations between 1.83 and 1.94 mm. But in some places, the diameter was 1.75 mm as well. On average the diameter was about 1.8mm which is suitable for 3D printing.

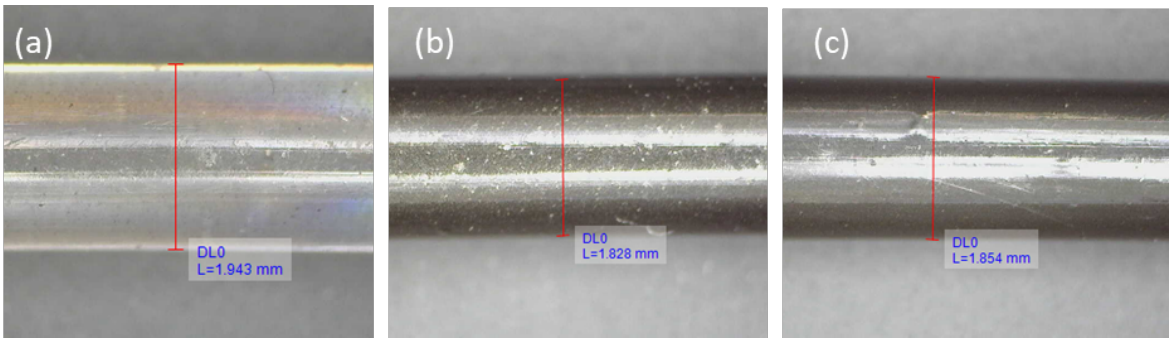

Figure 64: Diameter of (a) PLA, (b) PG and (c) PSG filaments.

The tomography results of the extruded filaments are illustrated in Fig. 65. The filaments are quite dense, with few pores. The GNP and SCF reinforcements are distributed all over the filaments which is noticeable by the yellow marks in the figure. This yellow marks actually indicates the agglomeration of the reinforced particles inside the filament. It should be noted

that, as expected, no elongated whiskers of SCF could be detected, because they were broken during the MA process.

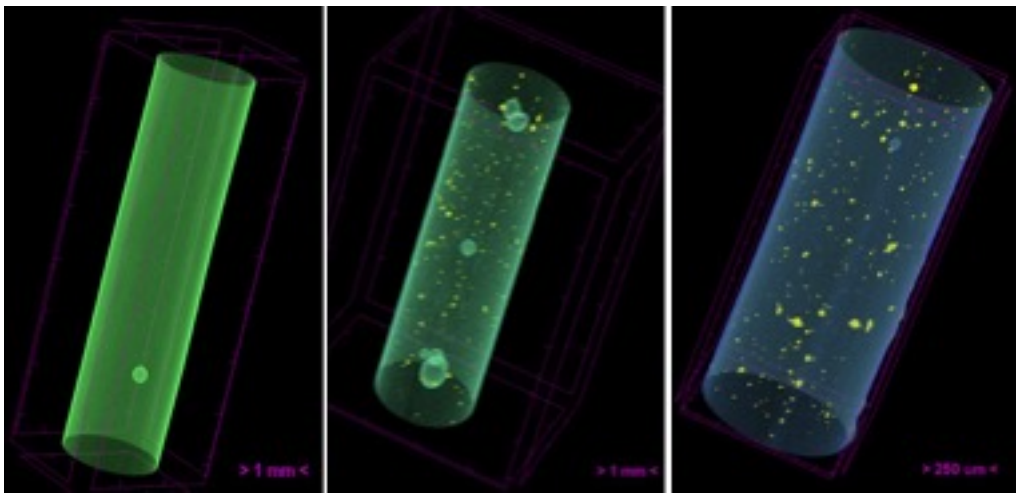

Figure 65: Microtomography images of (a) PLA, (b) PG, and (c) PSG filaments.

DSC analysis of the filaments is illustrated in Fig. 66. The curves are quite similar which means the reinforcements did not affect the thermal property of the PLA. A huge cold crystallization peak is visible at 100 ºC for all the samples. The extrusion process involves melting and rapid cooling of the polymer and therefore, the PLA didn't have enough time to crystallize. A similar phenomenon was also described by Sorrentino *et al.* in their work [93].

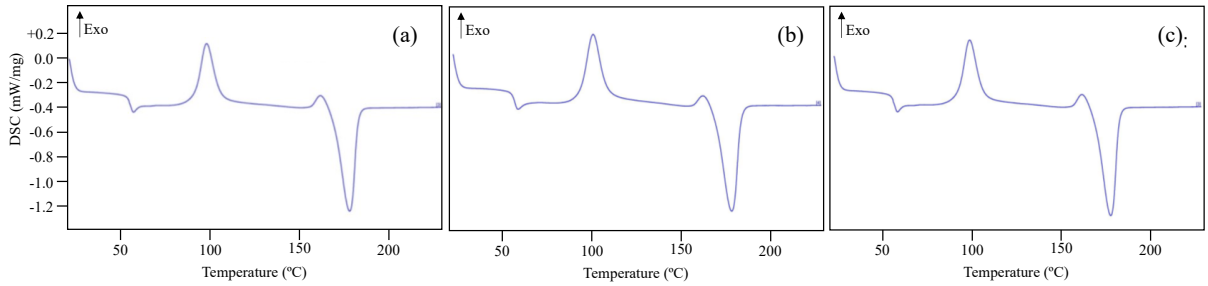

Figure 66: DSC curves of (a) PLA, (b) PG, and (c) PSG filaments.

6.2.3. 3D printing

Morphological and structural characterisation

The printed samples are shown in Fig. 67.

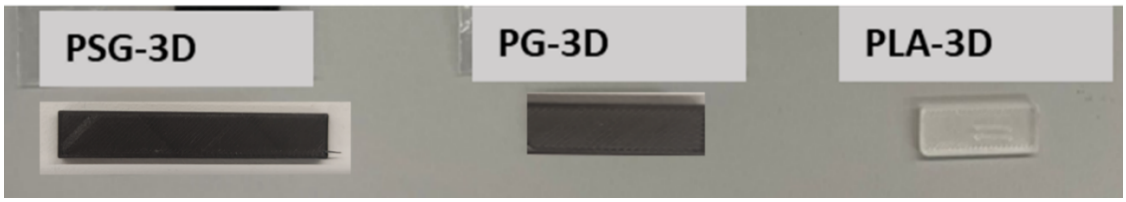

Figure 67: 3D printed samples.

The XRD patterns of the 3D printed samples are shown in Fig. 68. The PLA-3D sample is amorphous with a broad peak centred at 20º. PLA loses its crystalline structure during 3D printing due to the rapid cooling during processing. The XRD analysis of the PG-3D and PSG-3D samples was performed between 25° to 35° (position of the main diffraction peaks of GNP and SCF) and it confirmed the presence of both phases in the final printed samples. The peak for GNP is dominant whereas it is difficult to observe the XRD peak for SCF due to the amorphous structure of the PLA.

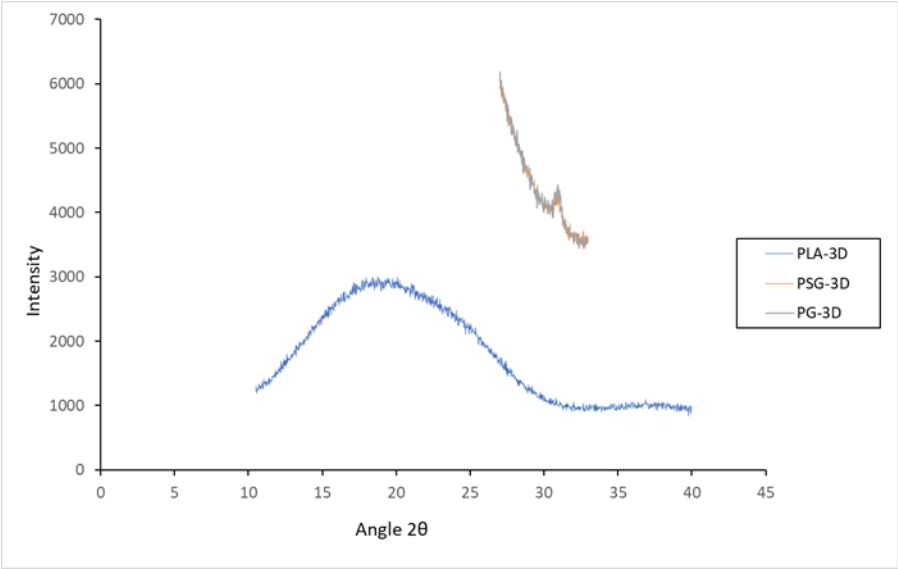

Figure 68: XRD patterns of the 3D printed samples.

The microtomography images of the 3D printed PG-3D and PSG-3D samples are illustrated in Figs. 69 and 70, respectively. The 0.1mm layer-by-layer construction is clearly noticeable in the images for the 3D printed samples. The 45° raster angle is also visible on the top surface of the samples. In both samples, the number of pores is higher at the centre of the samples than at their edges.

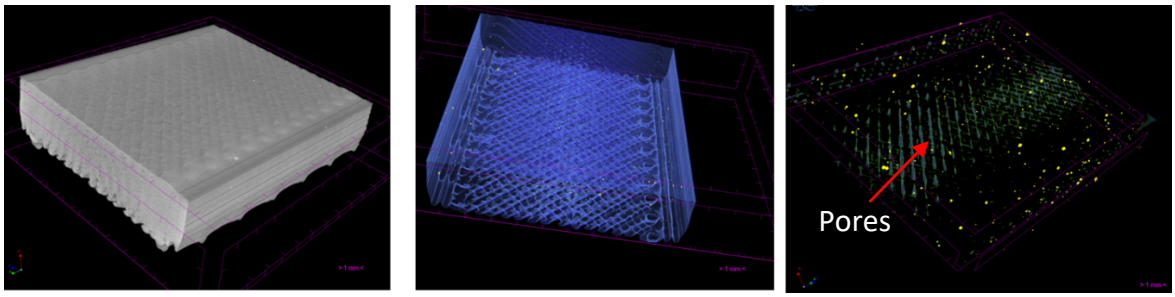

Figure 69: Microtomography of PG-3D.

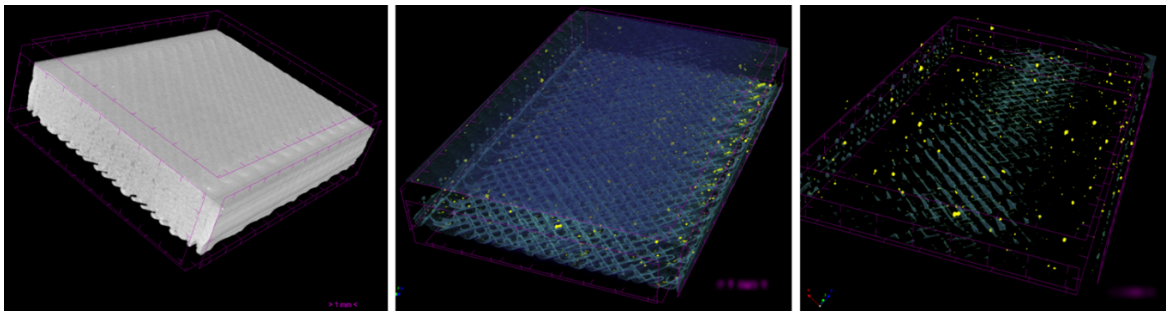

Figure 70: Microtomography of PSG-3D sample.

Mechanical and tribological characterisation

Figure 71 shows the Shore D values of the 3D printed samples. PLA-3D sample has a mean Shore D value of 61. Both, the PG-3D and PSG-3D have higher hardness values (73 and 78 Shore D, respectively.) The higher hardness value corresponds to a 22% increase when compared to the PLA-3D sample.

The shore D values of all the 3D printed samples are lower than the corresponding ones of the casted samples. The explanation for that is based on morphological and structural features: The 3D printed samples are mainly amorphous and present a higher level of porosity than the casted samples.

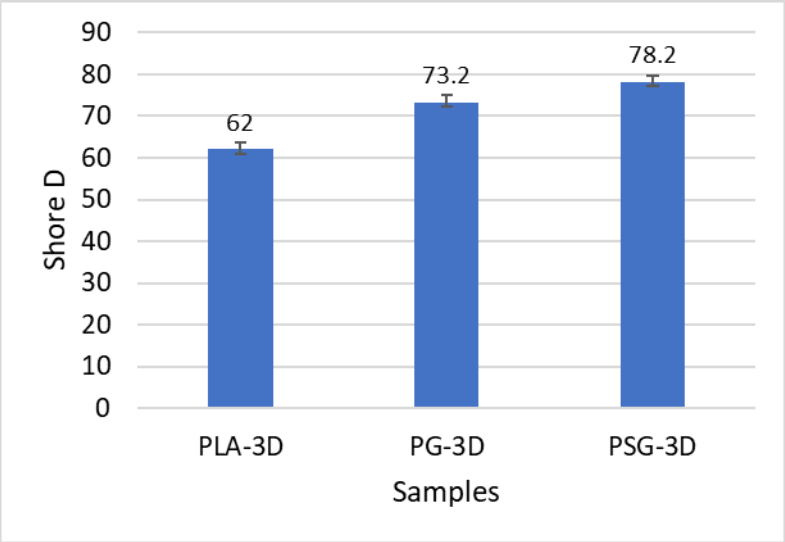

Figure 71: Shore D hardness of the 3D printed samples.

In Fig. 72, the load vs displacement and the flexural stress-strain curves obtained from the 3-point bending tests of the 3D printed samples are presented. For the same amount of displacement, a higher force is needed for the PG-3D and PSG-3D samples than for the PLA-3D ones (Fig. 72a). This means that the PG-3D and PSG-3D samples have higher flexural modulus than the PLA-3D sample. The flexural modulus of the PG-3D and PSG-3D samples (Fig. 73) is 7.2 and 8.1 GPa, respectively, which corresponds to values 2.2 and 2.6 times higher than the one of the PLA-3D sample (3.2 GPa). These results are in line with the previous studies by many authors for PLA-based composite with GNP or carbon fibre [68, 105-107]. SCF or GNP particles are attributed to the restriction of the polymeric chains which results in high resistance to strain and increases the load-bearing capacity.

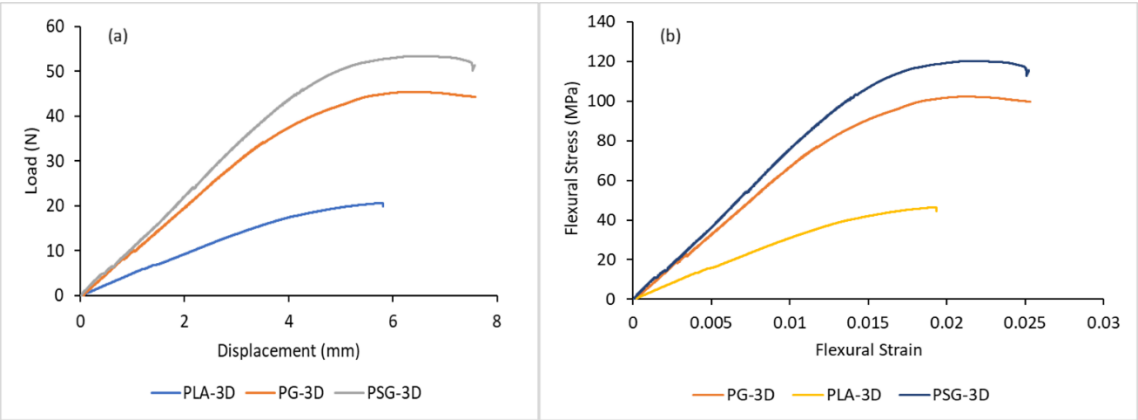

Figure 72: (a) Load vs displacement and (b) Flexural stress-strain curves of the 3D printed samples obtained from the 3-point bending tests.

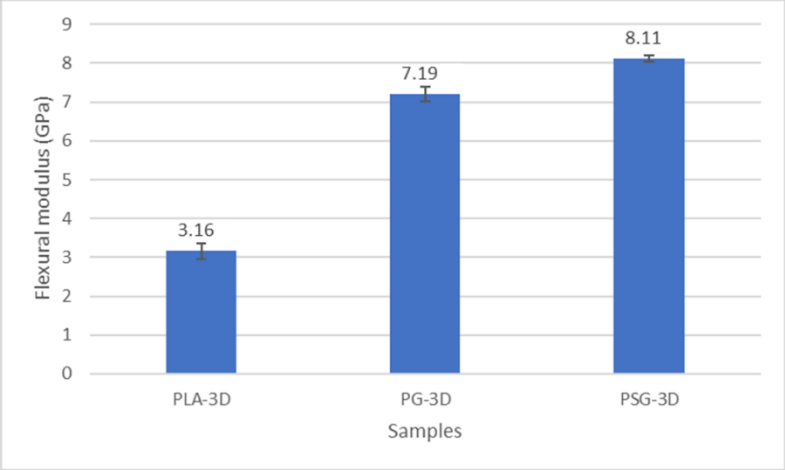

Figure 73: Flexural modulus of the 3D printed samples.

Figure 74 illustrates the COF vs time curves of the 3D printed samples. The average COF value of PLA-3D is around 0.60. PSG-3D sample has the lowest value of COF (~ 0.5) which corresponds to an 18% reduction when compared to the PLA-3D sample (Fig. 75). PG-3D shows a COF of ~ 0.53. The 3D printed samples have higher values of COF than the corresponding casted samples mainly because they were not polished to maintain the integrity of their surfaces and, therefore, they have higher roughness. The average roughness (Ra) of all the printed samples was almost the same (1.1-1.3 μm) whereas the Ra value of the polished casted samples was 500-600 nm. Higher roughness means less contact area and higher pressure was generated during the sliding test resulting in a boost in COF value for the printed sample compared to casted samples [108,109].

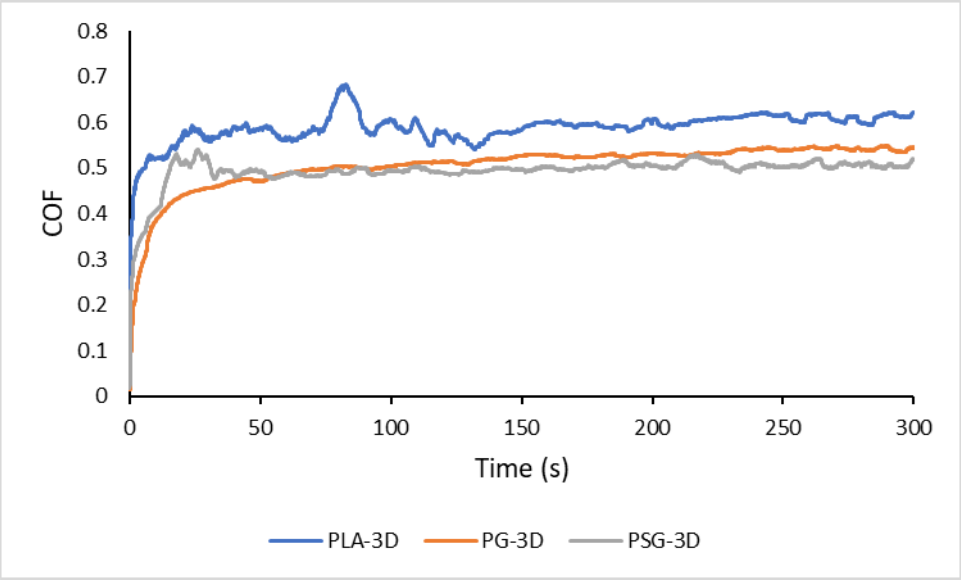

Figure 74: Time vs COF curves of the 3D printed samples.

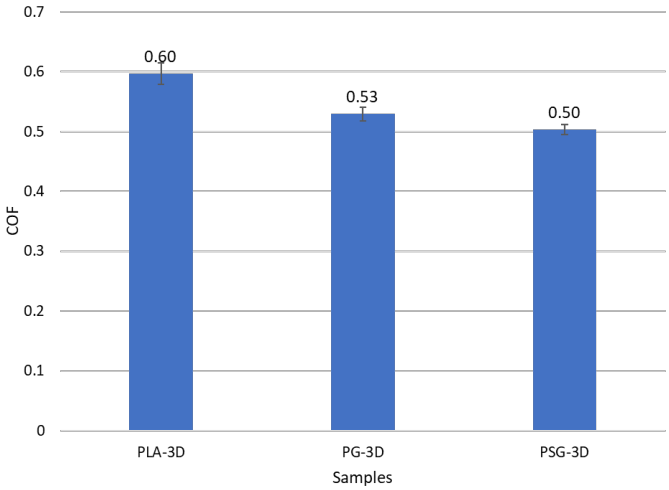

Figure 75: Average COF values of the 3D printed samples.

Figure 76 presents the 3D profilometry images of the wear scars and the corresponding wear profiles obtained from the 3D printed samples after the tribological tests. It is clearly observable that the wear profile of the PSG-3D sample has the lowest maximum wear depth (~ 15 µm) almost 4 times lower than the PLA-3D sample (~ 55 µm). The maximum wear depth of the PG-3D sample is in between these values (~ 23 µm).

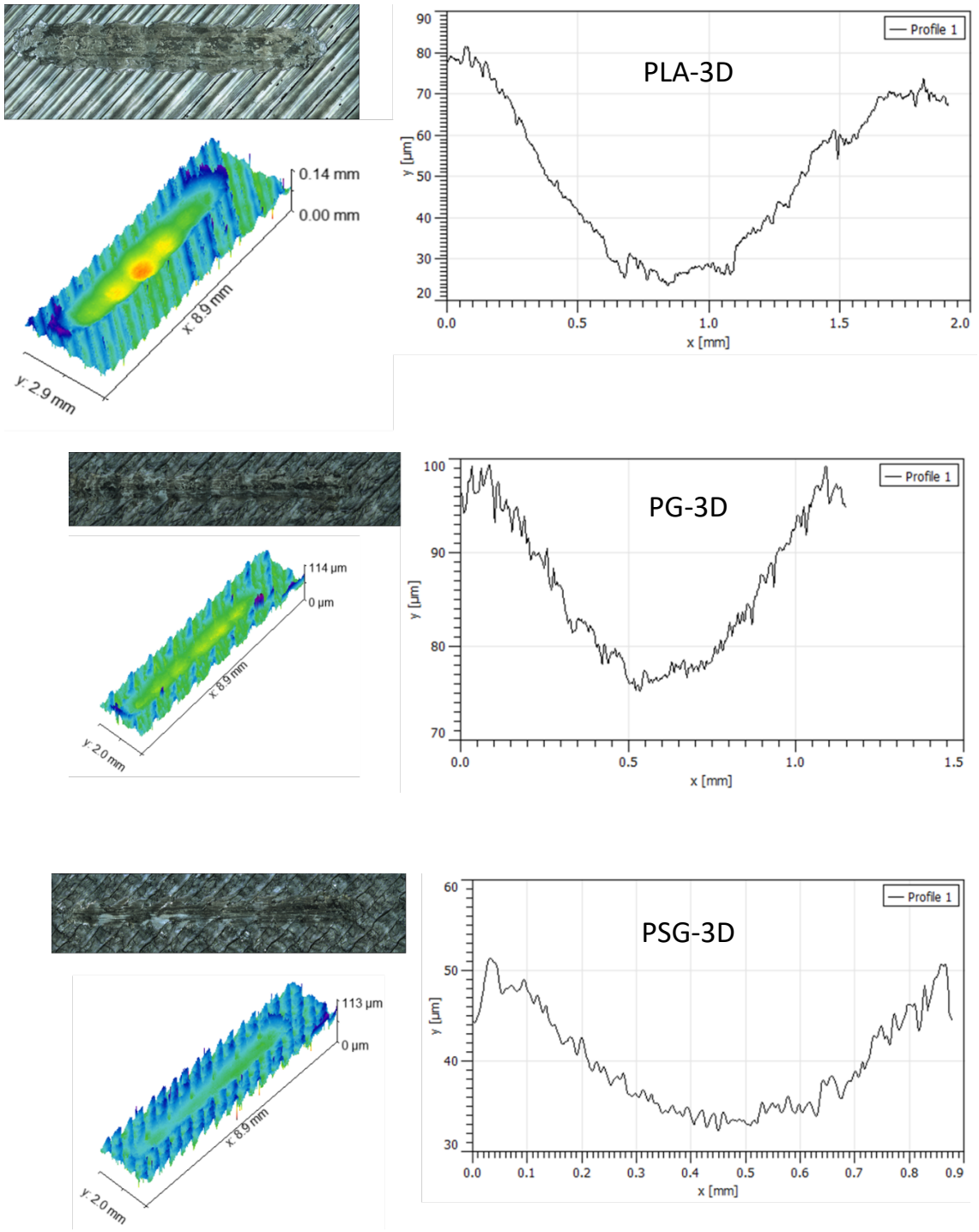

Figure 76: 3D profilometry images of the wear profiles and 3D scans of the 3D printed samples.

The wear rate of the 3D printed samples is illustrated in Fig.77. Pure PLA-3D has an average specific wear rate of 1.3e-3 mm^3/Nm. PSG-3D sample has the lowest wear rate (2.6e-04 mm^3/Nm) which is more than a 5 times reduction when compared to PLA-3D. The PG-3D sample has an intermediate wear rate of 4.5e-04 mm^3/Nm.

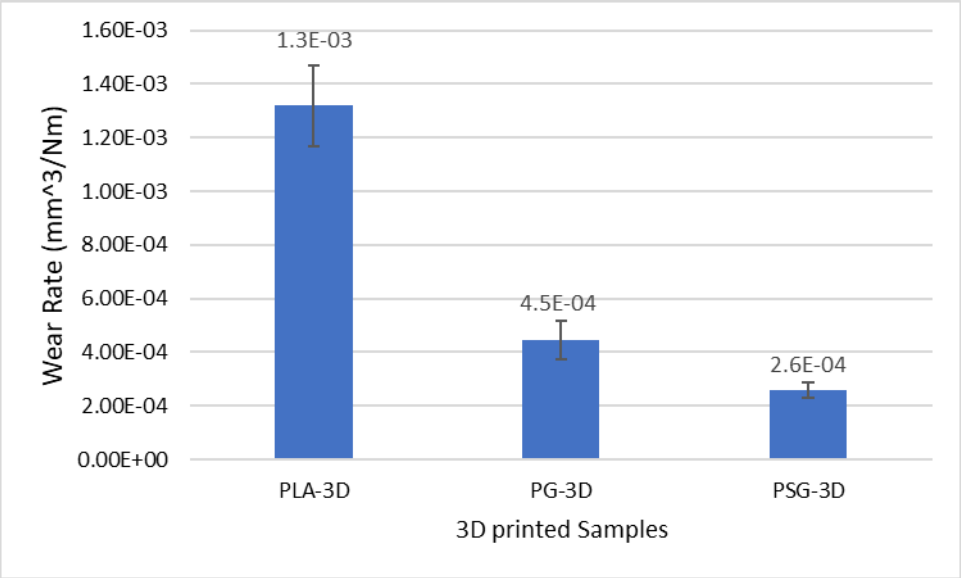

Figure 77: Specific Wear rate of the 3D printed samples.

These results of COF and wear rate of the composite sample agree with the works of many authors who showed the effect of SCF, and GNP incorporated polymer composites produced by 3D printing [98, 110].

Plastography, filament extrusion, and 3D Printing (Preliminary results)

A flow diagram of the 3D printing of the sample using plastography and granulation to control the reinforcements percentage in the composite is given in Fig. 78. Filaments of PLA with different amounts of GNP + SCF were produced by plastography (melting and mixing the PLA granules with GNP, SCF) followed by extrusion. Then, they were used to print the parts.

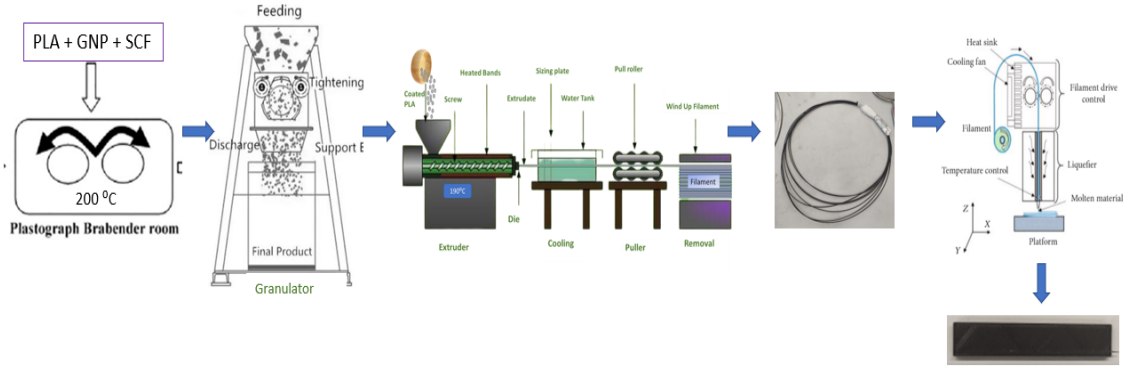

Figure 78: Complete diagram of 3D printed samples' manufacturing process using plastography.

6.3. Plastography, filament extrusion, and 3D Printing procedure

Table 15 presents the composition of PLA, GNP, and SCF for 3D printed composites using plastography and their reference name.

Table 15: Composition of PLA, GNP, and SCF for 3D printed composites using plastography and their reference name.

Sample name	PLA wt%	SCF wt%	GNP wt%
PSG-0.5	99	0.5	0.5
PSG-1	98	1	1
PSG-2	96	2	2
PSG-5	90	5	5

6.3.1 Plastography

During the mixing of SCF, GNP, and PLA in a plastograph, a Torque vs time curve was generated to observe the homogeneity of the mixture (Fig. 79). When the mixture becomes homogenous the curve becomes stable and horizontal to the time axis as the torque needed to mix the material is the same all over the mixture which is noticeable in Fig. 79. After the 600s the curve becomes stable. The more the amount of the material, the more torque is needed. That is why the torque value is going up with the increase in the percentage of the reinforcements.

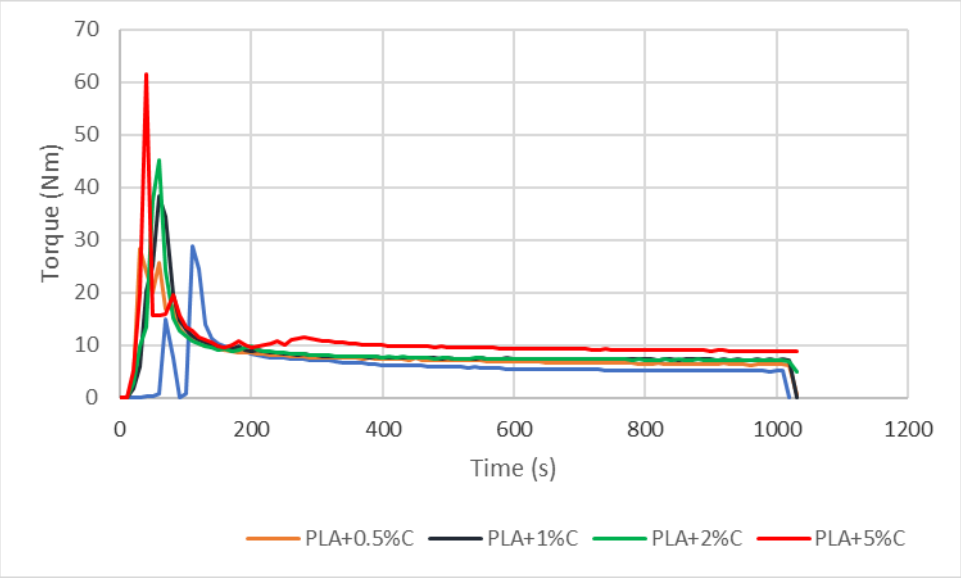

Figure 79: Torque vs time curve for different PLA, GNP, and SCF mixtures.

6.3.2. 3D printing

Figure 80 shows the PSG-2 which is a typical image of all the samples produced in this process. Here it is clearly noticeable that the surface is much wavier due to the higher layer thickness

and the bigger nozzle used to produce the samples compared to previously produced 3D printed samples (Fig. 67).

In this case, the parameter was changed because of some reasons. This time the raw powders were not broken by the milling process. So, the length of SCF inside the composite was 100-150 µm. Previously the diameter of the nozzle was 0.4mm so it was difficult to print the samples properly as the nozzle got clogged and no material was coming out of the nozzle. Another reason was that the diameter of the filament was more than 1.9mm in some places of the filament. As a result, a 0.8mm nozzle was used for the printing and the layer thickness was also changed to 0.2mm. Another noticeable thing is that during the mixing in the plastograph, there were some foreign elements inside the chamber even after cleaning it several times which may affect the composition of the composites as well as the results.

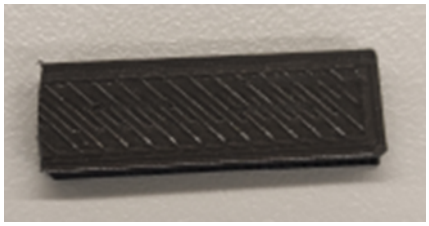

Figure 80: PSG-2 3D printed sample.

Mechanical and tribological characterisation

PSG-5 has the maximum Shore D hardness and PSG-0.5 has the lowest. PSG-1 and PSG-2 have almost the same hardness value though PSG-1 is slightly better (Fig. 81).

So, the specimen with a 5 wt.% GNP, SCF content had the greatest value. Clearly, the presence of graphene and SCF, which is significantly harder than the polymer matrix, increases hardness. Even a small amount of GNP+SCF—up to 1 wt. %, as demonstrated in other experiments [111-113] can boost the composite material's hardness value.

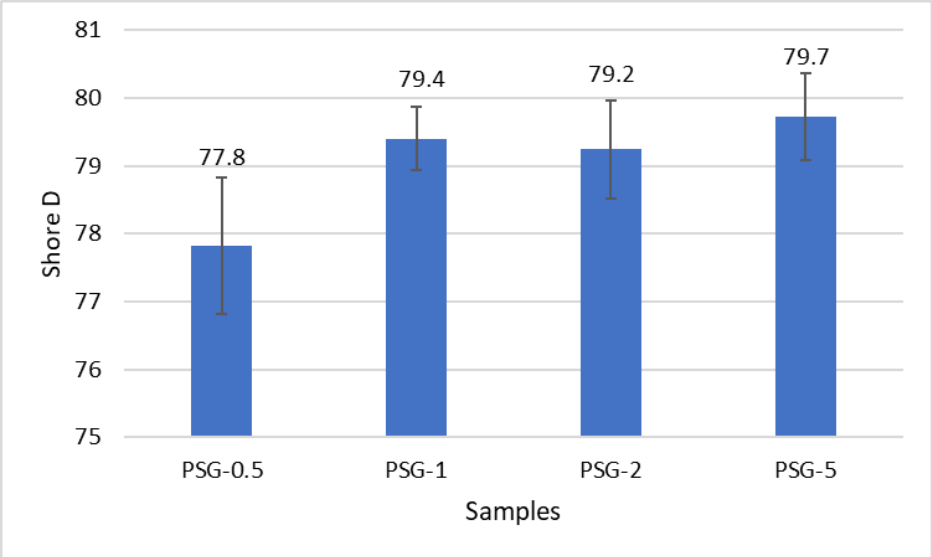

Figure 81: Shore D hardness of the 3D printed samples.

From Fig. 83, it is observed that PSG-0.5 has the lowest average COF value (0.49) among all the samples although the difference between the PSG-1 sample is not significant. PSG-1 has an average COF value of 0.5. But the PSG-2 has a comparatively higher COF value (0.54), and the PSG-5 possesses the highest of all which is 0.58. The findings demonstrated that the coefficient of friction was unaffected by GNP and SCF concentrations above 0.5 percent by weight. Therefore, the GNP+SCF percentage of 0.5 wt.% for the composite material employed in this study was deemed the ideal ratio for achieving the best results for friction behaviour which is somehow similar to the study of Hanon *et al.* [110] although in that study the polymer was different and only graphene was used as reinforcements.

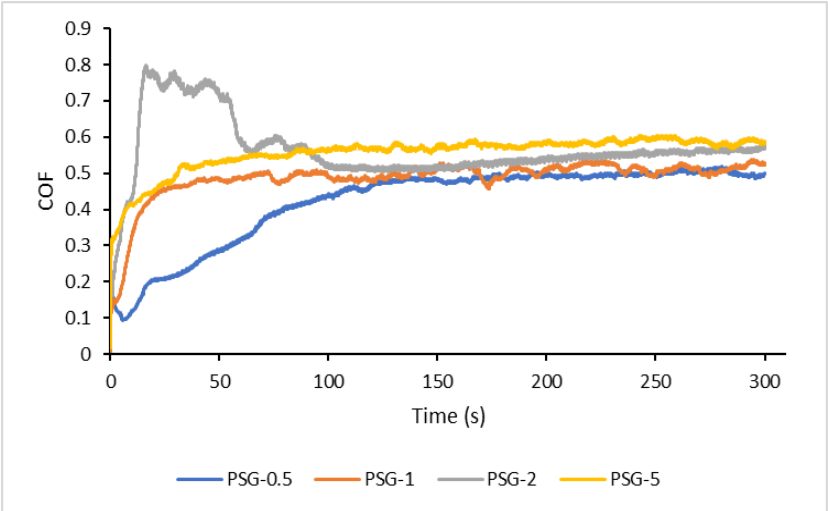

Figure 82: Time vs COF curves of the 3D printed samples.

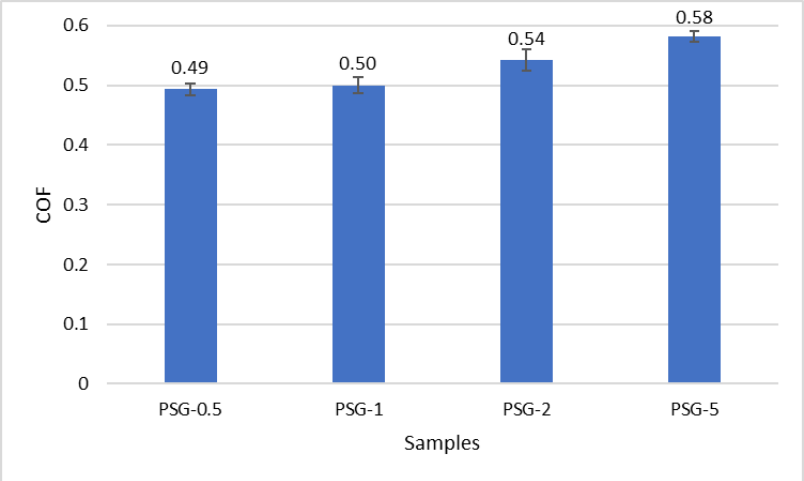

Figure 83: Average COF values of the casted samples.

Laser texturing, cold compaction, and laser sintering

A flow diagram of the laser texturing, reinforcement of the texture by cold compaction, and laser sintering for sample production are given in Fig. 84.

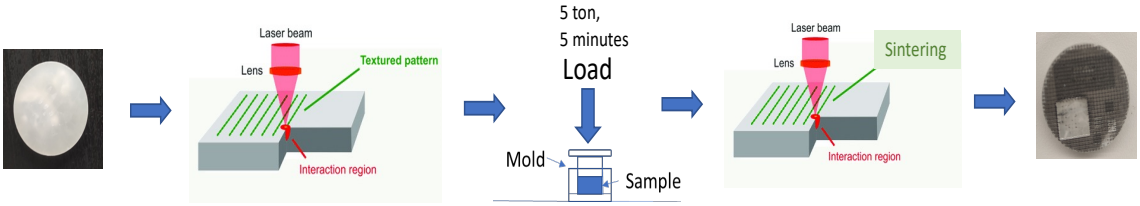

Figure 84: Laser Texturing and Sintering process for composite manufacturing.

This process consisted of three steps: laser texturing of casted PLA, reinforcement of the texture with GNP, SCF, and GNP+SCF by cold pressing, and laser sintering.

6.4. Laser texturing, reinforcement of the texture by cold compaction, and laser sintering

Three different samples were produced by this process (Table 16).

Table 16: Composition and reference name of Samples produced by laser texturing.

Sample name	Composition
PG-T	PLA reinforced with GNP
PS-T	PLA reinforced with SCF
PSG-T	PLA reinforced with SCF and GNP

6.4.1 Laser texturing

Morphological characterisation

Different laser parameters were used to optimize the texture to obtain a pattern capable to accommodate the different reinforcements. The best results were obtained with the following parameters: laser power 10 W, speed = 60 mm/s, frequency = 100 kHz, spot delay = 0.1 ms and step angle =90º. With these experimental conditions, quite a uniform pattern was produced (Fig. 85). Grooves have a depth of about 200 µm and a width of 400 µm.

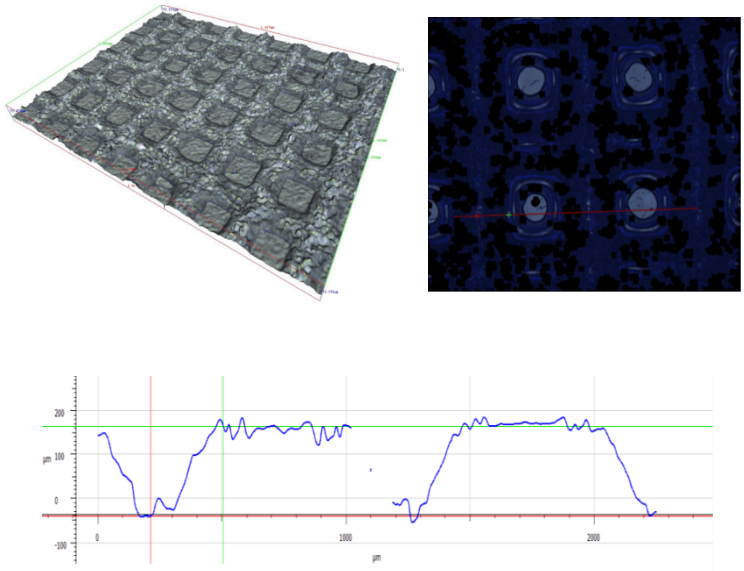

Figure 85: 3D profilometry images and 3D scan of the textured PLA.

6.4.2. Cold Compaction

Figure 86 shows the 3D profilometry images and 3D scans of the reinforced samples after cold compaction of the three reinforcements (GNP, SCF, and GNP+SCF). For PG-T the GNP particles almost covered the whole groove of the textures. On average only 25 µm of depth was left after the cold compaction with GNP. A similar phenomenon happened with the PSG-T

samples. SCF and GNP covered most of the grooves (30 µm of depth left). But for the PS-T samples, SCF did not cover the textured zone as the adhesion between SCF was not good after cold compaction. The SCF could not attach to each other by pressing whereas the GNP built layers and it is doubted that it might have transformed into Graphite on the textured surface.

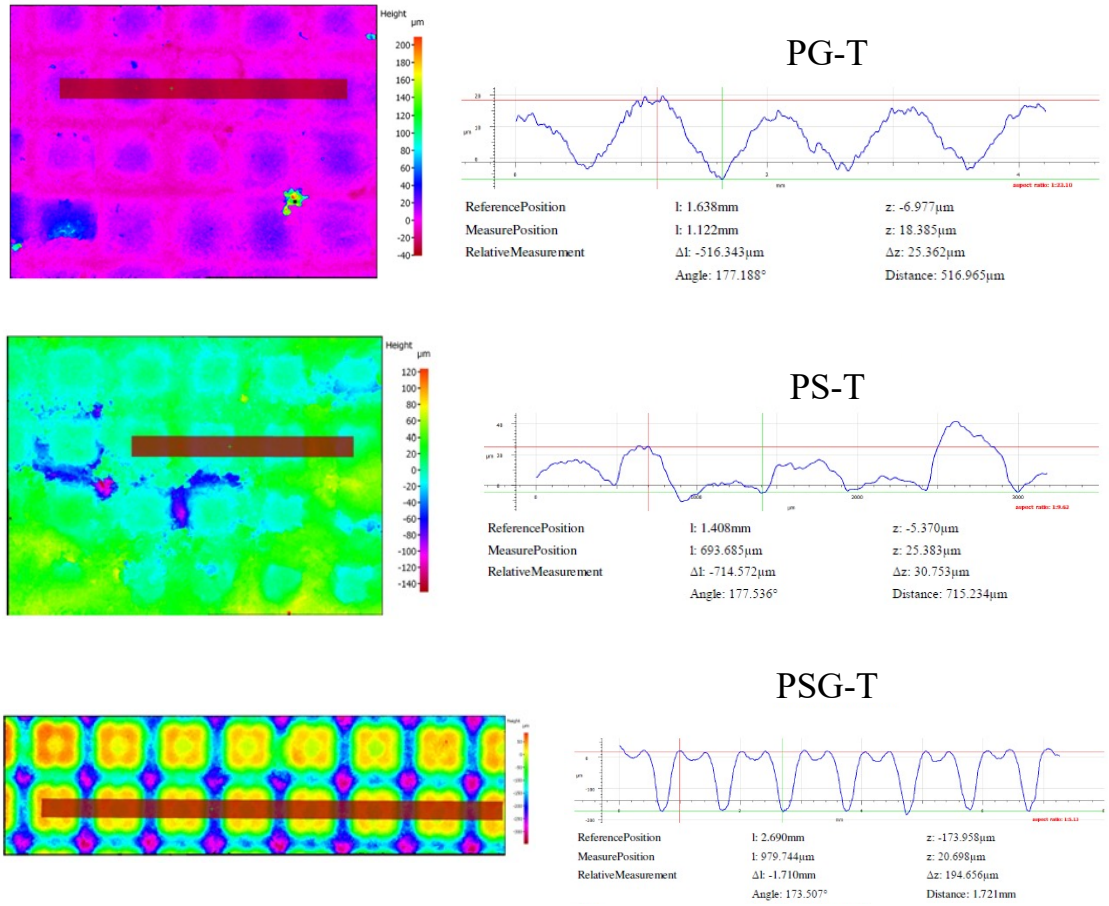

Figure 86: 3D profilometry images and 3D scan of the reinforced textured PLA.

Mechanical and tribological characterisation

Shore hardness values of the samples are shown in figure 87. PG-T has the lowest shore D value (63) whereas PS-T has the highest one (74).

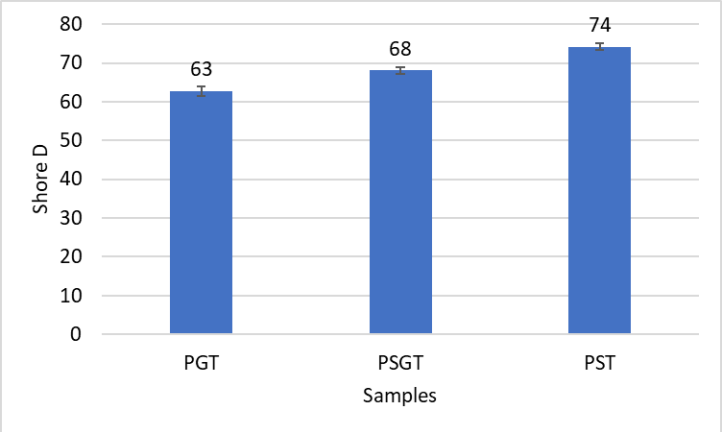

Figure 87: Shore D hardness of the 3D textured samples

PG-T shows the lowest COF value (0.33), and PST has the highest one (0.59) (Fig 89). But many more of these values are needed to be evaluated again as the composite samples after sintering was not in good condition. Much more iterations of sintering parameters need to be done to find out the optimum condition to produce good composite samples.

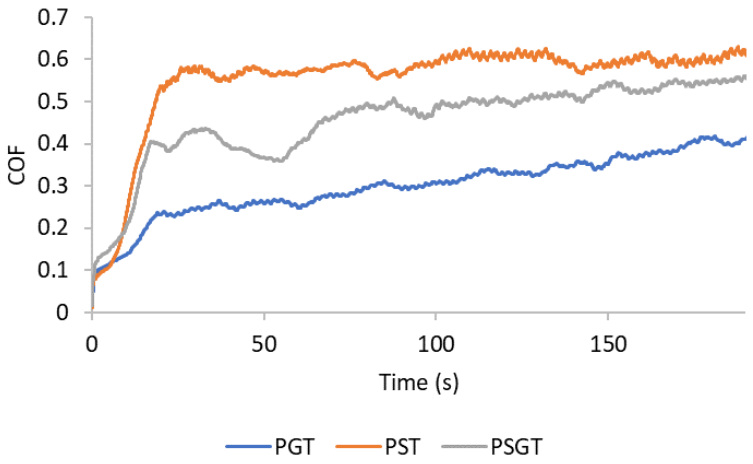

Figure 88: Time vs COF curves of the textured samples.

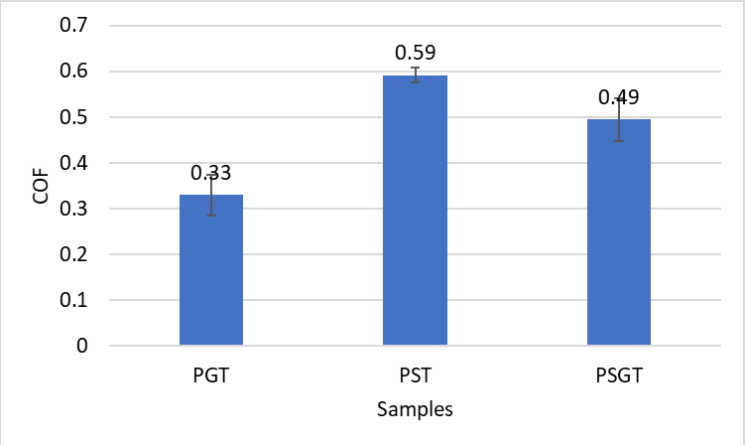

Figure 89: Average COF values of the textured samples.

7. CONCLUSION

Three different routes were followed to produce the composite samples - mechanical alloying followed by casting, mechanical alloying/plastograohy followed by 3D printing, and laser texturing followed by cold compaction and laser sintering. Based on the results obtained the following main conclusions may be withdrawn:

- Concerning the casted samples, all the composites produced presented higher hardness values than pure PLA (77 Shore D). The highest Shore D hardness was obtained for PSG (84.5, corresponding to a 10% increase in hardness compared to PLA). PG showed the lower COF (0,43) whilst the PSG sample presented the higher hardness and wear resistance (85 and $1.5e^{-4}$ mm^3/Nm, respectively). The PSG sample showed only an increase of 2.3 % in COF when compared to the PG sample. So, it can be concluded that PSG was the best performing sample produced by the casting process. PA samples (PLA reinforced with metallic alloy) produced by casting did not perform well compared to the other composite samples showing worse tribological and wear properties than pure PLA.

- The best mechanical and tribological properties of the 3D printed parts were obtained for the PSG-3D sample. The GNP and SCF reinforcements increased the flexural modulus, hardness, and wear resistance of the PLA matrix and reduced its friction coefficient. 3D printed samples had higher COF values than casted samples which were explained by their higher average roughness. The hardness values of the 3D printed samples were also lower than the corresponding ones of casted samples because of their amorphization and higher number of pores. The increase in the percentage of SCF and GNP in the composites hadn't a beneficial effect on the tribological properties, but there was a slight increase in hardness from PSG-0.5 to PSG-1.

- The samples produced by laser surface texturing and sintering presented some issues related to the lack of a proper sintering process However, as preliminary results, it can be stated that the PGT performed better tribologically and PST mechanically.

8. FUTURE WORK

There are few scopes for future work.

1. Concerning the casting process, to study the influence of different concentrations of GNP and SCF on the mechanical and tribological behaviour of the PLA composites.
2. Study of the laser sintering parameters on the final properties of the PLA composites.
3. Trying new polymer and reinforcements.

9. REFERENCES

[1]. Kumar, N., Arora, N.C. and Datta, B. (2014). Bearing surfaces in hip replacement – Evolution and likely future. Medical Journal Armed Forces India, [online] 70(4), pp.371–376. Available at: https://www.ncbi.nlm.nih.gov/pmc/articles/PMC4223187/.

[2]. Kaivosoja, E., Tiainen, V.-M., Takakubo, Y., Rajchel, B., Sobiecki, J., Konttinen, Y.T. and Takagi, M. (2013). Materials used for hip and knee implants. Wear of Orthopaedic Implants and Artificial Joints, pp.178–218.

[3]. King, S.W., Royeca, J.M., Cunningham, C.M., Madegowda, R., Sha, S., and Pandit, H. (2020). Metal hypersensitivity in total knee arthroplasty. Journal of Arthroscopy and Joint Surgery, 7(4), pp.184–188.

[4]. Liu, X., Holzwarth, J.M. and Ma, P.X. (2012). Functionalized Synthetic Biodegradable Polymer Scaffolds for Tissue Engineering. Macromolecular Bioscience, 12(7), pp.911–919.

[5]. Chatterjee, U., Jewrajka, S. K. and Guha, S. (2008). 'Dispersion of functionalized silver nanoparticles in polymer matrices: Stability, characterisation, and physical properties', Polymer Composites. Wiley, 30(6), pp. 827–834.

[6]. Son, W.K., Youk, J.H. and Park, W.H. (2006). Antimicrobial cellulose acetate nanofibres containing silver nanoparticles. Carbohydrate Polymers, 65(4), pp.430–434.

[7]. Zare, Y. (2015). A simple technique for determination of interphase properties in polymer nanocomposites reinforced with spherical nanoparticles. Polymer, 72, pp.93–97.

[8]. Zare, Y. and Garmabi, H. (2015). Thickness, modulus, and strength of interphase in clay/polymer nanocomposites. Applied Clay Science, 105-106, pp.66–70.

[9]. Zare, Y. and Garmabi, H. (2014). Modeling of interfacial bonding between two nanofillers (montmorillonite and CaCO3) and a polymer matrix (PP) in a ternary polymer nanocomposite. Applied Surface Science, 321, pp.219–225.

[10]. Zare, Y. and Garmabi, H. (2014). Attempts to Simulate the Modulus of Polymer/Carbon Nanotube Nanocomposites and Future Trends. Polymer Reviews, 54(3), pp.377–400.

[11]. Seyedjafari, E., Soleimani, M., Ghaemi, N., and Shabani, I. (2010). Nanohydroxyapatite-Coated Electrospun Poly(l-lactide) Nanofibres Enhance Osteogenic Differentiation of Stem Cells and Induce Ectopic Bone Formation. Biomacromolecules, 11(11), pp.3118–3125.

[12]. Shabani, I., Haddadi-Asl, V., Seyedjafari, E., and Soleimani, M. (2012). Cellular infiltration on nanofibrous scaffolds using a modified electrospinning technique. Biochemical and Biophysical Research Communications, 423(1), pp.50–54.

[13]. Deka, H., Karak, N., Kalita, R.D. and Buragohain, A.K. (2010). Bio-based thermostable, biodegradable, and biocompatible hyperbranched polyurethane/Ag nanocomposites with antimicrobial activity. Polymer Degradation and Stability, 95(9), pp.1509–1517.

[14]. DeStefano, V., Khan, S. and Tabada, A. (2020). Applications of PLA in modern medicine. Engineered Regeneration, 1, pp.76–87.

[15]. Faisal, Nadeem & Kumar, Kaushik. (2017). Polymer and metal nanocomposites in biomedical applications. 7(6), pp. 2286-2294.

[16]. Domènech, Berta & Muñoz, M. & Muraviev, Dmitri & Macanás, Jorge. (2013). Polymer-Silver Nanocomposites as Antibacterial materials.1,pp. 630-640

[17]. Papageorgiou, G.Z., Achilias, D.S., Nianias, N.P., Trikalitis, P. and Bikiaris, D.N. (2013). Effect of the type of nano-filler on the crystallization and mechanical properties of syndiotactic polystyrene-based nanocomposites. Thermochimica Acta, 565, pp.82–94.

[18]. Muraviev, D.N., Ruiz, P., Muñoz, M. and Macanás, J. (2008). Novel strategies for preparation and characterisation of functional polymer-metal nanocomposites for electrochemical applications. Pure and Applied Chemistry, 80(11), pp.2425–2437.

[19]. Afzal, A.B., Akhtar, M.J., Nadeem, M., Ahmad, M., Hassan, M.M., Yasin, T. and Mehmood, M. (2008). Structural and electrical properties of polyaniline/silver nanocomposites. Journal of Physics D: Applied Physics, 42(1), p.015411.

[20]. Asm International. (1987). Engineered materials handbook. Vol. 1, Vol. 1.

[21]. Park, S.-J., (2018). Carbon Fibres. Fibre Technol. Fibre-Reinforced Compos., 210, pp.123-151.

[22]. Nesher, G., Marom, G. and Avnir, D. (2008). Metal−Polymer Composites: Synthesis and Characterisation of Polyaniline and Other Polymer@Silver Compositions. Chemistry of Materials, 20(13), pp.4425–4432.

[23]. Sandhanshiv, R.D. and Patel, D.M. (2020). Carbon Fibre Reinforced Composite Material: Review of Properties and Processing for various Metal Matrix Materials. IOP Conference Series: Materials Science and Engineering, 810(1), p.012014.

[24]. Walsh, P.J. (2001). Carbon Fibres. Composites, pp.35–40.

[25]. Christensen, R.M. (1994). Properties of carbon fibres. Journal of the Mechanics and Physics of Solids, 42(4), pp.681–695.

[26]. MInus, M. and Kumar, S. (2005). The processing, properties, and structure of carbon fibres. JOM, [online] 57(2), pp.52–58. Available at: https://link.springer.com/article/10.1007%2Fs11837-005-0217-8.

[27]. Chand, S. (2000). Journal of Materials Science, 35(6), pp.1303–1313.

[28]. Baker, A.A. (1975). Carbon fibre reinforced metals — a review of the current technology. Materials Science and Engineering, 17(2), pp.177–208.

[29]. Dorey, G. (1987). Carbon fibres and their applications. Journal of Physics D: Applied Physics, 20(3), pp.245–256.

[30]. Huang, X. (2009). Fabrication and Properties of Carbon Fibres. Materials, [online] 2(4), pp.2369–2403. Available at: https://www.ncbi.nlm.nih.gov/pmc/articles/PMC5513585/

[31]. S, P., KM, S., K, N. and S, S. (2017). Fibre Reinforced Composites - A Review. Journal of Material Science & Engineering, 06(03).

[32]. Christensen, R.M. (1994). Properties of carbon fibres. Journal of the Mechanics and Physics of Solids, 42(4), pp.681–695.

[33]. Ozkan, D., Gok, M.S. and Karaoglanli, A.C. (2020). Carbon Fibre Reinforced Polymer (CFRP) Composite Materials, Their Characteristic Properties, Industrial Application Areas and Their Machinability. Advanced Structured Materials, pp.235–253.

[34]. Sreenivasulu, B., Ramji, BR. and Nagaral, M. (2018). A Review on Graphene Reinforced Polymer Matrix Composites. Materials Today: Proceedings, [online] 5(1, Part 3), pp.2419–2428. Available at: https://www.sciencedirect.com/science/article/pii/S2214785317322538

[35]. Sreenivasulu, B., Ramji, BR. and Nagaral, M. (2018). A Review on Graphene Reinforced Polymer Matrix Composites. Materials Today: Proceedings, [online] 5(1, Part 3), pp.2419–2428. Available at: https://www.sciencedirect.com/science/article/pii/S2214785317322538

[36]. Kandemir, N.; Yemeniciogwlu, A.; Mecitogwlu, C.; Elmaci, Z.S.; Arslanogwlu, A.; Göksungur, Y.; Baysal, T. (2005). Production of antimicrobial films by incorporation of partially purified lysozyme into biodegradable films of crude exopolysaccharides obtained from Aureobasidium pullulans fermentation. Food Technol. Biotechnol. 43(4), pp. 343—350.

[37]. Daloia, D. (2014). Friction And Wear Behaviour of Graphene Reinforced Epoxy. [Master's thesis, University of Dayton] [online] Available at: https://etd.ohiolink.edu/apexprod/rws_etd/send_file/send?accession=dayton1403532384&disposition=inline

[38]. Ilyas, R.A., Sapuan, S.M., Harussani, M.M., Hakimi, M.Y.A.Y., Haziq, M.Z.M., Atikah, M.S.N., Asyraf, M.R.M., Ishak, M.R., Razman, M.R., Nurazzi, N.M., Norrrahim, M.N.F., Abral, H. and Asrofi, M. (2021). Polylactic Acid (PLA) Biocomposite: Processing, Additive Manufacturing, and Advanced Applications. Polymers, 13(8), pp.1326.

[39]. Lunt, J. (1998). Large-scale production, properties, and commercial applications of polylactic acid polymers. Polymer Degradation and Stability, 59(1-3), pp.145–152.

[40]. Södergård, A. and Stolt, M. (2002). Properties of lactic acid-based polymers and their correlation with composition. *Progress in Polymer Science*, 27(6), pp.1123–1163.

[41]. Middleton, J.C., and Tipton, A.J. (2000). Synthetic biodegradable polymers as orthopedic devices. Biomaterials, 21(23), pp.2335–2346.

[42]. Fiore, G.L., Jing, F., Young, Jr., V.G., Cramer, C.J. and Hillmyer, M.A. (2010). High Tg aliphatic polyesters by the polymerization of spirolactide derivatives. Polymer Chemistry, 1(6), p.870.

[43]. www.ceresana.com. (n.d.). Bioplastics Report: Industry Analysis, Market, Growth | Ceresana. [online] Available at: https://www.ceresana.com/en/marketstudies/plastics/bioplastics/market-study-bioplastics.html

[44]. Lam, C.X.F., Olkowski, R., Swieszkowski, W., Tan, K.C., Gibson, I. and Hutmacher, D.W. (2008). Mechanical and in vitro evaluations of composite PLDLLA/TCP scaffolds for bone engineering. Virtual and Physical Prototyping, 3(4), pp.193–197.

[45]. Bose, S., Vahabzadeh, S. and Bandyopadhyay, A. (2013). Bone tissue engineering using 3D printing. Materials Today, 16(12), pp.496–504.

[46]. Bayraktar, E., (2015). Chapter 04108 - Section 12 Composites Materials and Technologies. Ref. Modul. Mater. Sci. Mater. Eng., 1-3.

[47]. Hsissou, R., Seghiri, R., Benzekri, Z., Hilali, M., Rafik, M. and Elharfi, A. (2021). Polymer composite materials: A comprehensive review. Composite Structures, [online] 262, p.113640.

[48]. Kiser, J.D., David, K.E., Davies, C., Andrulonis, R. and Ashforth, C. (2017). Updating Composite Materials Handbook-17 Volume 5-Ceramic Matrix Composites. Ceramic Transactions Series, pp.413–423.

[49]. Spasova, D., Argiro, Y. and Mechkarova, T. (2021). Comparative Analysis of the Mechanical Properties of Polymer Matrix Composites Reinforced with Fibreglass Fabric. TEM Journal, pp.1745–1750.

[50]. L Pilato and Michno, M.J. (1994). Advanced composite materials. Berlin: New York.

[51]. Jin, F.-L., Li, X. and Park, S.-J. (2015). Synthesis and application of epoxy resins: A review. Journal of Industrial and Engineering Chemistry, 29, pp.1–11.

[52]. Scribd. (n.d.). Advanced Composite Materials | PDF | Composite Material | Manmade Materials. [online] Available at: https://www.scribd.com/document/158109749/Advanced-Composite-Materials.

[53]. Spitalsky, Z., Tasis, D., Papagelis, K. and Galiotis, C. (2010). Carbon nanotube–polymer composites: Chemistry, processing, mechanical and electrical properties. Progress in Polymer Science, 35(3), pp.357–401.

[54]. Sreenivasulu, B., Ramji, BR. and Nagaral, M. (2018). A Review on Graphene Reinforced Polymer Matrix Composites. Materials Today: Proceedings, [online] 5(1, Part 3), pp.2419–2428. Available at: https://www.sciencedirect.com/science/article/pii/S2214785317322538.

[55]. S.K. Mazumdar, (2002). Composites Manufacturing: Materials, Product, and Process Engineering, CRC Press.

[56]. Jem, K.J. and Tan, B. (2020). The development and challenges of poly (lactic acid) and poly (glycolic acid). Advanced Industrial and Engineering Polymer Research.

[57]. Hinchcliffe, S.A., Hess, K.M. and Srubar, W.V. (2016). Experimental and theoretical investigation of prestressed natural fibre-reinforced polylactic acid (PLA) composite materials. Composites Part B: Engineering, 95, pp.346–354.

[58]. Dwijaya, M.S., Rokhmanto, F., Lestari, F.P., Utomo, M.S., Asmaria, T., Hakim, R.N. and Kartika, I. (2021). A bioresorbable MgZn binary alloy strengthened poly-lactic acid matrix composite. The 5th Biomedical Engineering's Recent Progress In Biomaterials, Drugs Development, And Medical Devices: Proceedings of the 5th International Symposium of Biomedical Engineering (ISBE) 2020.

[59]. Batakliev, T. (2020). Tribological Investigation of Pla-Based Nanocomposites by Scratch and Wear Experiments. Journal of Theoretical and Applied Mechanics, 50(2). pp. 105-113.

[60]. Maqsood, N. and Rimašauskas, M. (2021). Characterisation of carbon fibre reinforced PLA composites manufactured by fused deposition modeling. Composites Part C: Open Access, 4, p.100112.

[61]. Valapa, R.B., Pugazhenthi, G. and Katiyar, V. (2015). Effect of graphene content on the properties of poly (lactic acid) nanocomposites. RSC Advances, 5(36), pp.28410–28423.

[62]. Ivanov, E., Kotsilkova, R., Xia, H., Chen, Y., Donato, R., Donato, K., Godoy, A., Di Maio, R., Silvestre, C., Cimmino, S. and Angelov, V. (2019). PLA/Graphene/MWCNT Composites with Improved Electrical and Thermal Properties Suitable for FDM 3D Printing Applications. Applied Sciences, 9(6), p.1209.

[63]. M Sherif El-Eskandarany (2001). Mechanical alloying for fabrication of advanced engineering materials. Norwich, N.Y.: Noyes Publications: William Andrew Pub.

[64]. Pan, J. and Shaw, W.J.D. (1995). Effects of processing parameters on material properties of mechanically processed polyamide. Journal of Applied Polymer Science, 56(5), pp.557–566.

[65]. Kaloshkin, S.D., Vandi, L.-J., Tcherdyntsev, V.V., Shelekhov, E.V. and Danilov, V.D. (2009). Multi-scaled polymer-based composite materials synthesised by mechanical alloying. Journal of Alloys and Compounds, 483(1-2), pp.195–199.

[66]. Monich, P.R., Henriques, B., Novaes de Oliveira, A.P., Souza, J.C.M. and Fredel, M.C. (2016). Mechanical and biological behaviour of biomedical PEEK matrix composites: A focused review. Materials Letters, 185, pp.593–597.

[67]. Ambrosio-Martín, J., Lopez-Rubio, A., Fabra, M.J., Gorrasi, G., Pantani, R. and Lagaron, J.M. (2014). Assessment of ball milling methodology to develop polylactide-bacterial cellulose nanocrystals nanocomposites. Journal of Applied Polymer Science, 132(10), p.n/a-n/a.

[68]. Caminero, M.Á., Chacón, J.M., García-Plaza, E., Núñez, P.J., Reverte, J.M. and Becar, J.P. (2019). Additive Manufacturing of PLA-Based Composites Using Fused Filament Fabrication: Effect of Graphene Nanoplatelet Reinforcement on Mechanical Properties, Dimensional Accuracy, and Texture. Polymers, 11(5), p.799. doi:10.3390/polym11050799.

[69]. Çevik, Ü., and Kam, M. (2020). A Review Study on Mechanical Properties of Obtained Products by FDM Method and Metal/Polymer Composite Filament Production. Journal of Nanomaterials, 2020, pp.1–9. doi:10.1155/2020/6187149.

[70]. Tomanik, M., Kobielarz, M., Filipiak, J., Szymonowicz, M., Rusak, A., Mroczkowska, K., Antończak, A. and Pezowicz, C. (2020). Laser Texturing as a Way of Influencing the Micromechanical and Biological Properties of the Poly(L-Lactide) Surface. Materials, 13(17), p.3786.

[71]. Ma, H., Suonan, A., Zhou, J., Yuan, Q., Liu, L., Zhao, X., Lou, X., Yang, C., Li, D., and Zhang, Y. (2021). PEEK (Polyether-ether-ketone) and its composite materials in orthopedic implantation. Arabian Journal of Chemistry, [online] 14(3), p.102977. Available at: https://www.sciencedirect.com/science/article/pii/S1878535220305384#:~:text=Polyether%2Dether%2Dketone%20(PEEK)%20is%20a%20new%20type

[72]. Singhvi, M.S., Zinjarde, S.S. and Gokhale, D.V. (2019). Polylactic acid: synthesis and biomedical applications. Journal of Applied Microbiology, 127(6), pp.1612–1626.

[73]. Benjamin, J.S. (1990). Mechanical alloying — A perspective. Metal Powder Report, 45(2), pp.122–127.

[74]. O. D. Neikov, “Chapter 3 - Mechanical Alloying,” ed: Elsevier Science & Technology, pp. 63-79.

[75]. Baheti, V., Abbasi, R. and Militky, J. (2012). Ball milling of jute fibre wastes to prepare nanocellulose. World Journal of Engineering, 9(1), pp.45–50.

[76]. Gilman, P.S. and Benjamin, J.S. (1983). Mechanical Alloying. Annual Review of Materials Science, 13(1), pp.279–300.

[77]. Bécot, François-Xavier & Jaouen, Luc & Chevillotte, Fabien & Khan, Amir & Horoshenkov, Kirill. (2011). Relating manufacturing parameters and material microstructure to acoustic properties of recycled polymers. Proceedings of Forum Acusticum.

[78]. Papon, E.A. and Haque, A. (2018). Tensile properties, void contents, dispersion and fracture behaviour of 3D printed carbon nanofibre reinforced composites. Journal of Reinforced Plastics and Composites, [online] 37(6), pp.381–395.

[79]. Stokes, D. and Microscopical, R. (2008). Principles and practice of variable pressure/environmental scanning electron microscopy (VP-ESEM). Chichester, U.K.: Wiley.

[80]. Scanning Electron Microscopy and X-ray Microanalysis. (2002). Erscheinungsort Nicht Ermittelbar: Kluwer Academic/Plenum Publishers.

[81]. Carmignato, S., Wim Dewulf and Leach, R. (2018). Industrial X-ray Computed Tomography. Cham Springer.

[82]. Nanoscience Instruments. (2018). Optical Profilometry - Nanoscience Instruments. [online] Available at: https://www.nanoscience.com/techniques/optical-profilometry/ [Accessed 6 Dec. 2019].

[83]. Bucksbaum, P.H., Ware, M.R., Natan, A., Cryan, J.P. and Glownia, J.M. (2020). Characterizing Multiphoton Excitation Using Time-Resolved X-ray Scattering. Physical Review X, 10(1).

[84]. Prenner, E. and Chiu, M. (2011). Differential scanning calorimetry: An invaluable tool for a detailed thermodynamic characterisation of macromolecules and their interactions. Journal of Pharmacy and Bioallied Sciences, 3(1), p.39.

[85]. Additive manufacturing hybrid processes for composites systems. (2020).

[86]. applerubber. (2021, June 29). Shore A Versus Shore D: The Important Differences You Need to Know. Official Apple Rubber Blog. https://www.applerubber.com/blog/shore-a-versus-shore-d-the-important-differences-you-need-to know/#:~:text=The%20major%20differentiation%20between%20the

[87]. Krishna Hansdah (2012). 3-point bend test. [online] Available at: https://pt.slideshare.net/kkh007/3-point-bend-test.

[88]. Kucharski, S. and Mróz, Z. (2011). Identification of wear process parameters in reciprocating ball-on-disc tests. Tribology International, 44(2), pp.154–164.

[89] Hara, S., Watanabe, S., Takahashi, K., Shimizu, S. and Ikake, H. (2018). Preparation of Crystallites for Oriented Poly (Lactic Acid) Films Using a Casting Method under a Magnetic Field. Polymers, 10(10), p.1083. doi:10.3390/polym10101083.

[90]. Gilman, P.S. and Benjamin, J.S. (1983). Mechanical Alloying. Annual Review of Materials Science, 13(1), pp.279–300.

[91]. Zhang, H., Tang, W.-M., Xu, G.-Q., Wu, Y.-C. and Zheng, Z.-X. (2010). Synthesis of Sn–Ag binary alloy powders by mechanical alloying. Materials Chemistry and Physics, 122(1), pp.64–68.

[92]. Huang, M.L., Wu, C.M.L., Lai, J.K.L., Wang, L. and Wang, F.G. (2000). Lead free solder alloys Sn-Zn and Sn-Sb prepared by mechanical alloying. Journal of Materials Science: Materials in Electronics, 11(1), pp.57–65.

[93]. Sorrentino, A., De Santis, F., & Titomanlio, G. (n.d.). Polymer Crystallization Under High Cooling Rate and Pressure: A Step Towards Polymer Processing Conditions. Progress in Understanding of Polymer Crystallization, 329–344.

[94]. Eayal Awwad, K.Y., Yousif, B.F., Fallahnezhad, K., Saleh, K. and Zeng, X. (2021). Influence of graphene nanoplatelets on mechanical properties and adhesive wear performance of epoxy-based composites. Friction, 9(4), pp.856–875.

[95]. García, P.G., Ramírez-Aguilar, R., Torres, M., Franco-Urquiza, E.A., May-Crespo, J. and Camacho, N. (2018). Mechanical and thermal behaviour dependence on graphite and oxidized graphite content in polyester composites. Polymer, [online] 153, pp.9–16.

[96]. Puértolas, J.A., Castro, M., Morris, J.A., Ríos, R. and Ansón-Casaos, A. (2019). Tribological and mechanical properties of graphene nanoplatelet/PEEK composites. Carbon, [online] 141, pp.107–122.

[97]. Shalwan, A. and Yousif, B.F. (2014). Influence of date palm fibre and graphite filler on mechanical and wear characteristics of epoxy composites. Materials & Design, 59, pp.264–273.

[98]. He, Q., Wang, H., Fu, K. and Ye, L. (2020). 3D printed continuous CF/PA6 composites: Effect of microscopic voids on mechanical performance. Composites Science and Technology, 191, p.108077.

[99]. Karsli, N.G. and Aytac, A. (2013). Tensile and thermomechanical properties of short carbon fibre reinforced polyamide 6 composites. Composites Part B: Engineering, 51, pp.270–275.

[100]. Berman, D., Erdemir, A. and Sumant, A.V. (2014). Graphene: a new emerging lubricant. Materials Today, 17(1), pp.31–42.

[101]. BATAKLIEV, T. (2020). TRIBOLOGICAL INVESTIGATION OF PLA-BASED NANOCOMPOSITES BY SCRATCH AND WEAR EXPERIMENTS. Journal of Theoretical and Applied Mechanics, 50(2).

[102] Mittal, G., Dhand, V., Rhee, K.Y., Park, S.-J. and Lee, W.R. (2015). A review on carbon nanotubes and graphene as fillers in reinforced polymer nanocomposites. Journal of Industrial and Engineering Chemistry, 21, pp.11–25.

[103]. Bustillos, J., Montero, D., Nautiyal, P., Loganathan, A., Boesl, B., and Agarwal, A. (2017). Integration of graphene in poly(lactic) acid by 3D printing to develop creep and wear-resistant hierarchical nanocomposites. Polymer Composites, 39(11), pp.3877–3888.

[104]. Friedrich, K. (2018). Polymer composites for tribological applications. Advanced Industrial and Engineering Polymer Research, 1(1), pp.3–39.

[105]. Abderrafai, Y., Hadi Mahdavi, M., Sosa-Rey, F., Hérard, C., Otero Navas, I., Piccirelli, N., Lévesque, M. and Therriault, D. (2022). Additive manufacturing of short carbon fibre-reinforced polyamide composites by fused filament fabrication: Formulation, manufacturing, and characterisation. Materials & Design, 214, p.110358.

[106]. El Magri, A., El Mabrouk, K., Vaudreuil, S. and Ebn Touhami, M. (2019). Mechanical properties of CF-reinforced PLA parts manufactured by fused deposition modeling. Journal of Thermoplastic Composite Materials, [online] p.089270571984724.

[107]. Ozkan, C., Gamze Karsli, N., Aytac, A. and Deniz, V. (2014). Short carbon fibre reinforced polycarbonate composites: Effects of different sizing materials. Composites Part B: Engineering, 62, pp.230–235.

[108]. Nirmal, U., Hashim, J. and Megat Ahmad, M.M.H. (2015). A review on tribological performance of natural fibre polymeric composites. Tribology International, 83, pp.77–104.

[109]. Dawoud, M., Taha, I. and Ebeid, S.J. (2015). Effect of processing parameters and graphite content on the tribological behaviour of 3D printed acrylonitrile butadiene styrene. Materialwissenschaft und Werkstofftechnik, 46(12), pp.1185–1195.

[110]. Hanon, M.M., Ghaly, A., Zsidai, L. and Klébert, S. (2022). Tribological characteristics of digital light processing (DLP) 3D printed graphene/resin composite: Influence of graphene presence and process settings. Materials & Design, 218, p.110718.

[111]. Chen, Y., Qi, Y., Tai, Z., Yan, X., Zhu, F. and Xue, Q. (2012). Preparation, mechanical properties, and biocompatibility of graphene oxide/ultrahigh molecular weight polyethylene composites. European Polymer Journal, 48(6), pp.1026–1033.

[112]. Tabandeh-Khorshid, M., Ferguson, J.B., Schultz, B.F., Kim, C.-S., Cho, K. and Rohatgi, P.K. (2016). Strengthening mechanisms of graphene- and Al2O3-reinforced aluminum nanocomposites synthesised by room temperature milling. Materials & Design, 92, pp.79–87.

[113]. Pérez-Bustamante, R., Bolaños-Morales, D., Bonilla-Martínez, J., Estrada-Guel, I. and Martínez-Sánchez, R. (2014). Microstructural and hardness behaviour of graphene-nanoplatelets/aluminum composites synthesised by mechanical alloying. Journal of Alloys and Compounds, 615, pp. S578–S582.